Self Assembly in Soft Matter

Alexandros Chremos

Doctor of Philosophy
University of Edinburgh
2008

Declaration

I declare that this thesis was composed by myself and that the work contained therein is my own, except where explicitly stated otherwise in the text.

(*Alexandros Chremos*)

To my parents

Abstract

The term “soft matter” applies to a variety of physical systems, such as liquids, colloids, polymers, foams, gels, and granular materials. The most fascinating aspect of soft matter lies in the fact that they are not atomic or molecular in nature. They are instead macromolecular aggregates, whose spatial extent lies in the domain 1 nm to 1 μm.

Some of the most important examples of soft matter are polymers, which exhibit intriguing and useful physical properties. In this work, the adsorption and self assembly of linear and star polymers on smooth surfaces are studied using coarse-grained, bead-spring molecular models and Langevin dynamics computer simulations. The aim is to gain insight on atomic-force microscopy images of polymer films on mica surfaces, adsorbed from dilute solution following a good solvent-to-bad solvent quenching procedure. In the case of linear polymers, under certain experimental conditions, a bimodal cluster distribution is observed. It is demonstrated that this type of distribution can be reproduced in the simulations, and rationalized on the basis of the polymer structures prior to the quench. In addition to providing insight on experimental observations, the simulation results support a number of predicted scaling laws such as the decay of the monomer density as a function of distance from the surface, and the scaling of the film height with the strength of the polymer-surface interactions.

Star polymers represent a special class of polymers, in which one end of each linear chain is tethered to a small central core to form a single particle. The discovery of these molecules led to the synthesis of a wide range of new materials. Their structures are effectively considered as intermediate between those of colloids and linear polymers. We explore the behaviour of the star polymers (which are like “soft colloids”) in the proximity of a surface, using Langevin dynamics simulations. A number of different measurements such as the height, radius of gyration, and asphericity of adsorbed stars with different number of arms, are shown to provide valuable insights on experimental findings.

The simplest soft matter systems consist of spherical, rigid colloidal particles.

Examples of such particles are chemically synthesized polystyrene or silica particles. We investigated the neighbour distribution in a two-dimensional polydisperse hard-disk fluid, corresponding physically to a colloidal monolayer. The disk diameter distribution was defined by a power-law with the aim of realizing a scale-free near-neighbour network. Scale-free (power-law) behaviour is found in many important networks, for example, in transportation systems, biochemical reactions, scientific and movie-actor collaborations, and sexual contacts. We have provided the first example of a scale-free network in a model condensed-matter system.

Finally, we use genetic algorithms, a method for efficiently searching for minima on energy landscapes, to investigate the ordered equilibrium structures formed by binary mixtures of anisotropic dipolar particles confined on a plane, under the presence of an external magnetic field. The anisotropy of the interparticle forces is controlled by tilting the external magnetic field with respect to the plane. Initially, as the field is tilted the structures are only slightly perturbed, but once the anisotropy exceeds a critical value, completely new structures emerge.

Acknowledgments

I would like to thank my advisor Dr. Philip J. Camp for teaching me how to do research. His confidence in my work was very supportive and it encouraged me greatly. I always had the freedom to follow my own ideas, for which I am very grateful.

I would like to thank my (informal) advisor Dr. Vasileios Koutsos, who initiated the polymer projects. The fact that I could spend time in a different department gave me the opportunity to see things from a different perspective. Additionally, I would like to thank Dr. Emmanouil Glynos for the endless discussions about polymers and other subjects.

I would like to thank Prof. Christos N. Likos for giving me the chance to learn and work with genetic algorithms during a three month visit to the Department of Theoretical Physics, University of Düsseldorf, whose support via SFB and hospitality are gratefully acknowledged. In addition, I am grateful to Julia Fornleitner for valuable discussions about genetic algorithms.

Former and current colleagues from our group, namely Peter Duncan, Leonardo Lenoci and Georg Gunzemuller, never ceased to amazed me with their actions in our group meetings especially those abroad which were carefully planned and organised by our advisor, Dr. Philip J. Camp.

Finally but not least I thank for the financial support of the EPSRC and the School of Chemistry of the University of Edinburgh.

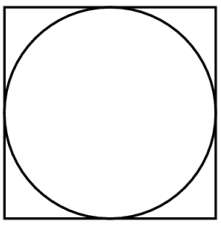

Contents

Chapter 1

Introduction

In the last decades soft matter has emerged as an important subfield of condensed matter physics. The term describes a rich variety of different substances whose common feature is that their properties are much more sensitive to mechanical stresses and thermal fluctuations than hard materials such as aluminium or sodium chloride. The predominant physical behaviour of soft materials occur at an energy scale comparable with thermal energy at room temperature, where quantum effects are unimportant. Nature's main materials come from soft matter; most biological materials such as blood, muscles, proteins/DNA, milk, and leaves are classifiable as soft matter. Soft materials can also be important in a wide range of technological applications. Since antiquity humans have used animal and plant fibres for their basic needs such as clothing and writing (papyrus, pergamon, and paper). Today one can find soft materials as structural and packaging materials, foams and adhesives, detergents and cosmetics, paints, food additives, lubricants, and fuel additives.

Perhaps the most fascinating aspect of soft matter is the interesting behaviour that arises in ways that cannot be predicted, or is difficult to predict, directly from its atomic or molecular constituents. This is often because soft matter self-organises into mesoscopic physical structures that are much larger than the microscopic scale (the arrangement of atoms and molecules), and yet are much smaller than the macroscopic dimensions of the material. In particular some of the microscopic factors can include a large number of internal degrees of freedom, weak interactions between structural elements, and a delicate balance between entropic and energetic contributions to the free energy. These properties lead to large thermal fluctuations, a wide variety of structural forms, sensitivity of equilibrium structures to external conditions, macroscopic softness, and metastable states. The overall properties and interactions of these mesoscopic structures determine the macroscopic behaviour of the material. For example, the Indians of the Amazon basin collect the sap from a

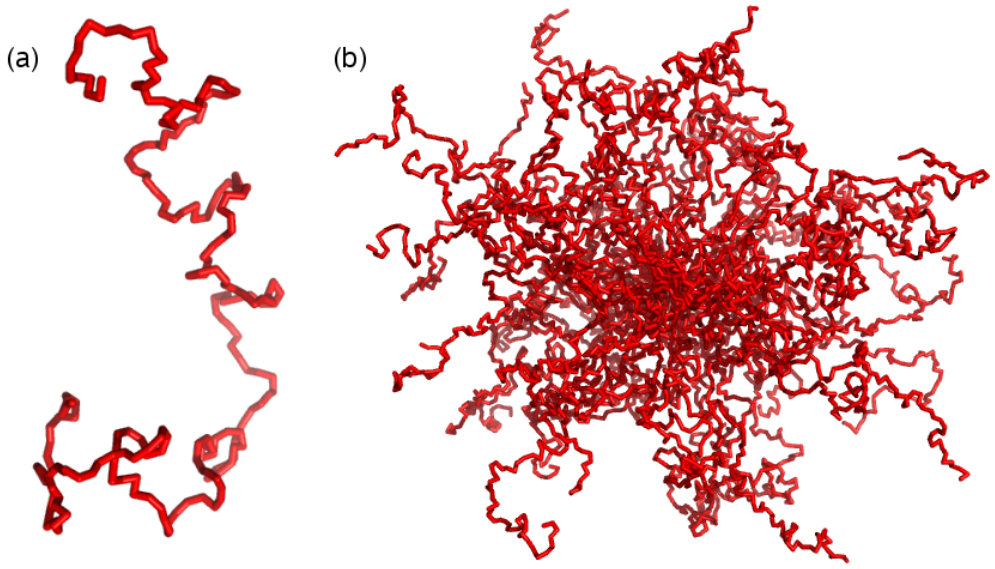

Figure 1.1: The figure shows screenshots of two types of polymers from computer simulations. (a) Linear polymer composed by 200 monomers; (b) a star polymer composed by 64 arms and 100 monomers per arm.

hevea tree and place it on their foot. After letting it dry for a short period of time, the material becomes a *boot*. From microscopic perspective the starting point is a set of independent, flexible polymer chains. The oxygen from the air builds in a few bridges between the chains, which transforms the material from the liquid state to a network structure which can resist tension. This material is known as rubber. Hence, soft matter is an exciting field in which even a mild chemical action can induce drastic changes on the properties of the material.

This thesis is devoted to the study of the self-organisation of some soft-matter systems. Two types of systems are studied here: polymers and colloidal monolayers.

1.1 Polymers

Polymers represent one of the outgrowths fields in soft matter. They are polyatomic molecules composed by small building blocks (a group of atoms), called monomers. The most fundamental topology of polymeric structure is a linear chain as seen in Fig. 1.1(a). One can generate new topologies by tethering the one end of chains to a d dimensional surface, for example $d = 0$ (point) creates a star polymer Fig. 1.1(b) and $d = 2$ (surface) creates a brush. To tether a chain at a two-dimensional surface is done with a chemical bond, whose monomer-surface interaction strength is $U \gg kT$. One such bond is strong enough to keep the rest of the chain tethered on the surface and significantly reducing its mobility. This is a type of adsorption called chemisorption.

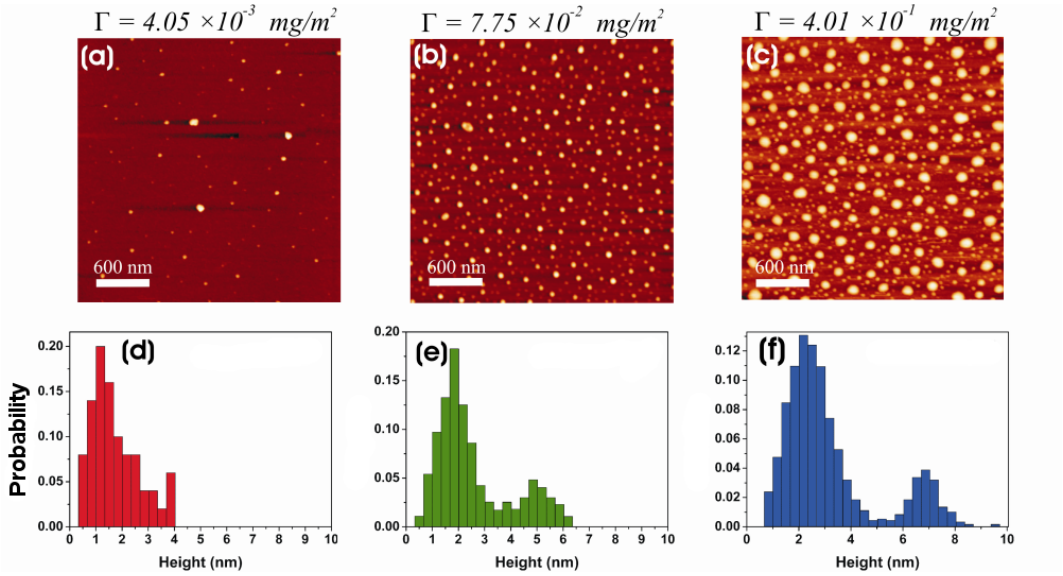

Figure 1.2: (a)-(c) AFM images of linear polybutadiene (molecular mass 78.8kg/mol) showing the patterns created after good-to-bad solvent transition occurs on adsorbed of a thin film polymers on a mica surface. The surfave covergage for each is $\Gamma = 4.05 \times 10^{-3}$, 7.75×10^{-2}, and 4.01×10^{-1} mg/m^2 respectively. (d)-(f) Cluster-height distributions correspoding to images (a)-(c), respectively. Pictures courtesy of Emmanouil Glynos.

Nevertheless, one can have an adsorbed polymer on a surface without tethering it. This can be achieved when the monomer-surface interaction strength is $U \sim kT$, meaning that these monomer-surface contacts can easily break. Adsorption occurs due to many monomer-surface interactions. The resulting conformational relaxation of the polymer is driven by the competition between the entropic due to loss of conformational freedom, and the drop in energy from binding monomers to the surface. This type of adsorption is called physisorption. Polymer physisorption from dilute solution has been frequently studied in the past, but to the best knowledge of the author no previous studies have focused on the pattern formation of the physisorbed polymers from a good solvent-to-bad solvent quenching transition. In a collaboration with E. Glynos and V. Koutsos of the School of Engineering of University of Edinburgh, patterns have been observed with atomic-force microscopic (AFM), in which two types of polymers were studied, linear [1] and star polymers [2]. The AFM images, in case of linear polymers, reveal a bimodal cluster distribution under certain experimental conditions, see Fig. 1.2. Like in the Amazonian boots example above it is easy to imagine what is happening. Before the good-to-bad solvent transition, the chain spread on the surface to maximise their monomer contacts with the surface. Additionally being in good solvent conditions the monomer-solvent interaction is

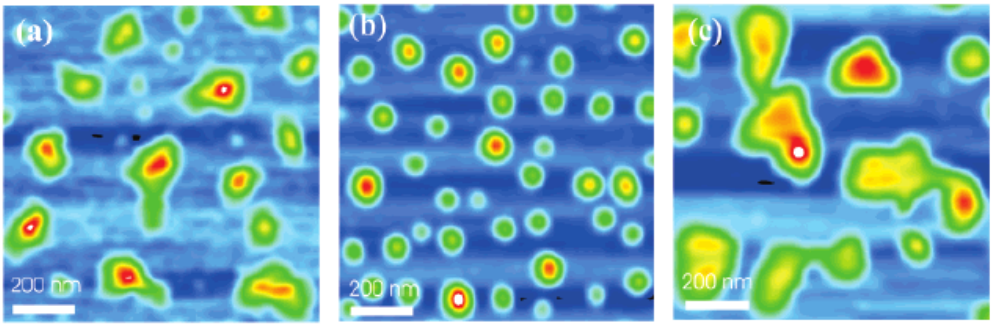

Figure 1.3: High-contrast AFM images in air, $1 \times 1 \mu m^2$, showing the patterns created after good-to-bad solvent occured at adsorbed star polymers on a mica surface. From image (a) to (c) the adsorbed amount is 0.104, 0.304 and 1.75 mg/m^2, respectively. Pictures courtesy of Emmanouil Glynos

attractive, which makes the chain soluble. However, once entered into bad-solvent conditions the monomer-solvent interactions becomes repulsive. Hence, the chain collapses into a structure that minimises the surface contact with the solvent. For low surface density each chain behaves as if it was an isolated chain, since it does not feel the presence of the other chains. Therefore once the good-to-bad solvent transition occurs each chain will collapse into itself leading to a cluster distribution dominated by single collapsed chains. Nevertheless, for higher surface density, an extra entropic term affecting the chain conformation is needed, which describes the competition for space between different chains. When the the good-to-bad solvent transition occurs at high surface density the chains are already close to each other by having monomer-monomer contacts or even entanglements for long chains, and that leads to the creation of many-chain clusters. One should expect that there is an intermediate regime in which both clusters and single collapsed chains are observed. In chapter 3 we demonstrate that this type of distribution can be reproduced with computer simulations and we rationalise the observed AFM structures on the basis of the polymer structures prior to the quench.

AFM experiments have also been performed with star polymers, see Fig. 1.3. Star polymers are a special case of branched polymers where a star is composed by f flexible polymer chains tethered to a core. f is called functionality. The functionality governs the star's behaviour from a linear chain for $f = 1$ and 2 to a colloidal particle for $f \gg 1$. In other words, a star polymer is a hybrid between polymer-like objects and colloidal particles, hence bridging two different domains of physics. A great interest has been evoked recently on how stars behave in the proximity of a substrate. For example it is interesting to understand how stars can act as depleting agents of colloidal particles, in other words to prevent colloidal aggregation and with an

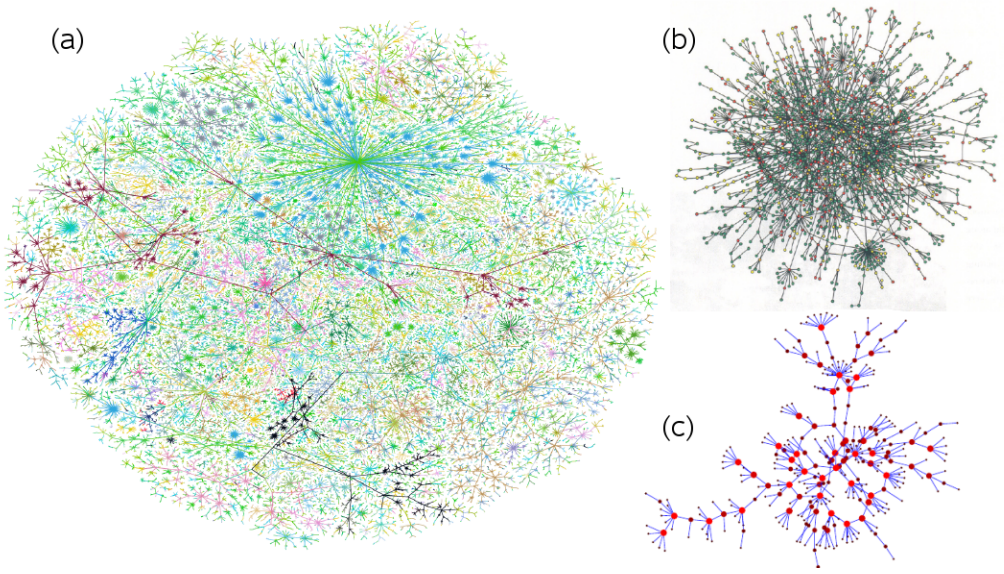

Figure 1.4: Three examples of the kinds of scale-free networks. (a) A vizualization of the network structure of the Internet at the level of autonomous systems. (b) A map of interacting proteins. (c) A social network, in the case of sexual contacts. The images were taken from the Refs. [6, 7].

ultimate goal to assemble the colloids into ordered structures [3, 4, 5]. However, it is still an unexplored region on how star polymers behave in the proximity of an attractive surface. In chapter 4 we discuss how a surface can affect the conformation of a physisorbed star. Measurements from computer simulations of the fraction of monomers bound to the surface, height, radius of gyration, and asphericity provide valuable insights on a star polymer's conformations. We rationalise on the basis of the results and it will allow us to map a star's behaviour (from linear to soft-colloid) based on the number of arms and their length, and the properties of the surface. The mapping the behavior of an adsorbed star polymer on a surface provides us valuable insights and can act as a guide to predicting a star's conformation on a surface for future experiments.

1.2 Scale-free neighbour networks in polydisperse 2D fluids

Polydisperse hard-disk fluids are of considerable interest as model of soft matter systems, for example, as models of colloidal monolayers, froths and foams, and of packing and segregation in granular materials. In particular we focus on the neighbour network of a two-dimensional polydisperse hard-disk fluid with a power

law diameter distribution. The aims are twofold. First we want to understand how a diameter distribution with a slowly decaying tail, as it happens to power laws and in contrast with exponential distributions, will affect the neighbour network. It is tempting to speculate that if the diameter distribution follows a power law, then perhaps the network distribution will also vary in a similar way. The assumption is that for any given disk the number of immediate neighbours will be proportional to its circumference and hence its diameter. And second if the neighbour network does vary with a power law then does it also have the properties of scale-free networks? Scale-free networks are characterised in qualitative terms by a small number of highly connected vertices called "hubs" and a large number of low connected vertices, see Refs. [6, 7]. Some examples of real scale-free networks are illustrated in Fig. 1.4. The degree distribution (i.e. the probability of finding a vertex with k connections) varies with a power law, a necessary but not sufficient condition for a network to be scale-free. Many physical systems have been identified as scale free, for example the World Wide Web, the Internet, metabolic and protein-protein interactions, sexual contacts, collaborations among scientists. But what makes scale-free networks fascinating is that they have self-similar behaviour. For example, in a self-similar network where the vertices are connected with edges (connections of links) there is no possible way to assess whether a vertex has an above or below average number of connections.[1] This happens because power law distributions with slow decaying tails have infinite mean, thus there is no characteristic scale to use for comparison. In chapter 5 we examine the polydisperse hard-disk fluid by using constant-pressure Monte Carlo simulations. Additional measurements are discussed in the chapter such as the assortativity of the network, which is found to be positive, meaning that vertices of equal degree are connected more often than in a random network. Finally, the equation of state is determined and compared with the prediction from a scaled-particle theory.

1.3 Colloidal monolayers with dipolar interactions

In the final part of the thesis, we look at two-dimensional binary mixtures of dipolar colloids. A popular description of colloids is that they are particles with the simplest and highest possible symmetry (sphere), and without any additional structure on the mesoscopic length scale, see Fig. 1.5. It is possible experimentally to insert within the colloid a magnetised substance and thus effectively create a colloid carrying a point magnetic dipole. The importance of this is for example creating new type of polymers where its monomers are colloids; or one can use external fields and take

[1] A finite size network will be bounded by a minimum and maximum degree, which can give a finite mean. The self-similarity manifests between the bounds.

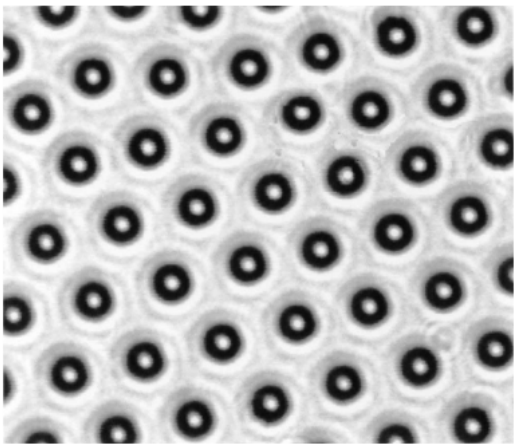

Figure 1.5: Optical micrograph of a monolayer of polystyrene spheres, with diameter 2.7μm, at the interface between water and a mixture of decane and undecane in the through. The picure is taken from the Ref. [8].

advantage of the long range repulsive forces (from dipole-dipole interactions) to create well disperse colloidal particles in the substance of interest. In chapter 6 we are interested in what are the global minimum-energy configurations of a binary mixture of dipolar colloids confined to a flat interface, and with a magnetic field is applied perpendicular direction polarising the particles and inducing long range repulsive interactions between them. We use genetic algorithms to efficiently search the global minimum of energy landscapes; genetic algorithms are described in the methodology of chapter 6.

1.4 Summary

This thesis is organised as follows. In chapter 2 we briefly summarise key concepts in statistical mechanics, computer simulations, polymers and fractals that underpin this thesis. In chapters 3 and 4 we study the self-assembly of physisorbed linear and star polymers, respectively. In chapter 5 we look at the behaviour of the neighbour network of a two-dimensional polydisperse hard-disk fluid with slow decaying diameter distribution. In chapter 6 we examine ordered equilibrium structures formed by binary mixture of anisotropic dipolar particles confined on a plane, under the presence of an external magnetic field. Finally, in chapter 7 we conclude this thesis.

Chapter 2

General Considerations

Science is the systematic observation and understanding of Nature. Until recently there were two ways one could understand Nature. The first was to perform experiments, for example by recording the time for a falling apple from different heights to hit the ground. The second method is by developing a theory. Theory takes mathematics and constructs a framework in which a model can be built and studied. Thus, in the case of a falling apple (or more precisely the orbits of planets) Newton developed the theory of gravity, which explains how the apple falls, and planets orbit around the sun rather than crushing each other. Theories can be tested by comparing their predictions with experimental results. Disagreement between experimental results and theoretical predictions can lead to a new theory, as happened in the 19^{th} century when Mercury's peculiar trajectory was first observed and led to Einstein's theory of general relativity.

The development of computers has provided an alternative mode of research in science. Computer simulations can be used as a linking bridge between theory and experiments. Mathematical in nature, computer simulations provide a new metaphor for the laws of Nature, the algorithms. The first systematic explorations with computers occurred in 1952, with Metropolis being interested in having the Los Alamos MANIAC machine tried against a wide spectrum of mathematical and physical problems. However, simulations, or to be more accurate algorithms, which are the heart of computer simulations, are not *new* discoveries. The ancients used algorithms to gain insights into difficult mathematical or physical problems; one example is the Euclidean algorithm, which determines the greatest common divisor in any Euclidean domain (i.e. integers). Simulations can easily examine different theories and visualise the results thus providing valuable insights. Furthermore, they can aid in interpreting experimental results, and in devising new experimental strategies.

In the case of many-body problems, computer simulations of condensed-matter systems frequently use statistical mechanics. Statistical mechanics is the discipline that connects the microscopic variables (positions, momenta, and interactions) of a physical system to its macroscopic ones (temperature, pressure, etc.). Many simple problems in statistical mechanics are exactly solvable, but only a handful of non-trivial problems can actually be solved exactly. Other problems can be tackled by using successive approximations, and perturbative expansions; computers play an important role in such work, for instance in calculating virial coefficients, understanding polymer conformations, and so on.

Polymer physics is founded upon the principles of statistical mechanics, which studies the structural and dynamical properties of polymers. It is a relatively old field (starting in 1920), but since then it has become a fundamental part of statistical mechanics providing great insights into understanding polymers like DNA and designing new exotic materials. One of these insights was that polymers are finite *fractals*, which corresponds to geometrical objects whose geometry is invariant on all scales.

In this chapter we briefly summarise the key concepts in statistical mechanics, computer simulations, polymers and fractals that underpin this thesis.

2.1 Statistical physics

Statistical mechanics is a probability theory which provides mathematical tools for dealing with systems of many particles. It is able to predict statistics (averages, fluctuations) for the macroscopic properties (such as for instance, pressure and temperature) of a many-body system from its microscopic properties, such as interactions.

2.1.1 Ensembles

Statistical mechanics groups many-body systems into *ensembles*. An ensemble in statistical mechanics consists of a very large (theoretically infinite) number of copies of a system, all characterised by the macroscopic varibles. There are four ensembles that are commonly used. (a) The *micro-canonical* ensemble is a group of systems characterized by a fixed number of particles N, total energy E, and in volume V. This ensemble is often denoted as the NVE ensemble and consists of copies of an isolated system. (b) The *canonical* ensemble consists of many-body systems with equal number of particles N, which are at thermal equilibrium with a heat bath at temperature T, and at the same volume V. This ensemble exchanges energy with the

heat bath and is denoted as the NVT ensemble. (c) The *grand-canonical* ensemble is a collection of identical systems at equilibrium with an external reservoir with which they exchange both energy and particles. This ensemble is refered to as the μVT ensemble, where μ is the chemical potential controlling the average in the number of particles. (d) In the *isothermal-isobaric* ensemble, all the systems have the same number of particles N and maintain the same temperature T and pressure P. It is refered to as the NPT ensemble and it plays an important role in chemistry as many chemical systems are prepared and studied under conditions of constant temperature and pressure.

2.1.2 Time averages and ensemble averages

The microscopic states (positions $\mathbf{r}$ and momenta $\mathbf{p}$) of a many-particle system can be represented in *phase space*. In the case of a three-dimensional system of N particles, the values assumed by the variables $\mathbf{r}^N$ and $\mathbf{p}^N$ at any time define a point in the $6N$-dimensional phase space. A set of points in phase space linked by dynamical equations of motion define a trajectory.

If $\mathscr{A}\left(\mathbf{r}^N, \mathbf{p}^N\right)$ is a function of the $6N$ coordinates and momenta, its time average over a period τ is defined as

$$\langle \mathscr{A} \rangle_t = \lim_{\tau \to \infty} \frac{1}{\tau} \int_0^\tau \left[\mathscr{A}\left(\mathbf{r}^N, \mathbf{p}^N\right) \right] dt \tag{2.1}$$

A different averaging procedure based on the concept of ensemble can also be introduced. The average properties of a system can be obtained from a single "snapshot", rather than tracking the system's configurations through time. Hence, we use a function describing the distribution in phase space at time t of the phase points relative to a certain statistical-mechanical ensemble. This function is called *probability density*, $f\left(\mathbf{r}^N, \mathbf{p}^N, t\right)$. Under equilibrium conditions f is independent of time and ensemble averages can be defined as follows

$$\langle \mathscr{A} \rangle_e = \iint \mathscr{A}\left(\mathbf{r}^N, \mathbf{p}^N\right) f\left(\mathbf{r}^N, \mathbf{p}^N, t\right) d\mathbf{r}^N d\mathbf{p}^N \tag{2.2}$$

If the average in eq. 2.1 is performed over a long time, and the system eventually flows through all its possible microstates, then the ensemble averages become the same as the time averages, that is

$$\langle \mathscr{A} \rangle_t = \langle \mathscr{A} \rangle_e \tag{2.3}$$

This equivalence is known as the *ergodic* theorem and it is believed to hold for all

many-body systems in Nature.

2.2 Simulation Techniques

In this section, we discuss a few computational tricks that are of great practical importance for an efficient simulation program. Additionally, we discuss some fundamental concepts in computer simulations such as how Monte Carlo and molecular dynamics algorithms work.

2.2.1 Interaction potentials

We describe our model of the system of interest by a function which gives the potential energy for a given configuration of the particles in the system. Usually, the assumption is made that the potential is pairwise additive. That is, we assume that the total potential is just the sum of potential for each pair of particles, which is expressed as a function of their relative positions (and possible orientations). This is justified because three-body (or higher order) terms in the potetial give a small contribution into the description of the overall system. More details can be found in Refs. [9, 10].

Perhaps the simplest model of a particle is to regard it as an impenetrable hard sphere and it is represented by the potential

$$U(r) = \begin{cases} \infty & r < \sigma \\ 0 & r > \sigma \end{cases} \tag{2.4}$$

where r is the distance between the particles and σ is the particle diameter. The hard core interaction which prevents the particles from overlapping provides a good representation of the Pauli repulsion which operates at short distances and has its origin in the exclusion principle. Another, widely used pair potential is the Lennard-Jones potential,

$$U(r) = 4\varepsilon \left[\left(\frac{\sigma}{r}\right)^{12} - \left(\frac{\sigma}{r}\right)^{6} \right] \tag{2.5}$$

where r is the distance between the particles, σ is the distance parameter and ε is a parameter giving the depth of the minimum in the potential. At large distances, this has the asymptotic $1/r^6$ dependence of the van der Waals interaction, and the $1/r^{12}$ term approximately describes the hard-core repulsion when the particles come close together. This potential provides an excellent description for argon and it is frequently used for many other molecules.

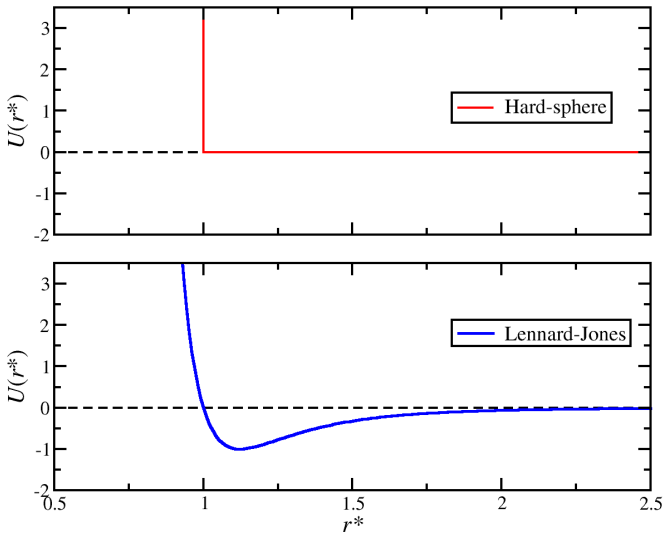

Figure 2.1: The diagrams display the the hard-sphere potential (top) and Lennard-Jones potential (bottom).

For short-range potentials, we can truncate the potential at a certain distance beyond which the interactions are negligible. This means that any two particles further apart than this distance do not need to be considered when calculating the total potential energy, speeding up the simulation. The discontinuity in the potential can cause problems, however. A discontinuous potential means an infinite force (since $\mathbf{F} = -\nabla U$), which can lead to numerical instabilities. One way to avoid this is to shift the potential in the vicinity of the cut-off by a function which brings it smoothly to zero.

2.2.2 Reduced Units

When carrying out a computer simulation it is convenient to define a set of reduced units in terms of the potential parameters of the system under study. For example, for Lennard-Jones fluid, with the pair potential given in Eq. 2.5, distances can be expressed in terms of the parameter σ, and energies can be expressed in terms of ε. We also use the mass of the particles in the system as a fundamental unit (i.e. $m = 1$). From these fundamental definitions, we can obtain other quantities in reduced units. Some reduced units for the Lennard-Jones potential are listed in Table 2.1.

The most important reason for using reduced units is that there are many different states in real units that corresponds to the same state in reduced units. The use of reduced units means we do not have to repeat the simulation for each of these states. Another advantage is that values in reduced units will be of order unity, hence we

Table 2.1: Properties of Lennard-Jones system in reduced units.

Quantity	Reduced Unit
Distance	$r^* = r/\sigma$
Density	$\rho^* = \rho\sigma^3$
Energy	$E^* = E/\varepsilon$
Temperature	$T^* = k_B T/\varepsilon$
Pressure	$P^* = P\sigma^3/\varepsilon$
Time	$t^* = (\varepsilon/m\sigma^2)^{1/2} t$

avoid the potential problems of using the very small numbers of atomic systems on a computer. The use of reduced units also simplifies the potential, allowing us to set the parameters of the potential to one. We do not need to choose specific values of these parameters.

2.2.3 Periodic Boundary Conditions

In a simulation of finite number of particles, a significant fraction of particles will be at the edges of the system. The environment of these particles will be very different to the environment of a particle within the bulk system. In order to reduce this problem, periodic boundary conditions are normally employed. We make copies of the system in all directions, see Fig. 2.2. When a particle leaves the central simulation cell at one side, its periodic image enters from the other side, thus conserving the number of particles in the central simulation cell. Technically, every particle interacts with every particle in all cells, but often the minimum image convention is used. When calculating the force and the interactions on a pair of particles, the only interaction that is considered is that due to the nearest of the periodic images of the particular particle.

2.2.4 Monte Carlo

Monte Carlo methods aim to generate a trajectory in phase space which samples from a chosen statistical-mechanical ensemble. The ensemble average of a certain quantity $\mathscr{A}$ is then calculated via

$$\langle \mathscr{A} \rangle = \frac{1}{Q} \sum_i \mathscr{A}_i \exp(-\beta E_i) \tag{2.6}$$

where $Q = \sum_i \exp\left(-\beta E_i\right)$ is the partition function, $\beta = 1/k_B T$ and $\exp\left(-\beta E_i\right)$ is the Boltzmann factor which weights every accessible state i of energy E_i. However, the

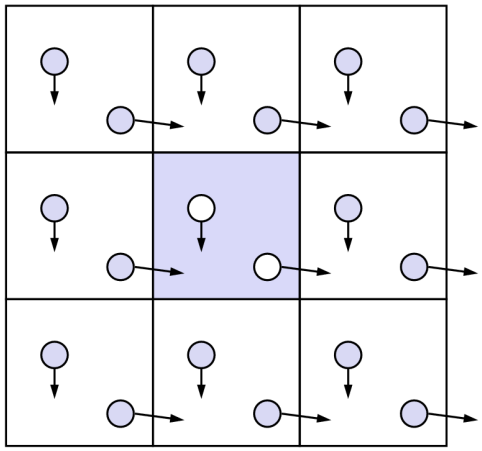

Figure 2.2: Schematic illustration of periodic boundary conditions.

number of accessible states in a large system can be huge thus making the exact evaluation of the average in eq. 2.6 unfeasible with current computers. Moreover, certain states (those with small Boltzmann factor) contribute very little to the average, and hence should be omitted in an efficient calculation. To overcome these problems, *importance-sampling* is employed. In this scheme the only configurations to be sampled are those that make a significant contribution to the partition function and ensemble averages. This task is achieved by generating a *Markov* chain of configurations in which each state is generated by "perturbing" the preceding one in the chain, and accepted as a new configuration only if the *detailed balance* condition is satisfied.

A sufficient (but not necessary) detailed-balance condition is that for old (o) and new n states

$$J(o \to n) = J(n \to o) \tag{2.7}$$

where $J(o \to n)$ is the probability flux from a state o to a new state n during a given simulation step. The flux $J(o \to n)$ can be factored into three terms

$$J(o \to n) = p(o) \cdot \alpha(o \to n) \cdot acc(o \to n) \tag{2.8}$$

where $p(o)$ is the probability of being in state o (which at equilibrium should follow the Boltzmann distibution), $\alpha(o \to n)$ is the probability of generating the trial move from o to n, and $acc(o \to n)$ is the probability of accepting the trial move from o and n. By combining eqs. 2.7 and 2.8 the detailed-balance condition can be rewritten as

$$\frac{acc(o \to n)}{acc(n \to o)} = \frac{acc(n \to o)}{acc(o \to n)} \cdot \frac{p(n)}{p(o)} \tag{2.9}$$

where $\frac{p(n)}{p(o)}$ is obtained based on the statistical ensemble we work on. In the case of NVT ensemble the ratio can be expressed as the Boltzmann factor of the energy difference:

$$\frac{p(n)}{p(o)} = \frac{Z_{NVT}^{-1} e^{-\beta E(n)}}{Z_{NVT}^{-1} e^{-\beta E(o)}} = e^{-\beta[E(n)-E(o)]} \tag{2.10}$$

where $E(n)$ and $E(o)$ are the system energies for the new and old state, respectively. Z_{NVT} is the partion function defined as the sum of all the energy states, E_i, and read as $Z_{NVT} = \sum e^{-\beta E_i}$. Now if we assume that $\alpha(o \to n) = \alpha(n \to o)$, then eq. 2.9 becomes

$$acc(o \to n) = \min\left(1, e^{-\beta[E(n)-E(o)]}\right). \tag{2.11}$$

A typical importance-sampling Monte Carlo scheme to perform a simulation in the canonical (NVT) ensemble will proceed as follows. The system is prepared in some initial configuration. A particle is chosen randomly and displaced within the simulation cell. If the trial move results in a decrease of the system energy, then the move is accepted and the particle positions updated. If the trial move results in an increase of energy, instead, the move is accepted with probability $\exp(-\beta\Delta E)$, where ΔE is the difference in system energy associated with the trial move. This is implemented in a computer simulation by generating a random number in the interval $(0,1)$ and accepting the move only if the random number is less than the value $\exp(-\beta\Delta E)$. These steps are repeated for the subsequent randomly chosen particles. After a large number of trial moves, simple unweighted averages over the visited states can be calculated since each state is sampled with a probability proportional to its Boltzmann factor.

2.2.5 Molecular dynamics

Molecular dynamics (MD) simulations is a classical technique to compute equilibrium structural and dynamical properties of a many-body system.

In this technique each particle moves according to Newton's laws of motion, which are integrated numerically. The positions and velocities of the particles are updated every time-step and the equations of motion integrated to generate a trajectory in phase space. This procedure is repeated for a number of time-steps required to equilibrate the system and calculate accurate time averages.

A typical MD simulation will proceed as follows: positions $\mathbf{r}_i$ and velocities $\mathbf{v}_i$ of the particles at time t are stored in the computer. The force acting on each particle is calculated from the potentials ($\mathbf{F}_i = -\nabla_i U$) and then the equation of motion, $\mathbf{F}_i = m_i \mathbf{a}_i$, is integrated over a finite time-step Δt according, for instance, to the Verlet algorithm to get the position of the particles in the next time-step, $t + \delta t$ [9]

$$\mathbf{r}_i(t+\delta t) = \mathbf{r}_i(t) - \mathbf{r}_i(t-\delta t) + \mathbf{a}_i(t)\delta t^2 \tag{2.12}$$

The velocities are calculated separately from the positions as follows:

$$\mathbf{v}_i(t) = \frac{\mathbf{r}_i(t+\delta t) - \mathbf{r}_i(t-\delta t)}{2\delta t} \tag{2.13}$$

The numerical integration of the equations of motion using the Verlet algorithm and its variants generates errors of order δt^4 in the positions and δt^2 in the velocities.

A better integration algorithm is the so-called "velocity-Verlet", which computes more accurately the velocities (the errors is of order δt^4) and it reads as

$$\mathbf{r}_i(t+\delta t) = \mathbf{r}_i(t) + \mathbf{v}_i(t)\delta t + \frac{1}{2}\mathbf{a}_i(t)\delta t^2 \tag{2.14}$$

$$\mathbf{v}_i(t+\delta t) = \mathbf{v}_i(t) + \frac{1}{2}\left[\mathbf{a}_i(t) + \mathbf{a}_i(t+\delta t)\right]\delta t. \tag{2.15}$$

The original Verlet algorithm may be recovered by eliminating the velocities. The algorithm only requires storage of $\mathbf{r}_i$, $\mathbf{v}_i$ and $\mathbf{a}_i$ and its implementation involves two stages, with the force evaluation in between. First, the new positions at time $t+\delta t$ are calculated using eq. 2.14 and then the forces and accelerations at time $t+\delta t$ are computed. At this point the velocities at time $t+\delta t$ are available. The origin of eq. 2.15 comes by calculating the velocities at mid-step i.e. at time $t+\frac{1}{2}\delta t$

$$\mathbf{v}_i(t+\frac{1}{2}\delta t) = \mathbf{v}_i(t) + \frac{1}{2}\mathbf{a}_i(t)\delta t \tag{2.16}$$

and at time $t+\delta t$

$$\mathbf{v}_i(t+\delta t) = \mathbf{v}_i(t+\frac{1}{2}\delta t) + \frac{1}{2}\mathbf{a}_i(t+\delta t)\delta t. \tag{2.17}$$

Combining eqs. 2.16 and 2.17, we obtain eq. 2.15.

Overall, the Verlet algorithms for most MD simulations are perfectly adequate. The success of Verlet algorithms relies on their simplectic character, meaning that it has a time-reversal symmetry and long-term energy conservation.

In a standard MD simulation total energy and momentum are conserved quantities. A typical MD program simulates a microcanonical ensemble (constant NVE). MD simulations can also be performed in constant-temperature ensembles, such as NVT (canonical ensemble), and NPT (where P is the system pressure). In these cases the temperature T is kept constant by coupling the system to a heat bath. A detailed review of constant-temperature MD methods is given in Refs. [9] and [11].

2.2.6 Brownian dynamics

An alternative simulation technique that keeps the system temperature constant is Brownian dynamics (BD).

In the presence of large time-scale separations between the rapid motion of the solvent and the slower motion of the solute, such as in the case of polymers, amphiphile and colloidal suspensions, the simulation time can became prohibitively long. In fact, the short time steps needed to capture the fast motion of the solvent, and the long runs needed to study the structural evolution of the solute, can make simulations very time consuming, especially in those cases in which the fast solvent modes are not of interest. BD is a mesoscale simulation technique in which solvent particles are replaced by a combination of stochastic and frictional forces.

At the very core of this technique there is the integration of the Langevin equation in order to generate trajectories of the solute particles in which we are interested, letting friction and random terms to mimic the solvent interactions with the solute. The Langevin equation in this situation is written

$$\mathbf{F}_i = -\nabla_i U - \xi m_i \mathbf{v}_i + \mathbf{W}_i \tag{2.18}$$

where $\mathbf{v}_i$ is the velocity of particle i, U is the total potential energy, ξ and $\mathbf{W}_i$ are the friction coefficient and the random force representing the effects of the solvent. The random force is, in a typical BD simulation, Gaussian noise, which obeys the fluctuation-dissipation theorem

$$\begin{aligned} \langle \mathbf{W}_i(t) \rangle &= 0 \\ \langle \mathbf{W}_i(t) \cdot \mathbf{W}_j(t') \rangle &= 6mk_BT\xi\delta_{ij}\delta(t-t'). \end{aligned} \tag{2.19}$$

The Langevin equation 2.18 can be integrated numerically, for example using a Verlet-like algorithm. The friction coefficient ξ is related to the single-particle diffusion coefficient D accordingly to Einstein's equation

$$\xi = \frac{k_B T}{mD} \tag{2.20}$$

where k_B is the Boltzmann's constant and m is the mass of the diffusing particle.

Hydrodynamic effects, that is the influence of one particle on another through the flow of the solvent around them, and the interaction between two particles due to solvent structure, can be included in this simulation scheme. Details are in Refs. [9, 12, 13].

2.3 Polymers and Scaling Theory

The development of human civilisation has been dictated by the availability of materials. In fact, the discovery of a new material can have such drastic effects as to lead to the decline of an old civilizations and give the rise to a new one. For this reason history is divided into eras named after the primary materials used; the *Stone Age*, the *Bronze Age*, and the *Iron Age*. Similarly, we can say that in the 20^{th} century we entered the *Polymer Age*.

In this section we will discuss the definition of a polymer, and review some universal properties of linear chains.

2.3.1 Definition and structure

Polymers are macromolecules (polyatomic structures) consisting of many elementary units, called *monomers*, and they are connected to each other by covenant bonds. The entire structure of a polymer is generated through the process of *polymerisation*, the process by which elementary units are covalently bonded together. The number of monomers in a polymer molecule is called the *degree of polymerisation*, N. For example, polyethylene's repeating unit is $-CH_2-CH_2-$, since the monomers used in their synthesis are ethylene, $CH_2=CH_2$, see Fig. 2.3.

The definition of a polymers is generic and includes a huge variety of polymers with distinct structural and architectural features, such as DNA and polypetides; these features change the physical properties of the molecules. For instance both the boiling point and the melting point increase rapidly with the number of backbone monomers. We briefly describe some of the ways of categorising these structures. The first way of categorising a polymer is by the number of different types of monomers in the molecule. If a polymer contains only one type of monomer, then it is called a *homopolymer*, otherwise it is called a *heteropolymer*. Heteropolymers have a whole range of subcategories depending on the number of different types of monomers and their position in the molecule. For example, for two types of monomers, say A and B, then you can have different sequences of monomers, e.g. *alternating* ...-A-B-A-B-A-B-A-..., *random* ...-A-A-B-B-B-A-B-..., *diblock* ...-A-A-A-B-B-B-... chains.

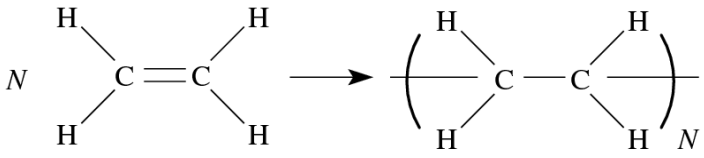

Figure 2.3: Polymerization of polyethylene monomers.

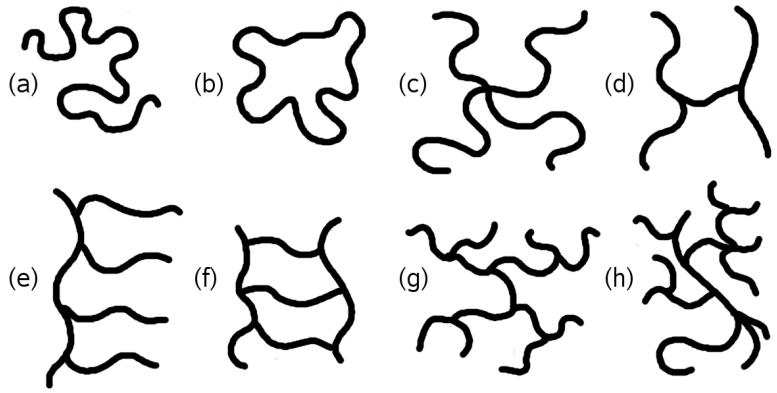

Figure 2.4: Examples of polymer architectures (a) linear; (b) ring; (c) star (d) H; (e) comb; (f) ladder (g) dentrimer; (h) randomly branched.

The second was by which one can categorise polymers is by their size. *Oligomers* are polymers consisting of a small number of monomers (generally, less than 20); polymers may contain between 20 and 10 billion (for the longest known chromosome) monomers. Third, another important way of characterising of polymeric systems is by their architecture. Types of polymer architectures include linear, ring, star-branched, H-branched, comb, ladder, dendrimer or randomly branched, see Fig. 2.4. The properties of branching and the formation of networks (via a high degree of crosslinking) make polymers useful as soft solids (e.g. erasers, tyres).

2.3.2 Polymer conformations

To understand the thermodynamic and dynamical properties of polymers, one has to look first to the possible conformations. The simplest model that describes a linear polymer is a *freely joined chain*. The model represents the polymer as a chain of $n+1$ identical monomers with a constant bond length $|\mathbf{r}_i| = l$, see Fig. 2.5. Moreover, we make an assumption that the chain is in an *ideal* state, meaning that there are no interactions between the monomers separated by a large number of bonds along the chain, so that $|i-j| \gg 1$.

We define the *end-to-end vector*, which is the sum of all n bond vectors $\mathbf{r}_i$ in the chain:

$$\mathbf{R}_n = \sum_{i=1}^{n} \mathbf{r}_i \tag{2.21}$$

Different configurations of the chain will have different bond vectors and hence different end-to-end vectors. However, the ensemble average of $\mathbf{R}_n$ over all possible states by either considering many chains or many different configurations of the

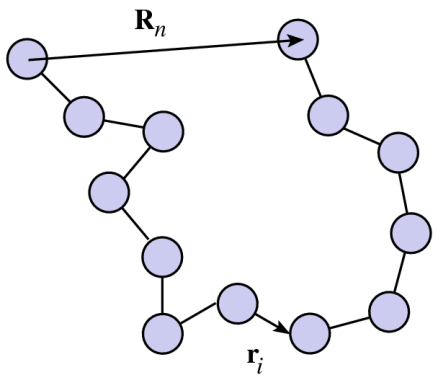

Figure 2.5: Schematic illustration of a conformation of a linear polymer.

same chain, is zero

$$\langle \mathbf{R}_n \rangle = 0 \tag{2.22}$$

which signifies that there is no preferred direction in this ensemble. The simplest non-zero average is the mean-square end-to-end distance:

$$\langle R^2 \rangle = \left\langle \left(\sum_i^n \mathbf{r}_i \right) \cdot \left(\sum_j^n \mathbf{r}_j \right) \right\rangle = \sum_{i=1}^n \sum_{j=1}^n \langle \mathbf{r}_i \cdot \mathbf{r}_j \rangle \tag{2.23}$$

If all bonds have the same length $l = |\mathbf{r}_i|$, then the scalar product can be represent in terms of the angle θ_{ij} between bond vectors $\mathbf{r}_i$ and $\mathbf{r}_j$

$$\mathbf{r}_i \cdot \mathbf{r}_j = l^2 \cos\theta_{ij} \tag{2.24}$$

The mean-square end-to-end distance becomes a double sum of average cosines:

$$\langle R^2 \rangle = l^2 \sum_{i=1}^n \sum_{j=1}^n \langle \cos\theta_{ij} \rangle \tag{2.25}$$

In the freely joined chain model there are no correlations between the directions of different bond vectors, thus $\langle \cos\theta_{ij} \rangle = 0$ for $i \neq j$. There are only n non-zero terms in the double sum ($\cos\theta_{ij} = 1$ for $i = j$). Therefore, $\langle R^2 \rangle$ of a freely joined chain is quite simple:

$$\langle R^2 \rangle = nl^2 \tag{2.26}$$

However, in a typical polymer chain, there are correlations between bond vectors (especially between neighbouring ones), so $\langle \cos\theta_{ij} \rangle \neq 0$. So one can group these

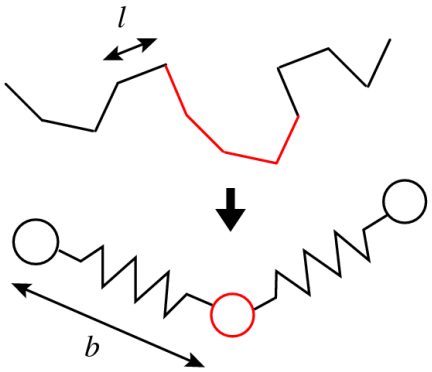

Figure 2.6: Schematic illustration of mapping a linear chain (continuous line) to an ideal flexible chain composed by effective bond of Kuhn length, b.

correlations into one quantity

$$C_n = \frac{1}{n}\sum_{i=1}^{n}\sum_{j=1}^{n}\langle\cos\theta_{ij}\rangle \tag{2.27}$$

where the coeffiecient C_n, called Flory's characteristic ratio, is the average value of the $\sum_{j=1}^{n}\langle\cos\theta_{ij}\rangle$ over all main-chain bonds of the polymer. Now eq. 2.25 can be reduced to

$$\langle R^2\rangle = l^2\sum_{i=1}^{n}\sum_{j=1}^{n}\langle\cos\theta_{ij}\rangle = C_n n l^2 \tag{2.28}$$

All real polymers have $C_n > 1$, meaning that the local correlations are significant i.e. $\langle\cos\theta_{ij}\rangle \neq 0$, which means that the local alignment of the bonds favours a parallel orientation. The physical origins of these local correlations between the bond vectors are restricted bond angles and steric hindrance. All models of ideal-chain polymers ignore steric hindrance between monomers separated by many bonds. This has as a result for a chain with large numbers of main chain bonds ($n \to \infty$) their characteristic ratios to saturate $C_\infty = \lim_{n\to\infty} C_n$. Thus, $\langle R^2\rangle$ can be approximated for long chains by

$$\langle R^2\rangle \cong C_\infty n l^2 \tag{2.29}$$

The values of the characteristic ratios of some common polymers are listed in Table 2.2.

The Flory characteristic ratio allows a simple description of all ideal polymers by an *equivalent freely joined chain*. The equivalent chain has the same mean-square end-to-end distance $\langle R^2\rangle$ and the same maximum end-to-end distance $R_{\max}$ as the actual polymer, but has N freely-joined effective bonds of length b, see Fig. 2.6. This

Table 2.2: Characteristic ratios, and Kuhn lengths for common polymers

Polymer	Monomer	C_∞	b (Å)
1,4-Polybutadiene (PB)	$-(CH_2CH=CHCH_2)-$	5.3	9.6
Poly(ethylene oxide) (PEO)	$-(CH_2CH_2O)-$	6.7	11
Atactic polystyrene (PS)	$-(CH_2CHC_6H_5)-$	9.5	18

effective bond length b is called the *Kuhn length*. Therfore, the Kuhn length for an equivalent freely joined chain is given by

$$b = \frac{\langle R^2 \rangle}{R_{\max}} = \frac{C_\infty n l^2}{R_{\max}} \tag{2.30}$$

where $R_{\max}$ is the contour length of the equivalent freely joined chain.

Eq. 2.30 renormalizes the monomers, and holds for all flexible linear polymers in the ideal state ($N \gg 1$), with all chemical-specific characteristics contained within the Kuhn monomer (i.e. Kuhn length). This makes the properties of flexible polymers independent of the local chemical structure, and thus universal.

2.3.3 Solvent effects

A polymer in solution is interacting with the solvent molecules. These interactions can significantly alter configuration of the polymer. There are three types of solvents, good-solvent, ideal (or θ-solvent) and bad-solvent. In good solvent conditions the interactions between the solvent molecules and the polymer monomers are attractive. This means that the polymer is soluble and the effective monomer-monomer interaction is repulsive. The chain conformation can be described as a self-avoiding walk, which is a random walk on a lattice that never visits the same site more than once. In an ideal solvent the net interaction between solvent molecules and polymer's monomers is zero. The polymer conformation resembles a random walk.[1] In the case of the bad-solvent conditions we have an attractive effective monomer-monomer interaction and the polymer collapses into a globular configuration for minimising the surface contact between the polymer and solvent.

[1] The monomers of a real chain in ideal-solvent do not overlap, but the statistics of the chain are the same with that of a random walk.

2.3.4 Scaling concepts of polymers

Flory Theory for a single chain

A simple and excellent scheme was devised by Flory for obtaining valuable insights on the conformations of linear chains. We briefly describe his method here, for more details see Refs. [14, 15].

Consider a polymer of N Kuhn monomers in good solvent conditions, which are uniformly distributed within volume R^d with no correlations between them. Note that the argument holds for an arbitrary dimensionality d. The probability of a second monomer being within the excluded volume v (in good solvent $v > 0$) of a given monomer is the product of the excluded volume v and the number density of the monomers in the pervaded volume of the chain N/R^d. The energetic cost of being excluded from this volume is kT per exclusion of $kTvN/R^d$ per monomer. For all N monomers in the chain, this energy is N times larger

$$F_{\text{int}} \approx kTv\frac{N^2}{R^d} \tag{2.31}$$

The Flory estimate of the entropic contribution to the free energy of a real chain is based on the fact that the entropic elasticity obeys the Hooke's law, and thus it is equal to the the energy required to stretch an ideal chain to end-to-end distance R:

$$F_{\text{ent}} \approx kTv\frac{R^2}{Nb^2} \tag{2.32}$$

The total free energy of a real chain in the Flory approximation is the sum of the energetic interaction and the entropic contributions:

$$F = F_{\text{int}} + F_{\text{ent}} \approx kT\left(v\frac{N^2}{R^d} + \frac{R^2}{Nb^2}\right) \tag{2.33}$$

The minimum free energy of the chain (obtained by setting $\partial F/\partial R = 0$) gives the optimum size of the real chain in the Flory theory, $R = R_{\text{F}}$:

$$\begin{aligned} \frac{\partial F}{\partial R} &= kT\left(-dv\frac{N^2}{R_{\text{F}}^{d+1}} + 2\frac{R_{\text{F}}}{Nb^2}\right) = 0 \\ R_{\text{F}}^{d+2} &\approx \frac{d}{2}vb^2N^3 \end{aligned} \tag{2.34}$$

The Flory theory leads to a universal power law dependence of polymer size R_{F}

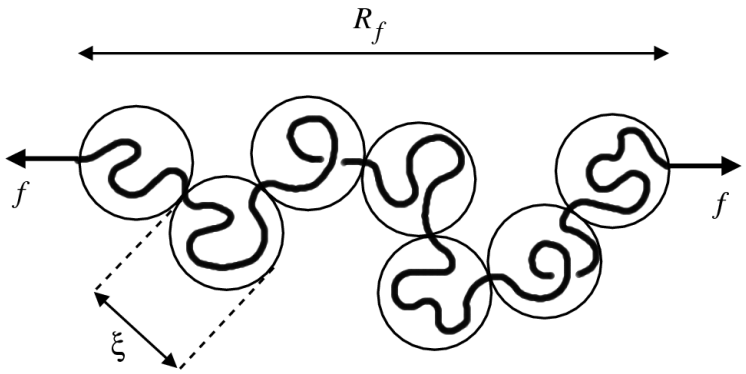

Figure 2.7: Stretching a linear chain by applying a force f at both ends of the chain. The characteristic length ξ represents the region in which within it the chain statists are unperturbed by the stretching.

on the number of monomers:

$$R_{\mathrm{F}} \sim N^{\nu} \quad \text{with} \quad \nu = \frac{3}{d+2} \tag{2.35}$$

where ν is the scaling exponent characterising the polymer conformation. It is interesting to note that ν is independented of v, thus being a universal exponent. One can work out with similar arguments the values of ν in different solvents, for more details are in Ref. [15]. The other values of ν for $d = 3$ are $1/2$ corresponding to an ideal chain (or θ-solvent conditions where the excluded volume $v = 0$) and $1/3$ describing the collapsed state of the chain when it enters into bad-solvent conditions.

The predictions of the Flory theory are in good agreement with both experiments and other more sophisticated theories. However, its success lies on cancellation of errors, because both the entropic and energetic terms in eq. 2.33 are overestimated. Nevertheless, Flory theory is useful because it is simple and provides a reasonable answer.

Stretching and blobs

To further understand scaling concepts, consider a chain of N Kuhn monomers of b size, under tension. The stretching is done by applying a force of magnitude f at both ends of the chain. In this problem the only characteristic lengths involved are (a) the Flory radius R_{F}, and (b) the length $\xi = kT/f$, which defines a tension blob of size ξ containing g monomers each, such that on length scales smaller than ξ the chain statistics are unperturbed, while on larger length scales the chain is a string of independent blobs, see Fig. 2.7. The number of monomers per blob, g, is related to ξ by the Flory law $\xi \approx bg^{\nu}$.

The end-to-end distance R_f is the product of the tension blob size ξ and the number of these blobs N/g

$$R_f \approx \xi \frac{N}{g} \approx Nb\left(\frac{fb}{kT}\right)^{1/\nu-1}. \tag{2.36}$$

This shows that a chain in good solvent ($\nu = 3/5$) has an elastic response which is nonlinear, $1/\nu - 1 = 2/3$, than in the case of an ideal chain ($\nu = 1/2$). In both types of solvents a stretched chain will have fewer possible configurations, but in good solvent conditions it has fewer possible configurations to lose. For this entropic reason it returns a smaller stretching force, but increases more rapidly with extension.

This concept of scaling, that is to divide a chain of Kuhn monomers into blobs that each contribute of order kT to the free energy, further simplifies the problem at hand.

2.4 Fractals and self-similarity

As demonstrated in section 2.3.1 polymers can adopt many different conformations that due to their size (the largest DNA molecules has 10^{10} bonds) can span through a wide range of length scales. But at the same time, they can be coarse-grained to high degree without losing the overall structural information. There is another feature in polymers that is related with the above characteristics, and that is most polymers are *self-similar*, or *finite random fractals*. In this section we will explore self-similar objects and some basic fractal properties by looking at polymers, and other examples.

2.4.1 Fractal dimension and Koch curve

Any polymer follows the Flory law, eq. 2.35 $R \sim N^{\nu}$, where ν takes the values 3/5, 1/2, and 1/3 in three dimensions for good, ideal and bad-solvent conditions, respectively. The values of ν characterise the conformations the chain takes, for example in a bad solvent ($\nu = 1/3$) the chain collapses into a globular structure. To explain this we briefly look to a mathematical example.

Consider a regular fractal, called the Koch-curve, see Fig. 2.8. To generate it one has to start with a section of a straight line and then divide it into three equal subsections. Then on the top of the middle subsection an equilateral triangle is drawn with its bottom side erased. Thus we end with four segments of equal length, with total length 4/3. Iterating the process infinitely many times results in a curve of infinite length, which is everywhere continuous but nowhere differentiable. Another

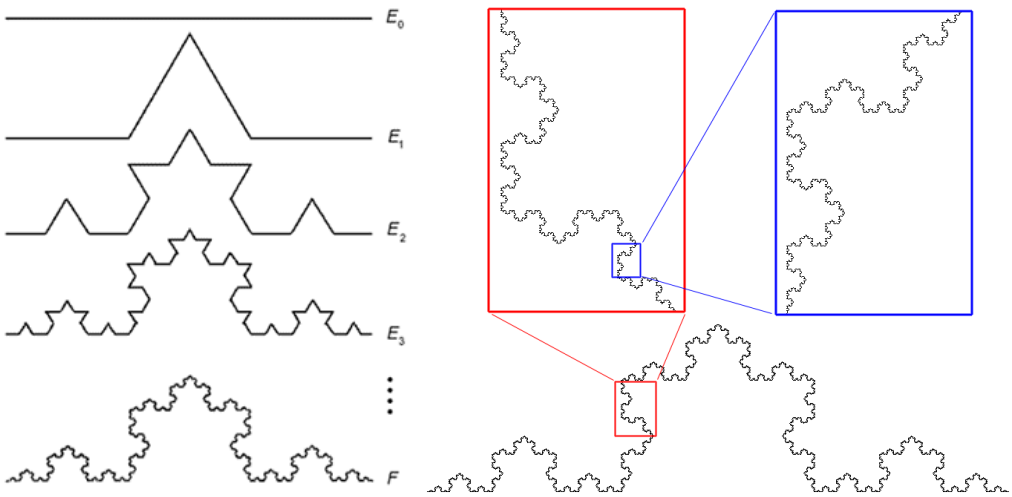

Figure 2.8: On the left an illustration shows the Koch curve after different number of iterations and on the right a display of the self-similar feature to a high order approximation to the Koch curve. (Both images were taken from Google search with related keywords)

striking feature is that if we magnify any section of the curve we will observe the same structure, see Fig. 2.8. This is an example of a fractal.

To understand this further we consider the following example. We have an infinite long straight rod of thickness (or diameter) H and it has uniform density. Now we draw a sphere of radius r around the rod, as seen in Fig. 2.9(a) and ask the question: *how the amount of mass, m, within the sphere changes as function of the radius of the sphere*. When the sphere is much bigger than the thickness of the wire ($r \gg H$) then the rod is effectively an one-dimensional object and so $m \sim r$. If however the sphere is smaller than the thickness (or diameter) of the rod ($r < H$) then the mass within the sphere will scale with the volume, thus $m \sim r^3$. The dependence of the mass m of the part of the wire inside the sphere of radius r is sketched in Fig. 2.9(a). Thus we can say that the rod is one-dimensional on length scales much larger than its thickness $r \gg H$ and three-dimensional on smaller scales $r < H$. Another important point to make is the relation between m and r in the form of $m \sim r^D$, where D is a *critical exponent* (also called *Hausdorff dimension*).

Now we apply similar arguments for the case of the Koch curve. We plot two circles of diameter $2r$ equal to the lengths of the lengths of two consecutive generations, see Fig. 2.9(b). The radius of the circles changes by a factor of 3 ($r_1 = 3r_2$), while the number of segments within the circles changes by a factor of 4 ($n_1 = 4n_2$). Similar with the previous example we assume that the number of segments within a cicle is

$$n \sim r^D \tag{2.37}$$

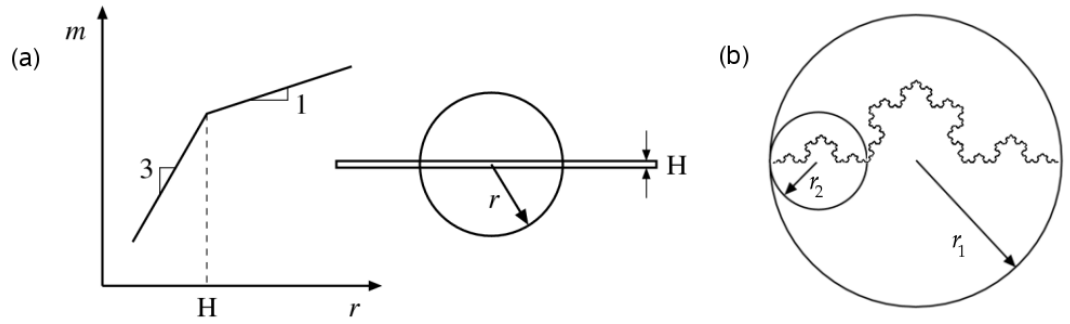

Figure 2.9: (a) The diagram shows how the amount of mass m of the part of the wire inside the sphere of radius r as function of r. Both axes have logarithmic scales. (b) Comparing the number of segments part of the Koch curve for two different circle radius, r_1 and r_2.

Now we can calculate the Hausdorff dimension in the following way:

$$n_1 = cr_1^D = c(3r_2)^D \tag{2.38}$$

$$n_1 = 4n_2 = 4cr_2^D \tag{2.39}$$

where c is a proportionality constant for eq. 2.37. Equating eqs. 2.38 and 2.39 will give

$$(3r_2)^D = 4r_2^D \tag{2.40}$$

which can be solved for the Hausdorff dimension of the Koch curve.

$$D = \frac{\ln 4}{\ln 3} \approx 1.26... \tag{2.41}$$

The value of D represents the dimensionality of the object; here it is close to one, which is somehow comforting because an infinity long curve is, in some sense, more than a one-dimensional object without being a two dimensional area.

Coming back to polymers the Flory value ν is related with the Hausdorff dimension in the following way

$$\nu \equiv \frac{1}{D} \tag{2.42}$$

The Flory value of ν for a two-dimensional polymer chain in good solvent conditions, is $\nu = 3/4$, and its Hausdorff dimension is $D = 1.333...$; this is quite close to the Hausdorff dimension for the Koch curve. However, polymers are *finite random* fractals, quite different from the Koch curve which is an example of a regular fractal. We emphasise two key differences. (a) A polymer is a self-similar object because if its smaller sections are magnified, they look similar to the whole chain. Unlike regular fractals the magnified sections do not look exactly like the whole chain, but

only on average. (b) Polymers can span many length scales but remain finite. Their self-similar features manifest themselves between the length scales of the monomer and that of the whole chain. This comes in contrast with regular fractals which are self-similar on *all* length scales.

2.4.2 Fractal universe

Mathematical fractals remain invariant to any change of scale. Polymers are not the only objects that manifest this property. That is because the underlying concept of fractals is *symmetry* – by symmetry we mean an *invariance* against change – and symmetry is everywhere in Nature. For example a widely noticed symmetry is the mirror symmetry, that is, invariance against flipping sides. Nature's most fundamental laws of physics, such as Newton's law of gravitation, have an exact mirror symmetry: there is no difference between left and right. Nevertheless the non-conservation of parity in radioactive decay – that is the violation of point symmetry in the *weak* interactions needs to be noted. Emmy Noether was the first to point out the connection between the symmetries in the fundamental laws of physics and the conservation of energy and momentum. In chapter 6 we observe that patterns of two-dimensional binary mixtures of dipolar colloids remain unchanged over wide ranges of density. The cause of this invariance in this example lies in the interactions between the colloids, which scales with a power law $\sim 1/r^3$. As we have seen in previous examples, power laws are related with fractals, due to their slow decaying tail spanning many (length) scales. In chapter 5 we discuss *scale-free networks* which relate and explain how physical systems that might look very different, such as protein networks, sexual contact networks and the Internet, can be governed by the same laws.

Chapter 3

Adsorption and self-assembly of linear polymers on surfaces

3.1 Introduction

Polymers near to, or adsorbed on, surfaces exhibit useful and interesting properties. Adsorbed polymers find application in colloid stabilisation, [16, 17] nanoscale surface patterning, [18] friction modification, [19, 20] DNA microarrays [21] and adhesion. [22] Polymers can be attached to appropriate surfaces either through chemisorption/grafting (i.e., anchoring by chemical bonds) or by physisorption (i.e., chain attachment by van der Waals interactions). For a weakly adsorbing surface the physisorption and resulting conformational relaxation of the chain is driven by the competition between the entropic repulsion due to the loss of conformational freedom and the drop in energy from binding monomers to the substrate. Earlier investigations have focused on thin-film polymer blends, [23, 24, 25] block copolymer micelles adsorbed on surfaces, [26, 27, 28] end-grafted polymers chemisorbed on surfaces, [29, 30, 31] and several other complex systems. The simple case of homopolymer chains physisorbed on a substrate has been studied with simulations of free [32, 33, 34, 35, 36, 37, 38] and tethered chains, [39, 40, 41] and through theoretical approaches; [14, 42, 43] experimental studies, however, are scarce.

In recent work by our groups, we studied the physisorption and self-assembly of star [2] and linear [1] polymers on smooth surfaces using using atomic-force microscopy (AFM). In a typical experiment, a polymer solution was prepared in good solvent at concentrations below the critical overlap volume fraction (ϕ^*), resulting in well-separated chains in solution and hence precluding any strong degree of structural ordering within the polymer component. Polymer (sub-)monolayers were formed by exposing a smooth surface (such as highly ordered pyrolytic graphite

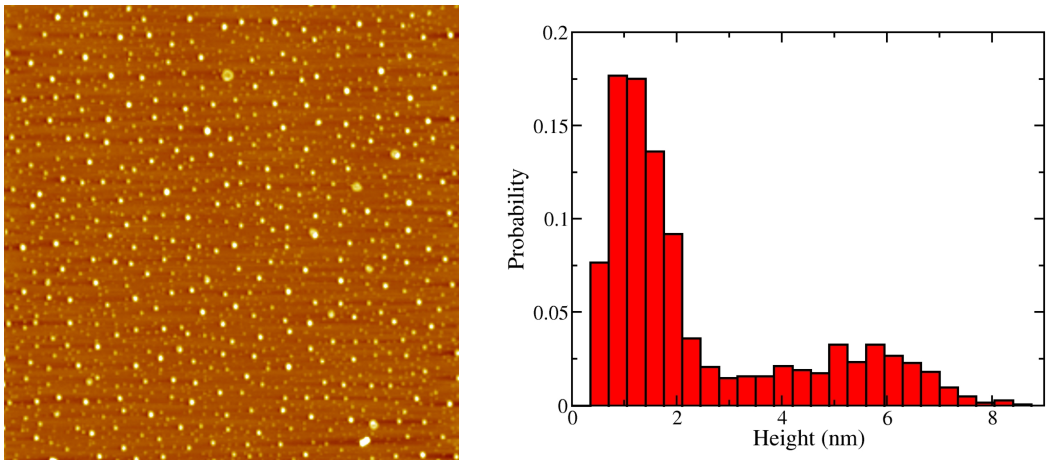

(a) (b)

Figure 3.1: (Colour online) (a) AFM image of linear polybutadiene (molecular mass 78.8 kDa) adsorbed on mica from toluene at a surface concentration of 7.75×10^{-2} mg m^{-2}. The image size is 6×6 μm^2. (b) Cluster-height distribution corresponding to the AFM image in (a).

or mica) to the polymer solution. The surface was then placed in a good solvent bath for several hours and extensively rinsed with good solvent to remove any non-adsorbed polymer. Finally, the samples were dried gently under a stream of nitrogen and subsequently imaged in air by AFM in tapping mode to investigate the resulting structures from this good solvent-to-bad solvent 'quench'. Depending on the polymer molecular weight, architecture, and concentration, very different surface structures can be obtained. Chapter 4 is focused on the case of star polymers, where it was found that the functionality (number of arms) and concentration of star polymers controls a crossover between 'polymer' and 'soft-colloid' regimes, being distinguished by characteristic cluster topologies, sizes, and surface coverages [2]. Using the same experimental procedure, we have now studied the adsorption of linear polybutadiene (PB) on to mica from toluene. A report of this investigation is in preparation [1], but for the purposes of the current work, we present one key experimental observation on which we will aim to gain insight using computer simulations. In Fig. 3.1(a) we present an AFM image of a freshly cleaved mica exposed for 30 minutes to a toluene PB solution (molecular weight 78.8 kg mol^{-1}) leading to a surface coverage of 7.75×10^{-2} mg m^{-2}. This image shows two distinct types of clusters. In Fig. 3.1(b) we show the corresponding bimodal cluster-height distribution, with most probable heights of 1 nm and 6 nm. In this chapter we aim to reproduce, and gain insight on, the development of bimodal cluster distributions using Langevin dynamics simulations of coarse-grained 'bead-spring' models of linear polymers.

In the experimental quenching procedure described above, the microscopic

structures of the polymer solutions in contact with surfaces prior to quenching must control the nature of polymer adsorption. Hence, the behaviour of polymers in good-solvent conditions and near a surface is of considerable interest. In the past, adsorption and depletion-layer effects have been the subjects of many experimental, theoretical, and computer-simulation studies. Of particular relevance to the current work is the seminal study by de Gennes focused on the monomer volume-fraction profile $\phi(z)$ as a function of the perpendicular distance from the surface z [44]. De Gennes considered a semidilute solution of chains in contact with a weakly attracting wall, with the wall-monomer interaction of a range comparable to the monomer size a. In the semidilute regime, the polymer volume fraction in solution $\phi_b > \phi^*$, meaning that there are overlapping chains. Near the wall, chains are physisorbed through a small number of monomers, leading to the formation of loops with characteristic dimension $D > a$. Well away from the wall, the characteristic length scale is the bulk correlation length $\xi_b \sim \phi_b^{-3/4}$ [14], which in the semidilute regime is comparable to the polymer radius of gyration R_G in bulk solution. Three regimes of z can be identified: the *proximal* regime $z \simeq a < D$ where $\phi(z)$ is dictated by the short-range interactions with the wall; the *central* regime $D < z < \xi_b$ in which "no other length enters in the problem" [44] meaning that if $\xi[\phi(z)] \simeq z$ and $\xi(z) \sim \phi(z)^{-3/4}$ then $\phi(z) \sim z^{-4/3}$; and the *distal* regime $z > \xi_b$ where $[\phi(z) - \phi_b]/\phi_b \sim \exp(-z/\xi_b)$. The structure in the central regime is 'self-similar' or 'scale-free', because there is no characteristic length scale (unlike in the proximal or distal regimes, which are characterised by a and ξ_b, respectively). The existence of a self-similar structure characterised by an exponent of $-\frac{4}{3}$ has been confirmed experimentally by neutron scattering [45] and by neutron reflectivity [46, 47, 48]. Results from Monte Carlo simulations of lattice polymer models are also consistent with this behaviour [49, 50, 51]. An incidental result of the current work is a demonstration that a coarse-grained, off-lattice polymer model can reproduce this self-similar structure, and with the correct exponent.

In this chapter we report a simulation study of adsorbed linear-polymer films. We use Langevin dynamics simulations of coarse-grained 'bead-spring' models to gain insight on the results from polymer adsorption experiments. The outline of the study is as follows. Firstly, we study the properties of isolated adsorbed polymers (vanishing surface coverage). This situation has been considered many times before (see, e.g., Ref. [38]), but for the purposes of comparison with the case of finite surface coverage, we reconsider specific single-molecule structural properties for the particular coarse-grained models being employed. Next, we deal with many polymers on a surface under good-solvent conditions, corresponding to the prelude to the bad-solvent quench in experiments. Of particular interest are simulation measure-

ments of $\phi(z)$ and the comparison with de Gennes' theoretical predictions. Finally, we simulate the good solvent-to-bad solvent quench, and its effects on the structure of the polymer film. Specifically, we identify under what conditions a bimodal cluster distribution (such as those seen in experiments – Fig. 3.1) should be expected. The chapter is organised as follows. Section 3.2 contains details of the coarse-grained polymer model, and the simulation methods. Results for isolated polymers and many polymers are presented in section 3.3. Section 3.4 concludes the chapter.

3.2 Simulation model and methods

Linear polymers are modelled as chains of N coarse-grained 'beads' connected by 'springs'. The physical motivation for such a model stems from the fact that correlations between monomers die off beyond a characteristic length, called the Kuhn length b. Hence, if a number of contiguous monomers are rendered by a single bead of dimension b, then the scaling properties of the chain on length scales larger than b will be left invariant [14, 52, 53]. Such bead-spring models of linear and star polymers were first introduced and employed in simulations by Grest and co-workers [54, 55, 56, 57]. In this work, N beads of equal mass m are connected to form a chain using a non-linear finitely extensible (FENE) potential between neighbouring beads, given by

$$V_{\mathrm{FENE}}(r) = -\frac{1}{2}kR_0^2 \ln\left(1 - \frac{r^2}{R_0^2}\right). \tag{3.1}$$

Here r is the bead-bead separation, R_0 is the maximum possible (bonded) bead-bead separation, and k is a spring constant. In this study we use parameters from earlier work [55], namely $R_0 = 3\sigma/2$ and $k = 30\varepsilon/\sigma^2$; ε and σ are the energy and range parameters, respectively, for the non-bonded interactions to be defined next.

The non-bonded interactions operate between all pairs of beads, and are derived from a composite potential devised by Steinhauser [58]. The potential is a combination of three terms. First we write the purely repulsive Weeks-Chandler-Andersen (WCA) potential [59], which is a Lennard-Jones potential cut and shifted at the position of the minimum, $r_{\mathrm{min}} = 2^{1/6}\sigma$:

$$V_{\mathrm{WCA}}(r) = \begin{cases} 4\varepsilon\left[\left(\frac{\sigma}{r}\right)^{12} - \left(\frac{\sigma}{r}\right)^{6}\right] + \varepsilon & r \le r_{\mathrm{min}} \\ 0 & r > r_{\mathrm{min}} \end{cases} \tag{3.2}$$

To represent the attractive interactions, the WCA potential is shifted back down in

the range $0 \le r \le r_{\min}$ by a square-well (SW) potential

$$V_{\mathrm{SW}}(r) \begin{cases} -\lambda\varepsilon & 0 < r \le r_{\min} \\ 0 & r > r_{\min} \end{cases} \tag{3.3}$$

where λ reflects the solvent quality (to be discussed below). To interpolate the potential smoothly between $-\lambda\varepsilon$ at $r = r_{\min}$ and 0 at a cut-off distance $r_{\mathrm{cut}} > r_{\min}$, we add the term

$$V_{\cos}(r) = \begin{cases} \frac{1}{2}\lambda\varepsilon\left[\cos(\alpha r^2 + \beta) - 1\right] & r_{\min} < r \le r_{\mathrm{cut}} \\ 0 & r > r_{\mathrm{cut}} \end{cases} \tag{3.4}$$

α and β satisfy the conditions $\alpha r_{\min}^2 + \beta = \pi$ and $\alpha r_{\mathrm{cut}}^2 + \beta = 2\pi$. The cosine form of the potential also means that $\mathrm{d}V_{\cos}/\mathrm{d}r = 0$ at $r = r_{\mathrm{cut}}$. Following earlier work [58], we choose $r_{\mathrm{cut}} = 3\sigma/2$, for which the appropriate parameters are

$$\alpha = \frac{4\pi}{9 - 4\sqrt[3]{2}} = 3.173\,072\,868 \tag{3.5}$$

$$\beta = 2\pi - \frac{9}{4}\alpha = -0.856\,228\,645. \tag{3.6}$$

The final, non-bonded potential is $V(r) = V_{\mathrm{WCA}} + V_{\mathrm{SW}}(r) + V_{\cos}(r)$, and is sketched in Fig. 3.2. The parameter λ controls the depth of the potential well at $r = r_{\min}$, and provides a convenient measure of the solvent quality. In a good solvent, the effective bead-bead interactions are purely repulsive; this corresponds to $\lambda = 0$. In a bad solvent, the bead-bead interactions are attractive, and this behaviour can be modelled with $\lambda = 1$; this corresponds to an attractive well of depth ϵ which sets the molecular energy. θ-solvent conditions – under which the chain statistics are very similar to those for an ideal (non-interacting) chain – are reproduced by $\lambda = 0.646$ [58].

For simulations involving a surface, an additional effective bead-surface potential is used, [57] based on integrating the Lennard-Jones interactions arising from a homogeneous distribution of sites within the surface. The potential is

$$V_s(z) = \frac{2\pi\varepsilon_s}{3}\left[\frac{2}{15}\left(\frac{\sigma}{z}\right)^9 - \left(\frac{\sigma}{z}\right)^3\right] \tag{3.7}$$

where z is the perpendicular distance of the bead from the surface, and ε_s controls the strength of the bead-surface attraction. In our simulations we define ε_s in terms of basic energy parameter ε by defining the dimensionless ratio $\varepsilon_s^* = \varepsilon_s/\varepsilon$. In practice, we concentrate on the values in the range $0.4 \le \varepsilon_s^* \le 1.0$.

For simulating the bead-spring polymer chains, we used Langevin dynamics

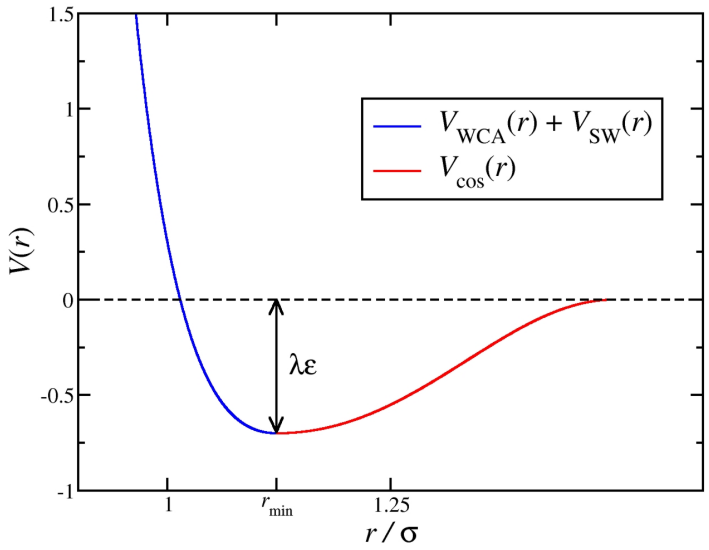

Figure 3.2: (Color online) The non-bonded, bead-bead interaction potential $V(r)$ with $\lambda = 0.7$, showing the contributions from $V_{\mathrm{WCA}}(r) + V_{\mathrm{SW}}(r)$ (blue) and $V_{\cos}(r)$ (red).

in which the system is coupled to a heat bath, corresponding physically to solvent. In addition to the conservative forces arising from the interaction potentials described above, each bead will feel random and frictional forces mimicking the solvent surrounding the bead. Thus the equations of motion for bead i are given by

$$m\frac{\mathrm{d}^2\boldsymbol{r}_i}{\mathrm{d}t^2} = -\nabla_{\boldsymbol{r}_i} V - m\Gamma\frac{\mathrm{d}\boldsymbol{r}_i}{\mathrm{d}t} + \boldsymbol{W}_i(t) \tag{3.8}$$

where Γ is the friction coefficient, $\boldsymbol{W}_i(t)$ describes the Brownian forces of the solvent acting on the bead, and $V = \sum_{i<j} V_{ij}$ is the total interaction potential. $\boldsymbol{W}_i(t)$ is represented by Gaussian white noise satisfying the fluctuation-dissipation theorem [9]

$$\langle \boldsymbol{W}_i(t) \cdot \boldsymbol{W}_j(t') \rangle = 6k_B T m\Gamma\delta_{ij}\delta(t-t') \tag{3.9}$$

where k_B is Boltzmann's constant, and T is the temperature. The Einstein relation leads to a diffusion constant for an isolated bead of $D_0 = k_B T/m\Gamma$. Further details are given in Ref. [54] and in chapter 2.

Simulations were performed in an $L \times L \times H$ cuboidal box with periodic boundary conditions in all three directions and the minimum-image convention applied. The box dimension in the z direction was set to a large, but finite, value of $H = 200\sigma$, and the surface was represented by a structureless, $L \times L \times l$ solid slab with a thickness l no less than the maximum range of interaction between beads. To control the surface bead density, L took on values of 80σ through to 180σ, which were always large

enough for polymers in their natural conformations to avoid interacting with their own periodic images. The simulation conditions mean that the polymers are at finite density within the simulation cell, and so there is an equilibrium state where the polymers are adsorbed. In principle, the polymers could adsorb on either face of the slab, but they cannot interact with each other because l is larger than the interaction range, and H is much larger than typical polymer dimensions (as measured by the radius of gyration, R_G); hence, the two surfaces are essentially isolated from one another. In practice, initial configurations were prepared by placing the polymers on one face of the slab, and all subsequent measurements were made for that one surface. Simulated properties are reported here in reduced units defined in terms of m, ε, and σ. The equations of motion were integrated using the velocity-Verlet algorithm with a time-step $\delta t = 0.007\tau$, where $\tau = \sqrt{m\sigma^2/\varepsilon}$ is the basic unit of time. In all cases, the reduced temperature $k_B T/\varepsilon = 1$, and the reduced friction coefficient $\Gamma\tau = 1$.

3.3 Results & discussion

We have studied three different situations using Langevin dynamics simulations: (i) the behaviour of isolated polymers on surfaces with various solvent qualities (with $0 \leq \lambda \leq 1$); (ii) the behaviour of many polymers on surfaces in good-solvent conditions (with $\lambda = 0$), corresponding to the experimental situation before the good solvent-to-bad solvent quench; and (iii) many polymers in bad-solvent conditions (with $\lambda = 1$) corresponding to the post-quench situation probed in AFM experiments. We have studied three different chain lengths ($N = 50$, 100, and 200 beads), a range of different surface-energy parameters $\varepsilon_s^* = \varepsilon_s/\varepsilon$, and in the many-polymer cases, a variety of surface coverages (to be defined in section 3.3.2). The number of beads in each of the longest chains is of the same order of magnitude as the number of Kuhn monomers in the smallest chains studied in experiments. Such coarse-grained, bead spring models are known to reproduce faithfully the semi-quantitative properties of polymers, and so despite the small lengths of our chains, we anticipate that the various trends seen in our results will be of relevance to experiments on ultra-thin polymer films after a sudden change in the solvent quality. Our choices for ε_s^* are based achieving a suitable degree of surface adsorption. We have not attempted the difficult problem of determining this effective interaction parameter from first principles; this would involve using atomistic representations of the surface, polymer and solvent in order to determine the direct and solvent-mediated forces acting between the polymer and surface.

3.3.1 Isolated polymer

The average conformation of a polymer in dilute solution is well understood, and has an isotropic globular shape defined by a radius of gyration R_G, which scales with the number of monomer units N like $R_G \sim N^{\nu}$ where ν is a characteristic exponent equal to $\frac{1}{3}$ in a bad solvent, $\frac{1}{2}$ in a θ-solvent, and $\frac{3}{5}$ in a good solvent [14]. In the proximity of a surface, the number of available polymer conformations is reduced, leading to a decrease in entropy. Adsorption occurs when the surface-energy parameter ε_s exceeds a certain critical value, ε_s^c, signaling that the energetic contribution to the free-energy from polymer-surface interactions becomes significant [14, 60]. The accompanying change in polymer conformation can be interpreted as the order parameter a type of second-order phase transition at $\varepsilon_s^* = \varepsilon_s^c$ [14, 60]. It is useful to define the dimensionless variable κ

$$\kappa = (\varepsilon_s - \varepsilon_s^c)/\varepsilon_s^c \tag{3.10}$$

which measures the critical distance from the critical point. We also define the scaling variable y,

$$y = \kappa N^{\phi} \tag{3.11}$$

where ϕ is a crossover exponent; this variable appears in the scaling analysis of polymer adsorption. [44, 42] Through scaling theory, one can identify four regimes of adsorption depending on the values of y and κ. (a) For a repulsive wall, $y < 0$, the chain trivially remains away from the surface. (b) Near the critical point, $y \simeq 0$, the chain is equally likely to be found at the surface as it is in the solution. (c) When $y \gg 1$ with N large and κ small, adsorption is nonetheless favored because the sum of the interactions of the individual beads with the surface outweighs the entropic penalty penalty of the chain being near the wall. This situation is called weak coupling limit. [44] (d) For $\kappa > 1$ the monomers are strongly attracted to the surface and the chain lies flat. This is called the strong coupling limit. [44] Cases (a)-(c) have been studied extensively in simulations of the particular situation where each chain is tethered to the surface by one end; [40, 41] case (d) has been studied in simulations of free chains. [36, 37, 38] Earlier simulations using the same type of bead-surface potential (3.7) suggest that, in reduced units, the critical surface-energy parameter $\varepsilon_s^c/\varepsilon \sim 0.1$. [41] The values of ε_s^* used in the current simulations (reported below) correspond to the strong-coupling regime.

All isolated-polymer simulations began by placing a linear chain in good-solvent conditions ($\lambda = 0$) close enough to the surface for adsorption to occur. Once the chain had adsorbed, the solvent quality was adjusted by changing λ to the desired value.

The molecule was equilibrated for around $10^6\delta t$, and then properties were measured over a production run of $5\times10^6\delta t$. Figures 3.3(a) and (b) shows the probability density $p(z)$ of finding beads at a perpendicular distance z from the surface, from simulations of isolated polymers consisting of $N = 100$ beads, with various values of ε_s^* and λ. (The density profiles are reported in this form – normalized so that $\int_0^\infty p(z)\mathrm{d}z = 1$ – to aid comparison with later results for many polymers at finite densities.) In all cases there is either a local minimum or a point of inflection in $p(z)$ at $z \simeq 1.2\sigma$, and the position of these features was taken as a distance-based criterion for assessing whether a particular bead is 'bound' to the surface or not. Note that from equation (3.7) the minimum bead-surface potential energy is located at $z/\sigma = \sqrt[6]{2/5} \simeq 0.86$; this distance corresponds to the positions of the primary peaks in $p(z)$.

In Fig. 3.4 we show the average bound fraction $\langle\Phi_a\rangle$ and the average maximum height $\langle h\rangle$ as functions of λ for different chain lengths and surface-energy parameters ε_s^*. With $N = 50$, no apparently stable adsorption occurs for $\varepsilon_s^* < 0.6$, while for the longer chains with $N = 100$ and 200, adsorption occurs when $\varepsilon_s^* \geq 0.4$. That is because for $\varepsilon_s^* = 0.4$ we are close to weak coupling regime, meaning that the sum of individual bead's enthalpic contributions with the surface for shorter chains is not enough keep them on the surface. The bound fraction $\langle\Phi_a\rangle$ is the fraction of beads within interaction range of the surface defined using the distance-based criterion $z \leq 1.2\sigma$. For all ε_s^*, $\langle\Phi_a\rangle$ remain insensitive to N. This is in agreement with theory and simulations, since for $\kappa > 1$ the bound fraction scales $\Phi_a \sim N^0$ [61]. It also remains insensitive to solvent quality. There is though only a weak monotonic decrease with increasing λ; this is due to the polymers bunching up to optimize the attractive bead-bead interactions, at the cost of bead-surface contacts. Unsurprisingly, for a given λ, increasing ε_s^* leads to a greater bound fraction.

In general, the average maximum height $\langle h\rangle$ for all systems with $\varepsilon_s^* \geq 0.6$ shows a very weak dependence on λ, there being only a slight hint of an increase as the bad-solvent conditions ($\lambda = 1$) are approached; this is due to the 'bunching up' of the beads, to take advantage of their mutual attractive interactions. But on the whole, the strong bead-surface interactions keep the polymers quite flat on the surface, with small, short-lived 'loops' and 'tails' appearing as beads lift off the surface as a result of thermal fluctuations.

Different behavior is observed in those systems with $N = 100$ and 200 beads, and $\varepsilon_s^* = 0.4$, in which $\langle h\rangle$ clearly decreases with increasing λ. This, again, is due to the 'bunching up' of the polymer chain, much like an accordion being compressed. The difference here, though, is that with such a weak bead-surface interaction parameter, the polymers possess only a small number of contacts with the surface, leading to

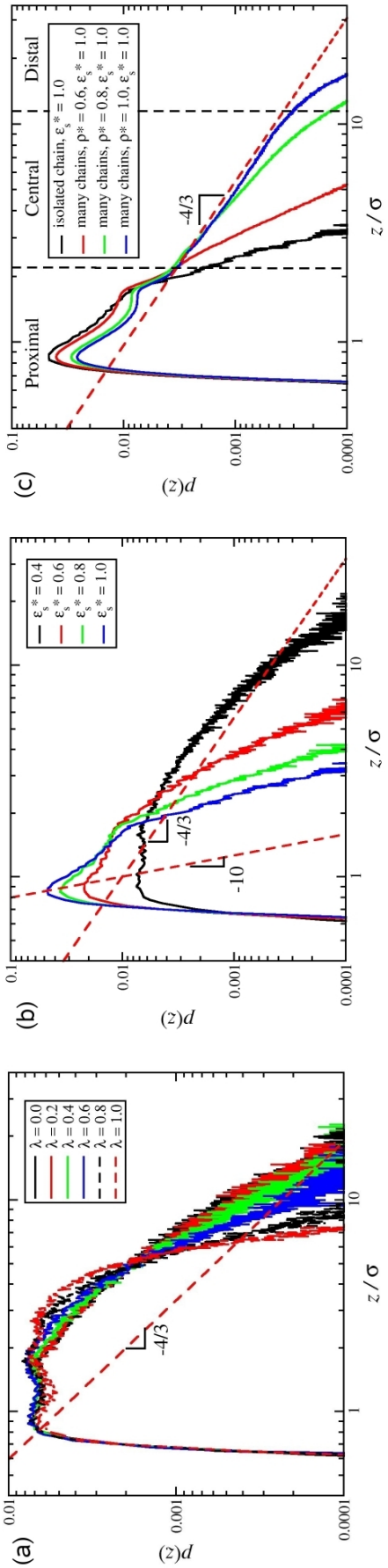

Figure 3.3: (Color online) The probability distribution $p(z)$ of finding a bead at a perpendicular distance z from the surface. All results are for chains with $N = 100$ beads. (a) Isolated chain with $\varepsilon_s^* = 0.4$ and $0 \leq \lambda \leq 1$. (b) Isolated chain with $\lambda = 0$ (good solvent) and $0.4 \leq \varepsilon_s^* \leq 1.0$. (c) Isolated chain compared to many chains (with densities $\rho^* = 0.6$, 0.8, and 1.0), all with $\lambda = 0$ (good solvent) and $\varepsilon_s^* = 1.0$.

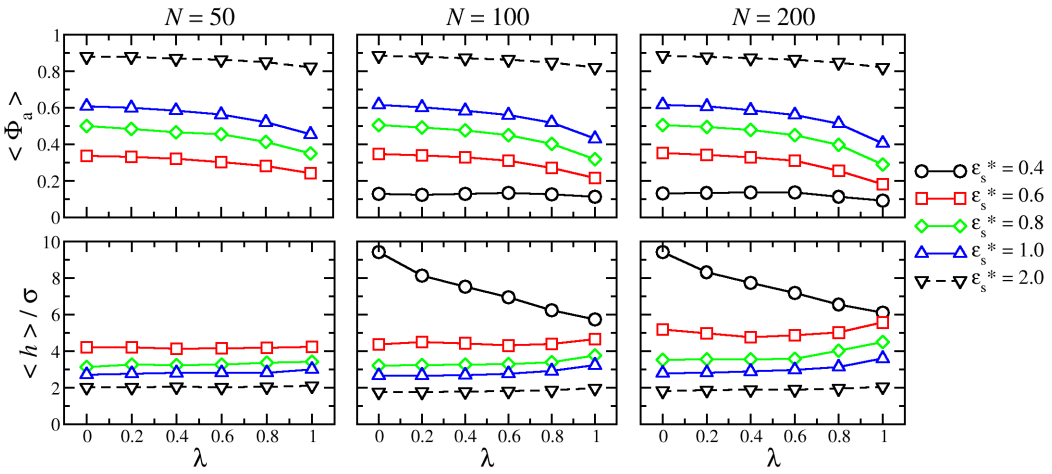

Figure 3.4: (Color online) The bound fraction $\langle \Phi_a \rangle$ (top) and the average maximum height $\langle h \rangle$ (bottom) against solvent quality λ for isolated linear chains with, from left to right, $N = 50$, 100, and 200 beads, and with different surface-interaction parameters ε_s^*.

the formation of large, long-lived 'loops' and 'tails' oriented perpendicular to the surface. When λ is increased, the loops and tails contract, leading to a reduction in the height of the polymer; but with a weak bead-surface interaction, this process occurs without the loops flattening out and forming new contacts with the surface.

3.3.2 Many polymers – good solvent

Polymers in good solvent experience purely repulsive mutual interactions. Appropriate simulations with $\lambda = 0$ were initiated by preparing configurations with many 'curled up' polymers on a surface, and equilibrating for around $10^6 \delta t$. For chains of $N = 50$, 100, and 200 beads, we initially placed 200, 100, and 50 chains on the surface, respectively, leading to the same total number of beads in each case. Following equilibration, we performed a production run of $2.5 \times 10^6 \delta t$. The adsorption is measured by the equilibrium surface bead density, defined in terms of the number of beads N_{ads} belonging to those chains with at least one bead-surface contact, defined using the distance-based criterion $z \leq 1.2\sigma$. Note that N_{ads} is, in general, greater than the number of beads actually bound to the surface. The reduced surface bead density is $\rho^* = N_{\text{ads}}\sigma^2/L^2$. By placing a fixed number of chains on surfaces of various sizes, we simulated surface densities, up to that corresponding to the critical overlap concetration. In other words, approached the semidilute regime within the adsorbed film. During equilibration runs near the critical overlap concetration, some of the polymers were seen to desorb as the polymer film approached the steady state.

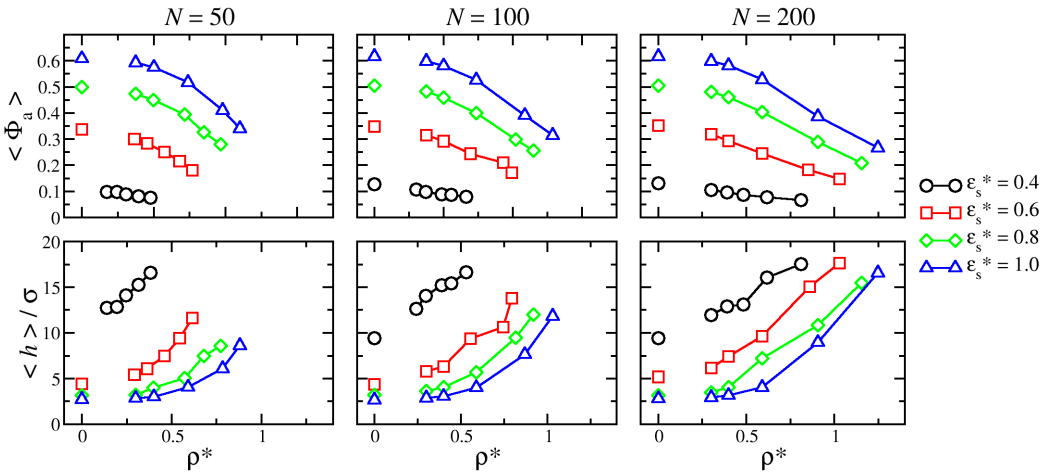

Figure 3.5: (Color online) The bound fraction $\langle\Phi_a\rangle$ (top) and the average maximum height $\langle h\rangle$ (bottom) against surface bead density ρ^* for many linear chains with, from left to right, $N = 50$, 100, and 200 beads, in good solvent ($\lambda = 0$) and with different surface-interaction parameters ε_s^*. Wherever possible, the corresponding isolated-polymer results are shown at $\rho^* = 0$.

We first consider the average bound fraction $\langle\Phi_a\rangle$ and maximum height $\langle h\rangle$, presented in Fig. 3.5. Results are shown as functions of the surface bead density ρ^* for chains of $N = 50$, 100, and 200 beads with bead-surface interaction parameters $0.4 \le \varepsilon_s^* \le 1.0$. For comparison, points for isolated chains are shown at $\rho^* = 0$, the effective density in this case. In all cases, $\langle\Phi_a\rangle$ decreases with increasing ρ^*. This may be explained by the entropic penalty associated with a reduced number of molecular conformations due to crowding; this effect becomes more pronounced as the surface density is increased. With purely repulsive bead-bead interactions, there is no additional energetic gain upon adsorption (above the bead-surface interaction) to offset the growing entropic penalty. Hence, it is more favorable for the some beads to lift off the surface to ease crowding. Some additional observations are that for a given N and ρ^*, $\langle\Phi_a\rangle$ increases with increasing ε_s^*; and that for a given ρ^* and ε_s^*, $\langle\Phi_a\rangle$ is essentially independent of N. We note that $\langle\Phi_a\rangle$ has been examined in experiments on linear-polymer films [62], but these were conducted with chemisorbed molecules, as opposed to the physisorbed molecules considered in this work. Chemisorption reduces sorbate mobility, and hence reduces the opportunity for reorganization. In addition, molecules can be irreversibly chemisorbed through fewer surface contacts than those required for physisorption. Both of these effects lead to relatively low bound fractions, as compared to the results reported here.

Examples of the structural differences between weak and strong surface parameter cases are illustrated in the simulation snapshots shown in Fig. 3.6. These are

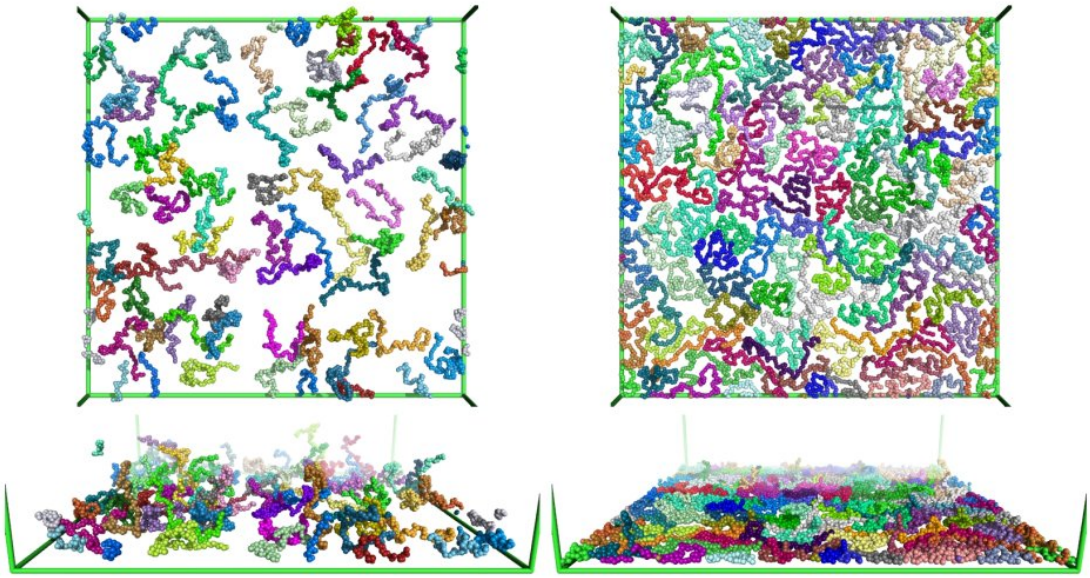

Figure 3.6: (Color online) Top views (top) and side views (bottom) from simulations of chains with $N = 100$ beads in good solvent ($\lambda = 0$). The surface dimensions are $130\sigma \times 130\sigma$. (Left) $\varepsilon_s^* = 0.4$, $\rho^* = 0.39$, $N_{\text{ads}} = 6600$. (Right) $\varepsilon_s^* = 1.0$, $\rho^* = 0.59$, $N_{\text{ads}} = 10000$. Figures were prepared using Pymol (http://pymol.sourceforge.net/).

from simulations of chains with $N = 100$ beads. With $\varepsilon_s^* = 0.4$ and at $\rho^* = 0.39$, the polymers form 'loops' and 'tails', orientated away from the surface; with $\varepsilon_s^* = 1.0$ and at $\rho^* = 0.59$, the polymers are flat on the surface, despite the high density.

Variations in the average maximum height $\langle h \rangle$, shown in Fig. 3.5, correlate with those in $\langle \Phi_a \rangle$. As the bound fraction decreases, the film height increases, reflecting the build-up of the polymer film. Scaling theory predicts that the height $\langle h \rangle$ scales like $\varepsilon_s^{\nu/(\nu-1)}$ where ν is the characteristic exponent [14, 15, 63]. For polymers in good solvent, $\nu = \frac{3}{5}$ and so $\langle h \rangle \sim \varepsilon_s^{-3/2}$. This applies to isolated polymers, and to many polymers when the surface concentration is much greater than the bulk concentration. Since in all cases we have an effective bulk density of zero, the scaling law should be observed. For each system showing significant adsorption under good-solvent conditions, we fitted $\langle h \rangle$ to the function

$$\langle h \rangle = \frac{h_0}{(\varepsilon_s^*)^{3/2}} \tag{3.12}$$

and plotted the quantities $\langle h \rangle / h_0$ on a single graph, as shown in Fig. 3.7. The results should collapse on to the curve $(\varepsilon_s^*)^{-3/2}$; they are indeed broadly consistent with the predicted scaling. Note that the critical surface-energy parameter is expected to be unimportant in this analysis, because we are working in the strong-coupling

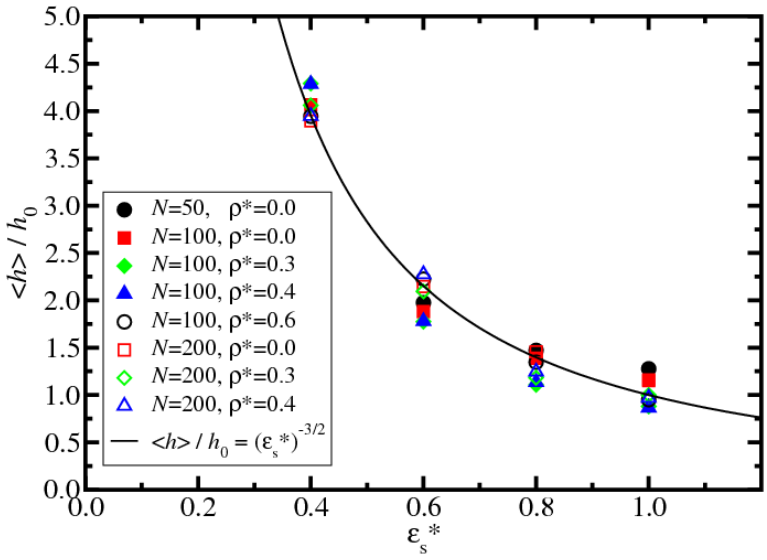

Figure 3.7: (Color online) Scaling plot of the maximum height $\langle h \rangle$ against the surface interaction parameter ε_s^* for polymers in good-solvent conditions ($\lambda = 0$). A reduced density of $\rho^* = 0$ corresponds to isolated polymers. The theoretical prediction [14, 15, 63] is that $\langle h \rangle \sim \varepsilon_s^{\nu/(\nu-1)}$, which for good-solvent conditions ($\nu = \frac{3}{5}$) gives $\langle h \rangle \sim \varepsilon_s^{-3/2}$. h_0 is the constant of proportionality from Eq. (3.12).

regime. From the fit shown in Fig. 3.7, it is clear that the critical value of ε_s^* would be small as compared to those used in the simulations. Indeed, attempts to fit critical parameters led to values of no more than 0.1, in reduced units, but with relative statistical uncertainties approaching 100%.

The effects of the surface-interaction parameter on the conformations of polymers in good-solvent conditions can be characterized in terms of the radius of gyration R_G defined by

$$R_G^2 = \left\langle \frac{1}{N^2} \sum_{i=1}^{N} \sum_{j>i}^{N} |\boldsymbol{r}_i - \boldsymbol{r}_j|^2 \right\rangle. \tag{3.13}$$

We note that R_G^2 can be decomposed in to components perpendicular and parallel to a surface, but the average value defined above is sufficient for the current purposes. Figure 3.8 shows the ratio $\gamma = R_G^2(\text{many})/R_G^2(\text{isolated})$, where $R_G^2(\text{many})$ is for many polymers made up of $N = 200$ beads in good-solvent conditions and at finite density, and $R_G^2(\text{isolated})$ is the corresponding value for an isolated polymer on a surface (and therefore at an effective density of $\rho^* = 0$). Results are shown for systems with various surface-interaction parameters. For a given ε_s^*, increasing the density causes a decrease in γ, reflecting a crowding effect due to neighboring polymers. For a given ρ^*, increasing ε_s^* causes a flattening of the polymers, and hence an overall reduction in the average dimensions.

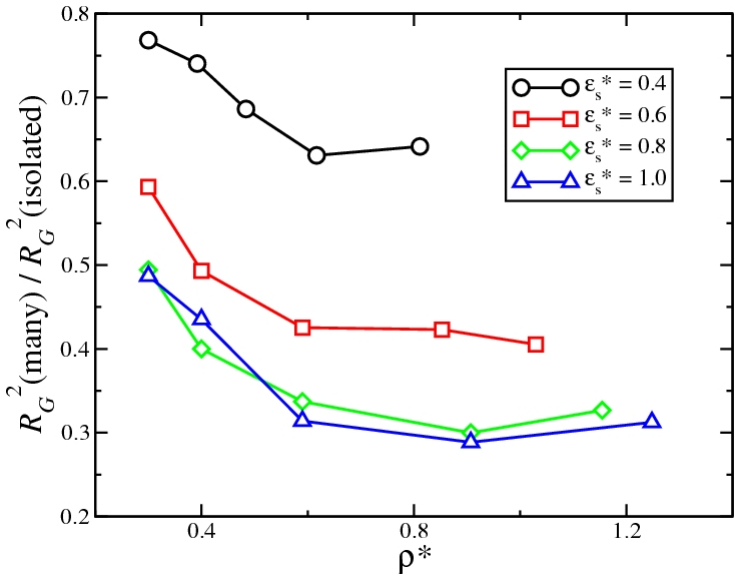

Figure 3.8: (Color online) R_G^2 for many polymers, divided by R_G^2 for an isolated polymer, against surface bead density ρ^*, for polymers with $N = 200$ beads in good-solvent conditions and with various surface-interaction parameters ε_s^*.

The probability density $p(z)$ for the many-polymer case is shown in Fig. 3.3(c). Specifically, we show results for chains consisting of $N = 100$ beads in pure solvent, with $\lambda = 0$, a fixed surface-interaction parameter $\varepsilon_s^* = 1.0$, and surface bead densities ranging from $\rho^* = 0$ (isolated chain) to $\rho^* = 1.0$. The proximal regime, identified by de Gennes, [44] is dominated by the bead-surface interactions, and in this case covers the range $0 \le z/\sigma \le 2$; the two peaks can be interpreted as arising from two ordered layers on the surface. For an isolated chain, $p(z)$ dies off very rapidly beyond $z \simeq 2\sigma$. At finite densities, $p(z)$ dies off rapidly at large distances, roughly corresponding to distal regime. Under the same conditions, there is an intermediate, central regime in which $p(z)$ should vary like $z^{-4/3}$ in good-solvent conditions [14]; our simulation results appear to be consistent with this scaling law. For the system with $\rho^* = 1.0$, the central regime covers the range $2 \le z/\sigma \le 10$; approximate ranges of the proximal, central and distal regimes for this system are indicated in Fig. 3.3(c). In general, the theoretical scaling predictions should apply to long chains and to adsorption from semidilute solutions. The experimental [1] and simulation conditions correspond more closely to an adsorbed film with a pure sovent; in addition, the simulated chains are relatively short. Our results approach the expected $z^{-4/3}$ scaling as the density is increased due to the conditions *near the surface* are beginning to resemble those in a film formed by adsorption from semidilute solutions. Note that this is consistence even for strong adsoprtion, because the polymers extend to distances of the same order the Flory radius, $R_F \sim N^\nu$, with large loops [42]. We emphasize that this study

was not focused on observing the predicted scaling, but it is comforting that our simulation results are at least consistent with the theoretical predictions [44, 42, 43]; coarse-grained, off-lattice models of polymers in good solvent appear to form de Gennes' 'self-similar carpet' [43].

3.3.3 Many polymers – bad solvent

The final step in the experimental polymer-adsorption procedure being considered here, is the quench from good-solvent to bad-solvent conditions, corresponding to rinsing with solvent and then drying in nitrogen / air. In our simulations, we mimic this step by starting simulations from well equilibrated configurations with $\lambda = 0$ (good solvent) and then instantaneously switching to $\lambda = 1$ (bad solvent). We then re-equilibrate the system for $2 \times 10^6 \delta t$, during which time the system was seen to reach an apparent steady state. In our experiments, the surface structures are apparently stable for periods of at least ten days. In our simulations no restrictions exist in the lateral directions, e.g. surface roughness, thus allowing the polymers slowing to diffuse on the surface. In earlier simulations of polymers films on surfaces, apparently metastable structures have been observed for periods of time that might extend towards experimental timescales [64]. Simulations therefore provide valuable insights on the experimental images. Nevertheless, it is easy to imagine that the true equilibrium state –if accessible– would correspond to a single, large (hemisperical) polymer droplet [32, 33, 34]; so the observed behavior in our simulations might best described as metastable. This is because the diffusion rate of an adsorbed polymer chain in bad solvent is not only lower than in good solvent, bad also inversely proportional to the number of beads [35]. Thus, within the simulation timescale, clusters may not diffuse sufficiently far in order to form a putative, single-droplet equilibrium structure. In any case, the structures we observe are apparently static on the timescales accessed in the simulations.

Figure 3.9 shows examples of equilibrated simulation configurations before ($\lambda = 0$) and after ($\lambda = 1$) the quench, for systems of polymers each made up from $N = 200$ beads, with surface-interaction parameters $\varepsilon_s^* = 0.4$, and at various densities. In good-solvent conditions, the polymers are in extended conformations, but in bad-solvent conditions they collapse to form globular clusters to optimize the attractive bead-bead interactions. At high density ($\rho^* = 0.81$) the quench induces extensive clustering, resulting in a small number of large clusters. At intermediate density ($\rho^* = 0.49$), a mixture of single chains and large clusters is in evidence, with the single chains in the minority. At low density ($\rho^* = 0.30$) the single chains are more numerous.

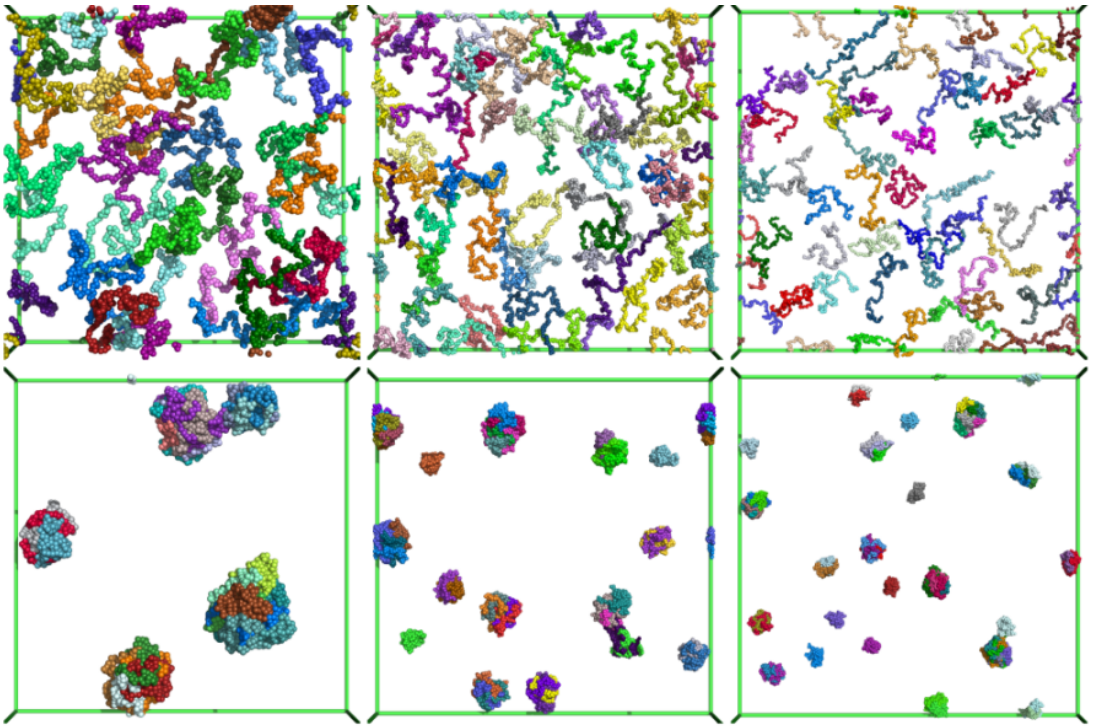

Figure 3.9: (Color online) Top views from simulations of chains with $N = 200$ beads in good-solvent conditions ($\lambda = 0$, top) and bad-solvent conditions ($\lambda = 1$, bottom), and with surface-interaction parameter $\varepsilon_s^* = 0.4$. (Left) $\rho^* = 0.81$, $L = 80\sigma$, $N_{\mathrm{ads}} = 5200$. (Center) $\rho^* = 0.49$, $L = 130\sigma$, $N_{\mathrm{ads}} = 8200$. (Right) $\rho^* = 0.30$, $L = 180\sigma$, $N_{\mathrm{ads}} = 9720$. Figures were prepared using Pymol (http://pymol.sourceforge.net/).

In Fig. 3.10 we show cluster-size histograms for systems of polymers ($N = 200$ beads per polymer) in bad-solvent conditions, with fixed surface bead density $\rho^* = 0.30$, and with various surface-interaction parameters ε_s^*. Two polymers were considered clustered if any two beads on different polymers were within a distance of 1.5σ. Histograms were accumulated from sets of five independent good solvent-to-bad solvent simulations. With small surface-interaction parameters ($\varepsilon_s^* = 0.4$ and 0.6) the distribution shows a monotonic decrease from the peak corresponding to single chains; with larger parameters ($\varepsilon_s^* = 0.8$ and 1.0), the distribution is bimodal, with a clear delineation between one-chain or two-chain species, and larger clusters. The bimodal distribution is to be compared qualitatively to that found in AFM experiments, Fig. 3.1(b). A direct, quantitative comparison is not feasible because we have not considered a specific, coarse-grained molecular model tailored to describe 78.8 kDa linear PB adsorbed on mica. Another factor that might influence the pattern formation, and that has not been considered in the simulations, is polydispersity in the lengths of the chains. Nonetheless, we suggest that the general picture, to be sketched out below, will apply to the real, experimental situation.

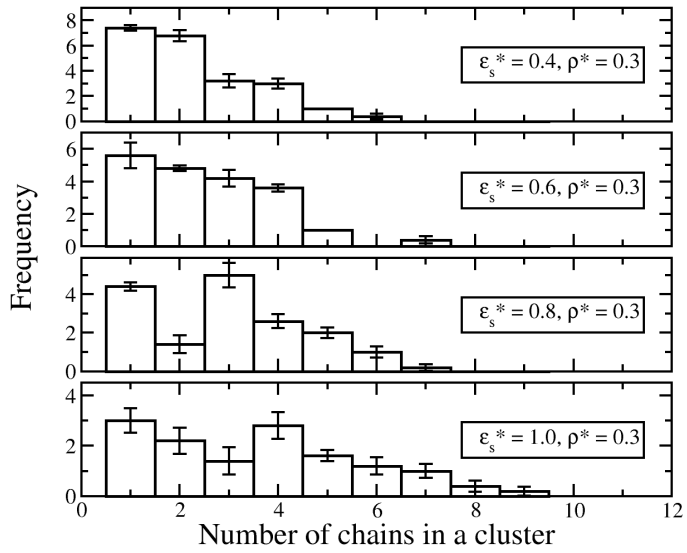

Figure 3.10: Cluster-size histograms from simulations of polymers with $N = 200$ beads in bad-solvent conditions ($\lambda = 1$), at a density $\rho^* = 0.30$, and with various surface-interaction parameters. Each histogram is an average of five independent simulations of the good solvent-to-bad solvent quenching process. In each case, the total number of adsorbed beads (as defined in section 3.3.2) is $N_{\text{ads}} = 10000$.

Clearly, the nature of the cluster-size distribution depends on both ρ^* and ε_s^*. From simulations of 200-bead polymers at different densities and with different surface-interaction parameters, we constructed a 'phase diagram' indicating whether the quenched configurations in bad-solvent conditions showed monotonically decreasing cluster-size distributions, bimodal distributions, or distributions showing single peaks; it is shown in Fig. 3.11. In general, low ρ^* / low ε_s^* favors a monotonically decreasing cluster distribution. Increasing ε_s^* flattens out the polymers on the surface, while increasing ρ^* slightly leads to more overlaps with neighboring chains; either change leads to more pronounced clustering and a bimodal cluster distribution. At high values of ρ^* and ε_s^*, the clustering is extensive and the cluster-size distribution is strongly peaked (typically at around five chains per cluster).

From these results, we can picture the polymer behavior during the good solvent-to-bad solvent quench as follows. At low density and with a low surface-interaction parameter, the polymers are largely isolated from one another and the probability of forming bead-bead contacts is low because of the large mean separation and the existence of 'loops' and 'tails' extending perpendicular to the surface. The polymer conformations are essentially the same as for an isolated polymer. During the quench, the majority of polymers simply fold up by themselves; successively smaller proportions of the molecules form dimers, trimers, etc., leading to a monotonic, rapidly

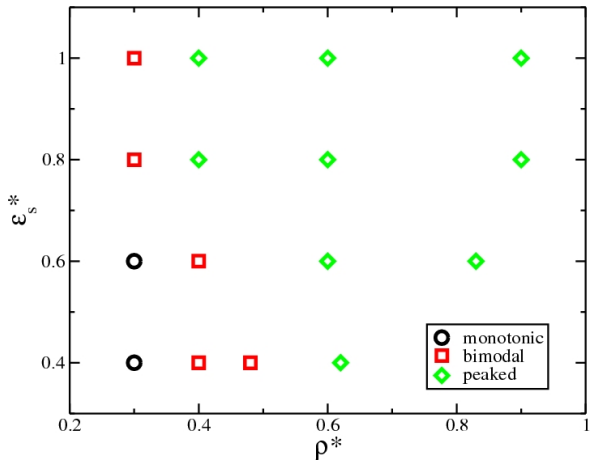

Figure 3.11: (Color online) 'Phase diagram' in the plane of surface density ρ^* and surface-interaction parameter ε_s^* for polymers with $N = 200$ beads in bad-solvent conditions ($\lambda = 1$), showing the occurrences of cluster distributions which are either monotonic decreasing with cluster size, bimodal, or single peaked.

decaying cluster distribution. At high density and with a high surface-interaction parameter, the polymers are held flat on the surface and hence the chains form many more contacts with their neighbors. Therefore, during the quench, polymers aggregate with their neighbors and go on to form large clusters. The cluster distribution is consequently peaked at a relatively large value. At intermediate values of the density or the surface-interaction parameter, the polymer conformations are not significantly different from those of isolated polymers, but there are many more opportunities for forming contacts with neighbors. These factors favor a mixture of the extremal processes described above, and so give rise to a bimodal cluster distribution.

3.4 Conclusions

In this work we have used Langevin dynamics simulations of a coarse-grained, bead-spring model to gain insight on the adsorption of linear polymers on to a smooth surface. The main experimental results we set out to understand are AFM images of polymers physisorbed from solution on to mica surfaces during a process of rapid solvent evaporation. We mimicked this process by switching the bead-spring model interactions from good-solvent to bad-solvent conditions. Of particular interest was the experimental observation of a bimodal cluster distribution. We have shown that this feature is favored at low-to-moderate polymer concentrations, and over a broad range of polymer-surface interaction strengths. At high concentrations, a single-peaked distribution is observed; at low concentrations, and with weak polymer-

surface interactions, a monotonically decaying cluster distribution is obtained. The trends observed in simulations have been rationalized in terms of the probable numbers of contacts between polymers before quenching from good-solvent to bad-solvent conditions.

We have measured and rationalized the trends in a variety of other properties including the fraction of monomer units bound to the surface, the height of the adsorbed polymer film, and the radius of gyration of an adsorbed polymer chain. An additional, incidental result of this study is the reproduction of an algebraically decaying density profile within the 'central regime', as predicted by de Gennes using scaling arguments [44]; the simulation results are consistent with the prediction that the monomer density as a function of the perpendicular distance from the surface (z) decays like $z^{-4/3}$. The existence of the central regime has been confirmed experimentally [45, 46, 47, 48] and in Monte Carlo simulations of lattice models, [49, 50, 51] but as far as we're aware, this has not been demonstrated before in simulations of an off-lattice model.

Future experimental and simulation work will be focused on the adsorption and clustering of star polymers on smooth surfaces. In addition, the kinetics of adsorption and clustering will be explored in detail. For now, we note that two distinct mechanisms for the self-assembly of adsorbed polymers were identified through inspecting movies of the simulated quenching process. In the first mechanism, weakly adsorbed chains first collapse in to individual globules, which then slowly diffuse over the surface and coalesce. The cluster distribution then appaerently reaches a steady state on the simulation timescale. This process was more common with small chains (with $N = 50$ beads) at low concentrations. The second mechanism involves the development of contacts between the polymers prior to quenching, i.e., in good-solvent conditions. Upon quenching, the chains collapse in to one another, and form more extended structures. Occasionally, we observed a chain bridging between two others, and causing all three to collapse simultaneously. These mechanisms were favored by longer chains ($N = 200$ beads) at high concentrations.

Chapter 4

Adsorption and self-assembly of star polymers on surfaces

4.1 Introduction

Star polymers are a special case of branched polymers. They are single molecules composed by f flexible polymer chains tethered to a core particle, where f is called the functionality. The average conformation of a star polymer in a dilute solution is well understood by the standard star blob model, introduced by Daoud and Cotton [65] and further developed in the work of Birshtein *et al.* [66, 67]. In the Daoud-Cotton model, the interior of the star is regarded as a succession of concentric shells of blobs, see Fig. 4.1. For $f = 1$ and 2 a star resembles a linear polymer meaning that for low functionalities, star polymer exhibit highly aspherical conformations [68, 69]. However, as the functionality is increased, asphericity significantly drops and the stars become spherical and "stiffer" [70, 71, 72]. A star polymer is therefore a hybrid between polymer-like objects and colloidal particles bridging two different domains of physics. A great of interest has been generated recently on how stars behave in the proximity of a substrate. One such interesting example is how stars act as depleting agents for colloidal particles, and how they can be used to control colloidal aggregation to produce desired ordered structures [3, 4, 5]. The situation of star polymers on flat surfaces is of particular interest not only due to the academic insights it can provide but also for potential industrial and technological applications. On the basis of previous theoretical [73, 74, 75] and simulation [76, 77, 78] work on star polymers on flat surfaces one can categorise the structures as belonging to one of two categories. In the first case the star polymers are near the adsorption transition, in which the polymer conformation has (almost) identical statistics when the star polymer is in the bulk, see Fig. 4.2(a). In the second category the star polymer

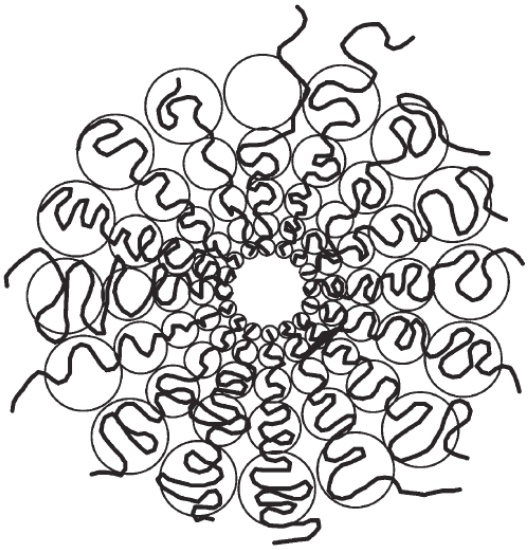

Figure 4.1: (Colour) A scematic illustration of the Daoud-Cotton blob model of a star polymer.

statistics are greatly affected by polymer's core being tethered on the surface, see Fig. 4.2(b). The latter has been studied both on repulsive or marginal surfaces, whose conformations are called star-brushes and in (strong) attractive surfaces (quasi) two-dimensional polymer conformations are created. Nevertheless, there is an intermediate case in which adsorption of the star polymer structure is driven only by van der Waals interactions (physisorption) on a surface as see Fig. 4.2(c). The resulting polymer structures are expected to show bulk statistics that is intermediate between two-dimensional to three-dimensional limiting cases. This intermediate type of interaction has been been omitted in the literature to date.

In recent work by our groups, we studied the physisorption and self-assembly of linear [1] and star [2] polymers on smooth surfaces using atomic-force microscopy (AFM). In a typical experiment, a polymer solution was prepared in good-solvent conditions at concentrations below the critical overlap volume fraction (ϕ^*), resulting in well-separated chains in solution and hence precluding any strong degree of structural ordering within the polymer component. Polymer (sub-)monolayers were formed by exposing a smooth surface (such as highly ordered pyrolytic graphite or mica) to the polymer solution. The surface was then placed in a good solvent bath for several hours and extensively rinsed with good solvent to remove any non-adsorbed polymer. Finally, the samples were dried gently under a stream of nitrogen and subsequently imaged in air by AFM in tapping mode to investigate the resulting structures from this good solvent-to-bad solvent 'quench'. Depending on the polymer molecular weight, architecture, and concentration, very different surface structures

can be obtained.

For the case of linear polymers under certain conditions two distinct types of cluster were found, giving rise to a bimodal cluster-height distribution. A report of the experimental investigation is in preparation [1], and a simulation study yielding insight on the experimental results is in Ref. [79]. Using the same experimental procedure, we have studied the adsorption of star polybutadiene (PB) on to mica from toluene. The functionality and concentration of star polymers control a crossover between 'polymer' and 'soft-colloid' regimes, being distinguished by characteristic cluster topologies, sizes, and surface coverages [2]. In this work we aim to reproduce, and gain insight on, the transition from star-polymer to soft-colloid regimes using Langevin dynamics simulations of coarse-grained 'bead-spring' models of star polymers.

In the past, the properties of a star polymer and its crossover between 'polymer' and 'soft-colloid' regimes has been examined experimentally, theoretically, and with computer simulations. In particular computer simulations have helped to confirm the predictions of the Daoud-Cotton model and its scaling concepts [55, 56]. They have also made possible to obtain the effective interactions between star polymers and thus further coarse-grain the whole star polymer as one ultra-soft particle [80]. This technique has provided valuable insights on the properties of star polymers, including the phase diagram [80]. Despite the numerous simulations studies of star polymers it is still largely unknown how the star polymers behave in the proximity of an attractive surface. Part of problem, namely, the lack of simulation studies focusing on this problem, is that the star's architecture poses a significant challenge for Monte Carlo (MC), molecular dynamics (MD), and Brownian dynamics (BD) techniques. For example, lattice Monte Carlo simulations permit only a small number of arms, less than 20, to be studied, while continuum Monte Carlo runs into problems when dealing with systems with strong density fluctuations [81]. On the other hand MD and BD simulations can study the properties of many-arms star polymers, but not yield information on the number of configuration and thus the calculation of characteristic exponents in scaling theory.

In this chapter we report a simulation study of adsorbed star-polymer films. We use Langevin dynamics simulations of coarse-grained 'bead-spring' models to gain insight on the results from polymer adsorption experiments. The outline of the study is as follows. Firstly, we study the properties of isolated adsorbed polymers (vanishing surface coverage). For the purposes of comparison with the case of finite surface coverage, we reconsider specific single-molecule structural properties for the particular coarse-grained models being employed. Next, we deal with many polymers on a surface under good-solvent conditions, corresponding to the prelude

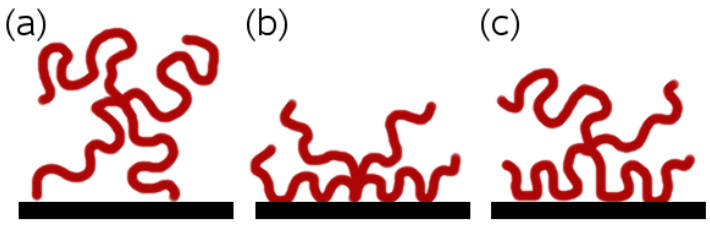

Figure 4.2: (Colour) Scematic illustration of the different categories of polymer adsorption; (a) near the adsorption transition; (b) center-adsorbed; (c) physisorbed.

to the bad-solvent quench in experiments. Finally, we simulate the good solvent-to-bad solvent quench, and its effects on the structure of the polymer film. The chapter is organized as follows. Section 4.2 contains details of the coarse-grained polymer model, and the simulation methods. Results for isolated polymers and many polymers are presented in section 4.3. Section 4.4 concludes the chapter.

4.2 Simulation Model & Methods

4.2.1 Simulation Model

Star polymers are composed of f flexible linear chains, which are tethered to a small central core to form a single molecule. Accordingly, in this work the star polymers are modelled with f polymer chains, which are attached/bonded to a core particle. Each chain is composed by N beads of equal size and mass connected by springs. The size of the core particle may be larger than the size of the beads especially for $f > 32$, to allow for the construction of a stable molecule without any bond breaking. We emphasise that the core size, which was kept as small as possible, is insignificant as compared to the star's overall structure. A star of f arms and N beads per arm will be expressed in the following notation f/N. Further details on the model interactions and simulation methodology can be found in section 3.2.

4.3 Results & Discussion

We have studied three different situations using Langevin dynamics simulations: (i) the behavior of an isolated star polymer on a surface in good-solvent conditions ($\lambda = 0$); (ii) the behaviour of an isolated star polymer on a surface in various solvent qualities ($0 < \lambda \leq 1$); (iii) the behavior of many star polymers on a surface in athermal solvent conditions (i.e. $\lambda = 0$), corresponding to the experimental situation before the bad-solvent quench; and (iv) many star polymers in bad-solvent conditions ($\lambda = 1$)

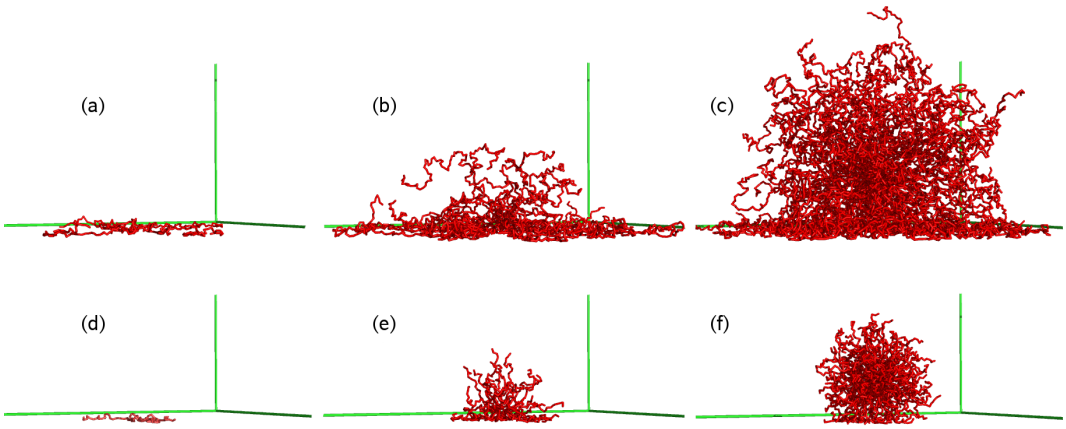

Figure 4.3: (Colour) Screenshots showing isolated stars 4/100, 32/100 and 128/100 from left to right on the top row, and 4/25, 32/25 and 128/25 from left to right on the bottom row. The interaction strength of surface is $\varepsilon_s^* = 0.6$.

corresponding to the post-quench state probed in the AFM experiments. We have studied star polymers with eight different functionalities ($f = 2$, 4, 8, 16, 32, 50, 64 and 128), and three different chain lengths ($N = 25$, 50 and 100), on different surfaces having surface-energy parameters $\varepsilon_s^* = \varepsilon_s/\varepsilon = 0.4$, 0.6, 0.8 and 1.0; in the case of many-polymers, a range of surface coverages was explored.

4.3.1 Isolated star – Athermal solvent

In the proximity of a surface, the number of available possible conformations of a star polymer is reduced, leading to a decrease in entropy. The 'adsorption transition' can be said to be the point where the star polymer is (weakly) physisorbed on the surface, but the distance of the core from the surface is such that the number of available configurations is not significantly less than the number in bulk. Essentially, the structure of the star polymer is similar to that in the bulk. Other studies have explored how the conformation of star polymers with the cores tethered to a surface [76]. In the case of repulsive or marginal surfaces the core particle being tethered on the surface keeps the star polymer adsorbed despite the entropic penalties. The configuration of a star polymer interacting with a marginal surface with a small center-surface distance, is similar to that of a bulk star polymer with twice as many arms [82]. In the case of strongly attractive surfaces center-adsorbed star polymers resemble (quasi) two-dimensional polymers. However, to the best of the knowledge of the authors' no work has examined the case of star polymers adsorbed on attractive surfaces but without the core been tethered on the surface. The resulting star polymer configuration is a balance between the star's arms attempt to minimise the energetic contribution of

the free-energy arising from polymer-surface interactions and minimise the entropy penalties for the star being near the surface. Additionally, this biased preference of monomers towards the surface breaks (alters) the isotropic nature of the star polymer. In this work we study the surface effects on a physisorbed star polymer and how it changes its conformation from low to high values of f. We study model parameters corresponding to the physisorption regime, meaning that the interaction between a bead and the surface is of order $\sim k_B T$; adsorption is favoured because of the large number of contacts between individual beads and the surface.

All isolated polymer simulations began by placing a star polymer in good-solvent conditions ($\lambda = 0$) and close enough to the surface for adsorption to occur. The equilibration time needed varied with different values of f, N and ε_s^*. Equilibration was complete within $2 \times 10^5 \delta t$ for the smallest molecules and upto $8 \times 10^6 \delta t$ for the largest. Finally, the measured properties were averaged over a production run of $4 \times 10^6 \delta t$.

In Fig. 4.4 we show how the behavior of the average maximum height of the star, $\langle h \rangle$, and the average height of the core particle, $\langle h_{\text{core}} \rangle$, in different perspectives as a function of the functionality. In the first perspective we plot the ratios $\langle h \rangle / R_c$ and $\langle h_{\text{core}} \rangle / R_c$, where R_c is the root mean square center-end distance of a star polymer in bulk,

$$R_c = \langle \frac{1}{f} \sum_{\text{end points } i}^{f} (\mathbf{r}_i - \mathbf{r}_{\text{core}})^2 \rangle^{1/2}. \tag{4.1}$$

The first ratio provides the information on how much the overall structure is affected by the star's interaction with the surface, while the second ratio describes the position of the core particle and how much the star polymer has been deformed by exposing the core particle on the surface. In both cases, both ratios increase with increasing f and approach the values 2 and 1, respectively, corresponding to a structure of a star on a surface which is similar to that in the bulk. Nevertheless, we make some important observations. The first observation is for the 128/25 star with $\varepsilon_s^* = 0.4$, $\langle h \rangle$ is slightly above $2R_c$. This happens because even though the star has a very similar structure to that in the bulk being quite spherical due to the high values of f, the few arms having monomer contacts with the surface are stretched to increase the monomer contacts. The stretching of these arms increase the overall height of the star polymer. The second point concerns the change in $\langle h_{\text{core}} \rangle / R_c$ in going from the 2/25 to 4/25 star. The decrease observed is a consequence of a transition from unbranched to branched architecture. At $f = 2$ the star is effectively a linear chain and the position of the core particle can be anywhere between the surface and the maximum height of the molecule. However, adding one or two more arms creates a higher density of monomers around the core making it more favorable for it to be

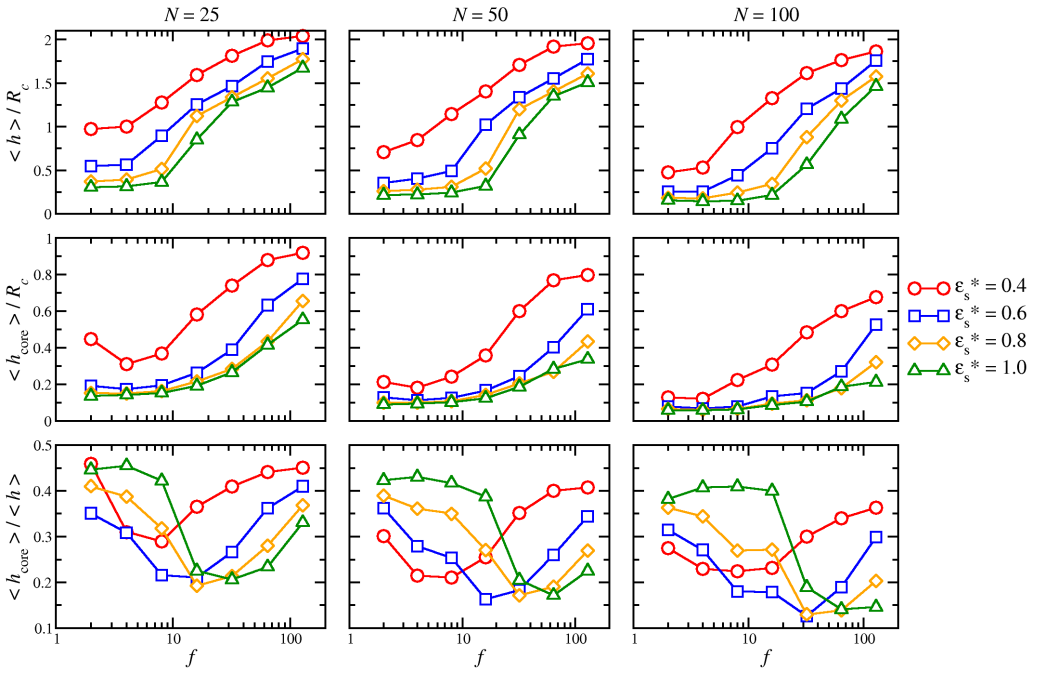

Figure 4.4: (Colour) The figures at the top row show the ratio of the maximum height of the star, $\langle h \rangle$, over the end-to-center distance of a star in the bulk, as a function of f with a surface for various values of ε_s^*. At the middle row the figures show the ratio of the distance of star's core particle between core particle and the surface, $\langle h_{\text{core}} \rangle$, over the end-to-center distance of a star in the bulk, as a function of f with a surface for various values of ε_s^*. The figures at the bottom row show the ratio between the height of the core particle, $\langle h_{\text{core}} \rangle$, over the maximum average height of the star, $\langle h \rangle$.

close to the surface and from the monomer-surface interactions. Nevertheless for higher values of ε_s^* at low f, $\langle h_{\text{core}} \rangle / R_c$ remains low and at the same level, meaning that the core particle remains close to the surface, see Fig. 4.3 (a) and (d).

In the second perspective, we look at the ratio $\langle h_{\text{core}} \rangle / \langle h \rangle$ as function of f. This quantity describes the relation between the height of the star and the position of its core. For low values of f the ratio $\langle h_{\text{core}} \rangle / \langle h \rangle$ has values slightly less then 0.5, which means that the core is located slightly lower than the mid-height of the molecule. The ratio has higher values and closer to 0.5 for more attractive surfaces because possible tails or large loops from the arms contributing to $\langle h \rangle$ diminish. Thus even though the core particle is close to the surface - as indicated by $\langle h_{\text{core}} \rangle$ - the ratio increases for more attractive surfaces.

Above a threshold value of f the ratio $\langle h \rangle / R_c$ increases significantly, with $\langle h_{\text{core}} \rangle / R_c$ following the lead but at a different rate. This happens because as f is increased the number of arms effectively saturates the region near the core of the star, where the whole structure is essentially flat on the surface. At that point $\langle h_{\text{core}} \rangle / \langle h \rangle$ significantly drops because any new arms will find the surface too crowded and they will

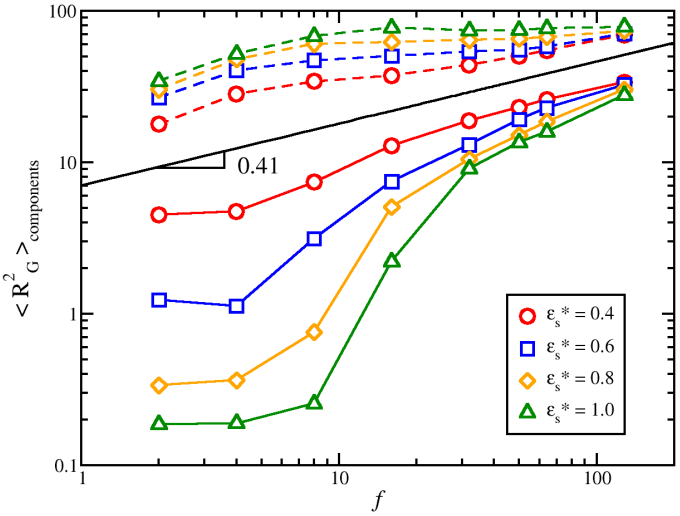

Figure 4.5: (Colour) The figure displays the vertical (continuous line) and parallel (dashed) components of radius of gyration, $\langle R_G^2\rangle_\perp$ and $\langle R_G^2\rangle_\parallel$, for star polymers having $N = 25$ in various surfaces. The black line has slope 0.41, corresponding to $\langle R_G^2\rangle \sim f^{0.41}$.

become free chains, which greatly contributes to the increase of $\langle h\rangle$, see Fig. 4.3(b) and (e). There are two characteristic conformational features, the first one is that the adsorbed arms form a disk lying on the surface, and the second feature is that, due to crowding, some arms become free chains and form a small 'fountain', see Fig. 4.3. At this threshold there is an increase of $\langle h_{\rm core}\rangle/R_c$, because the area around the core particle becomes more crowded and that brings the core particle further away from the surface.

At higher values of f, the ratios $\langle h\rangle/R_c$, $\langle h_{\rm core}\rangle/R_c$ continue to increase towards to values 1 and 2 respectively. The ratio $\langle h_{\rm core}\rangle/\langle h\rangle$ reaches a minimum and continues with an increase towards to 0.5. The star polymer essentially starts to regain its bulk shape and features, and the effects of the surface are reduced. The star polymer star now starts to resemble a hemispherical, [Fig. 4.3(c)] or spherical droplet [Fig. 4.3(f)]. In other words the star behaves like a soft-colloid, since it is stiff enough to resist the 'flattening' effects of the surface. The variation of $\langle h_{\rm core}\rangle/\langle h\rangle$ with ε_s^* is in reverse of what is observed in the 'linear polymer' regime. For star polymers, a reduction of the monomer-surface interaction brings $\langle h_{\rm core}\rangle/\langle h\rangle$ closer to 0.5.

To understand further the behavior of the adsorbed star polymer, we draw attention to the radius of gyration,

$$\langle R_G^2\rangle = \frac{1}{N_t^2}\left\langle \sum_{i=1}^{N_t}\sum_{j=i}^{N_t}(\mathbf{r}_i-\mathbf{r}_j)^2\right\rangle. \tag{4.2}$$

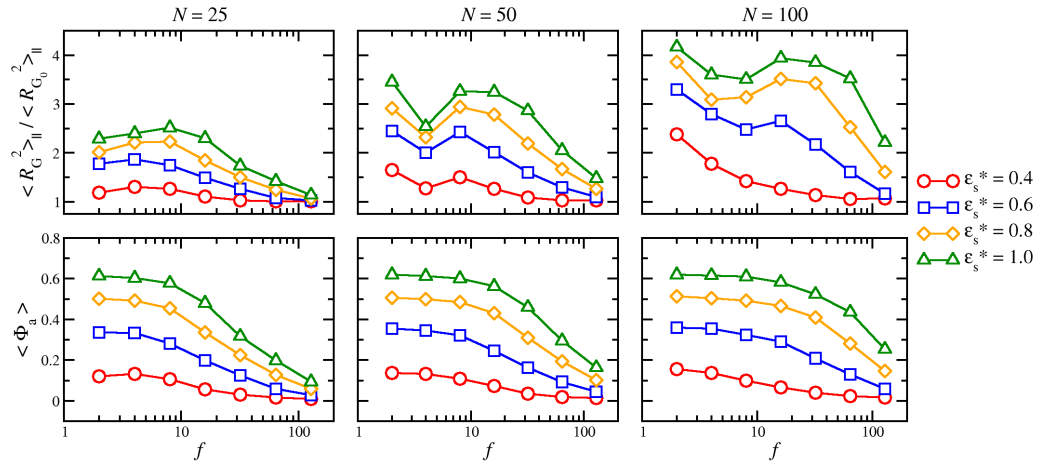

Figure 4.6: (Colour) The figures of the top row show the ratio of radius of gyration $\langle R_G^2 \rangle_\parallel$ of a star polymer on a surface with diferent ε_s^*, over the radius of gyration of a star polymer in bulk (i.e. no surface), $\langle R_{G_0}^2 \rangle_\parallel = \frac{2}{3}\langle R_{G_0}^2 \rangle$, as a function of functionality, f, and for the three diffrent arm lengths $N = 25, 50, 100$.

where $N_t = Nf+1$. It is well known that for star polymers in solution $\langle R_G^2 \rangle \sim N^{2\nu} f^{1-\nu}$, with ν being the correlation length exponent. In good solvent conditions $\nu = 3/5$, therefore $\langle R_G^2 \rangle \sim N^{1.18} f^{0.4}$. When a star is away from a surface, $\langle R_G^2 \rangle$ is expected to scale in a isotropic fashion. But near a surface, we need to consider the dimensions of the star polymer with respect to the surface. Therefore, we will resolve the vector $\mathbf{r}_i - \mathbf{r}_j$, in eq. 4.2 in components perpendicular ($\perp$) and the parallel ($\parallel$) to the surface, and generate the corresponding radii of gyration labelled $\langle R_G^2 \rangle_\parallel$ and $\langle R_G^2 \rangle_\perp$, the sum of which equals $\langle R_G^2 \rangle$. As seen in Fig. 4.5 for the case $N = 25$, the components of $\langle R_G^2 \rangle$ deviate significantly for low functionality and for higher values of the surface interaction strength, ε_s^*. At very high values of f, the star is "stiff" enough to maintain the spherical shape it had away from the surface. Thus in the proximity of a surface isotropy breaks down with the collapse of scaling with f, that is $\langle R_G^2 \rangle$ is no longer $\sim f^{0.4}$, see Fig. 4.5. The strong interaction with the surface significantly alters the structure of a low- or mid-functionality adsorbed star.

In Fig. 4.6 we plot the ratio of the parallel component of the radius of gyration of an isolated star on the surface over its value in the bulk, $\langle R_G^2 \rangle_\parallel / \langle R_{G_0}^2 \rangle_\parallel$. The ratio essentially describes the degree of the effects on the shape/size of the star caused by the surface. The ratio has values higher than 1 since the polymer spreads on the lateral directions of the surface. As seen above a low functionalities the star has a two-dimensional conformation and for high functionalities the star polymer regains its bulk statistics. A star polymer having a two-dimensional conformation means that we can use the scaling arguments for two-dimensional stars that is $\langle R_G^2 \rangle_\parallel \sim f^{1-3/4}$,

where we have used the value of characteristic exponent, $\nu = 3/4$, in two dimentions. This leads to the prediction that

$$\langle R_G^2 \rangle_{\parallel} / \langle R_{G_0}^2 \rangle_{\parallel} \sim f^{1-3/4} / f^{1-3/5} = f^{-3/20} \tag{4.3}$$

However, the results in Fig. 4.6 do not agree with eq. 4.3. We interpret the results as follows. At $f = 2$ (equivalent of linear chain) the ratio is > 1 meaning that the star has spread out on the surface compared with that away from the surface. As f increases a more complex image emerges. Instead of following eq. 4.3 there is a significant decrease of the ratio meaning for example that a $4/50$ star is not affected as much as a $2/50$ star on a surface. This becomes more pronounced for stronger surface interactions. The interpretation for this behavior is that each arm of the star polymer behaves as a linear chain. For low values of f each arm on the surface is well separated from the rest of the arms of the star and hence there is little or no interaction between the arms. In other words each arm is affected by the surface in the same way as in the isolated chain of the same length. This interpretation explains the ratio's values for $4/50$ and $4/100$ stars being at the same level with the values of $2/25$ and $4/50$ stars, respectively. Overall, it indicates that a star of low functionality and with long arms on a strong attractive surface resembles a network of linear chains, with the core particle being its hub (or contact point). However, this behavior is expected to be a finite effect. As obeserved in Fig. 4.6 the depth of the minimum is smaller for $N = 100$ than for $N = 50$. Hence, for longer arms the depth would become smaller, and the behaviour would be better described by eq. 4.3. As f increases there is an increase of $\langle R_G^2 \rangle_{\parallel} / \langle R_{G_0}^2 \rangle_{\parallel}$, because the new arms start to interact and to compete for space (crowding effect), which leads to the star stretching out more on the surface. As seen in Fig. 4.3(a) and (d), the star resembles a two-dimensional object, thus new arms will have more pronounced effects on the structure of the star polymer. For high values of f the ratio descreases and approaches to 1, because the star starts to distance itself from the surface (also see Fig. 4.4) and regains the bulk characteristics and shape.

In Fig. 4.6 we show the average bound fraction $\langle \Phi_a \rangle$ as a function of f, where the bound fraction is defined as the fraction of beads within the interaction range of the surface defined using the distance-based criterion $z \leq 1.2\sigma$. For details see subsection 3.3.1. At low f the behavior of $\langle \Phi_a \rangle$ remains at the same level for the case of linear chains ($f = 2$), since all arms are adsorbed on the surface and essentially each behaves like a linear chain. Having more arms, will create crowding effects and after a certain threshold the star will have arms not being adsorbed, thus reducing the bound fraction.

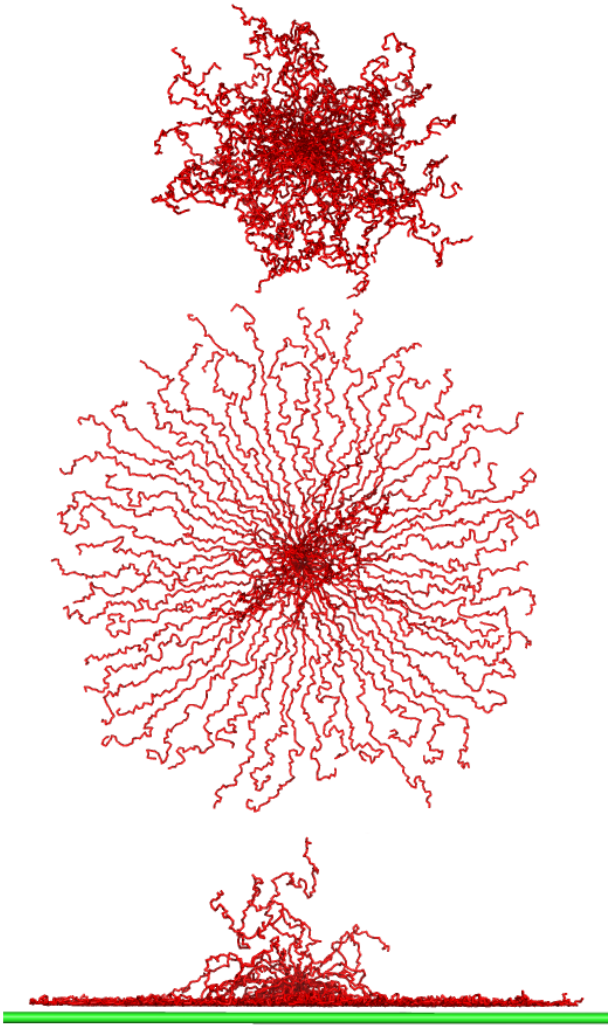

Figure 4.7: (Colour) Snapshots of 64/100 star polymer. The top snapshot shows the star polymer conformation in the bulk. The mid and bottom snapshots display the topview and sideview, respectively, conformation of the star on a surface with $\varepsilon_s^* = 1.0$ showing how much it has spread on the surface.

To further understand the behavior of a physisorbed star on a surface we looked at its shape. There many ways to characterize the shape of an arbitary object; in particular for polymers one can gain valuable insights by looking at the shapes of random walk, for an overview conserning star polymers see Ref. [83] In this work we will use the characterization developed by Runidick *et al.*[84] in which the asphericity, A_d, is defined as

$$A_d = \frac{\sum_{j>i}^{d} \left\langle (L_i^2 - L_j^2) \right\rangle}{(d-1) \left\langle \left(\sum_{i=1}^{d} L_i^2 \right)^2 \right\rangle} \tag{4.4}$$

where L_i are the principal components of the squared radius of gyration, and d is the number of the principal components. The quantity A_d has 0 as its lower bound

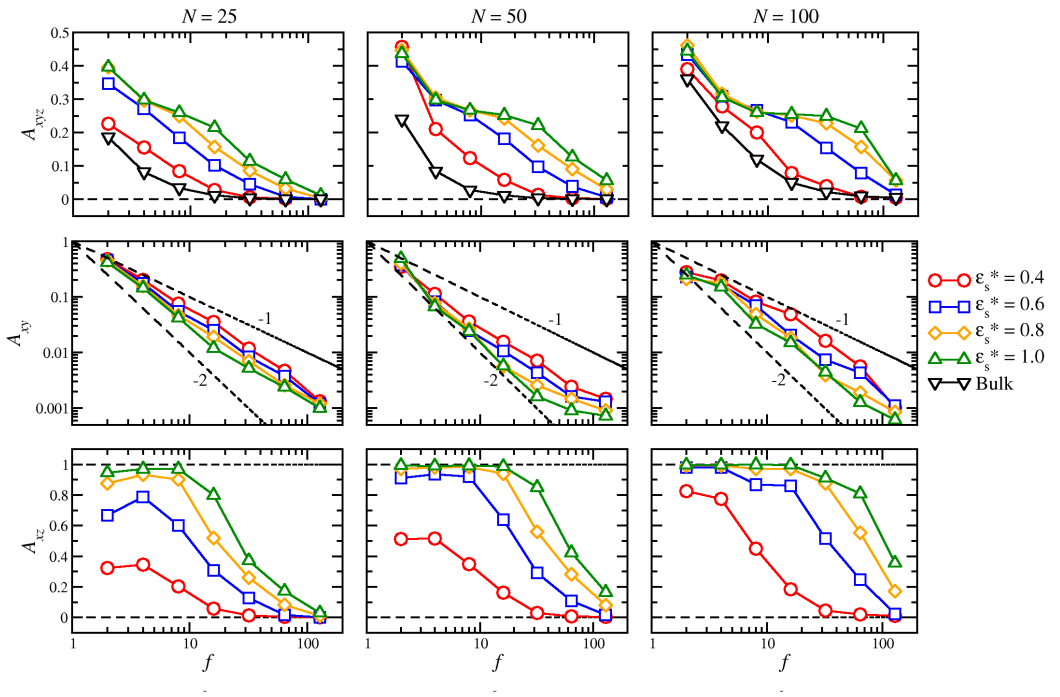

Figure 4.8: (Colour) The figure displays the degree of asphericity, for $N = 25$, 50 and 100 as a function of f for different values of ε_s^*. In the top row the ratio of A_{xyz}/A_{xyz}^* and in bottom row the A_{xz} are plotted.

and it is achieved when the object has a spherical shape, and has upper bound of 1 when it is extended in one dimension (rod-like). In Fig. 4.8 we plot A_{xyz} (three-dimensional asphericity) of a star in the bulk and on a surface for different surface energy interactions. It provides information on how much the surface has affected a star's shape. In previous studies it was found that in the bulk the asphericity drops as $\sim f^{-1}$ [83], which is in agreement with our results in the bulk. However, the results for stars on the surface show a more complex picture. For this reason in Fig. 4.8 we also plot the A_{xy}, which is the two-dimensional asphericity with the beads' positions projected on to the surface. The quantity A_{xy} has a weak power-law dependence that scales with $\sim f^{-1.4}$, which is different from that found in the bulk $\sim f^{-1}$. Moreover, in Fig. 4.8 we plot the asphericity in the x, z directions, A_{xz} that is one parallel and one perpendicular to the surface. The values of A_{xz} provide a more clear description of an adsorbed star measuring the degree of flatness. The results show that for high values of ε_s^* and low values of f, A_{xz} has values near 1 meaning that the profile of the star spans only the dimensions parallel to the surface. In other words the star lies flat on the surface. Note that the longer the arms are, the higher the functionality is required to start regaining its bulk shape; in the case of $N = 100$ the threshold is $f = 32$. That is because longer arms have more monomer contacts with the surface and with their energetic contributions the star adopts configurations with higher

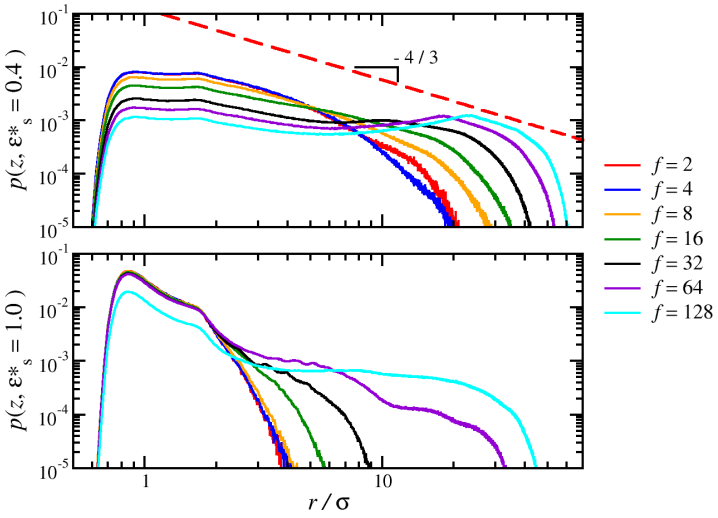

Figure 4.9: (Colour) The figures display the density profiles of adsorbed stars of $f/100$ on surfaces with $\varepsilon^*_s = 0.4$ (top) and $\varepsilon^*_s = 1.0$ (bottom).

entropic costs. Thus one can adjust the strength of the surface interaction and the length of the arms of a star and convert a high f star into a (nearly) two-dimensional object, see Fig. 4.7. A more detailed investigation of the transition of an adsorbed star between being a two- and three-dimensional regimes is in preparation.

In Fig. 4.9 we plot the probability density $p(z)$ of finding a bead at a perpendicular distance z from the surface for $\varepsilon^*_s = 0.4$ and $\varepsilon^*_s = 1.0$ for adsorbed stars with $f/100$ stars. In all cases there is either a local minimum or a point of inflection in $p(z)$ at $z \simeq 1.2\sigma$, and the position of these features was taken as a distance-based criterion for assessing whether a particular bead is 'bound' to the surface or not. Note that from eq. 3.7 the minimum bead-surface potential energy is located at $z/\sigma = \sqrt[6]{2/5} \simeq 0.86$; this distance corresponds to the positions of the primary peaks in $p(z)$. The first two peaks observed in Fig. 4.9 arise from two ordered bead layers on the surface. A third peak is observed in the case of $\varepsilon^*_s = 0.4$ at $f = 64$ and 128; it corresponds to the position of the star's core particle. Additionally, for $z > h_{\text{core}}$ the density profile $p(z) \sim z^{-4/3}$, which corresponds to the Daoud-Cotton picture [65], in which the bulk interior of a star in good-solvent conditions and with suffiently long arms possesses a region in which the monomer density profile follows a power law as a function of the distance from the star's center. In other words, the arms of high-functionality stars remote from weakly attractive surfaces remain unpertubed by adsorption effects.

From the results presented here three different structures have been identified, and we use the following terminology. The *linear regime* corresponds to the case where the arms do not interact significatly with one another, and so the star polymer

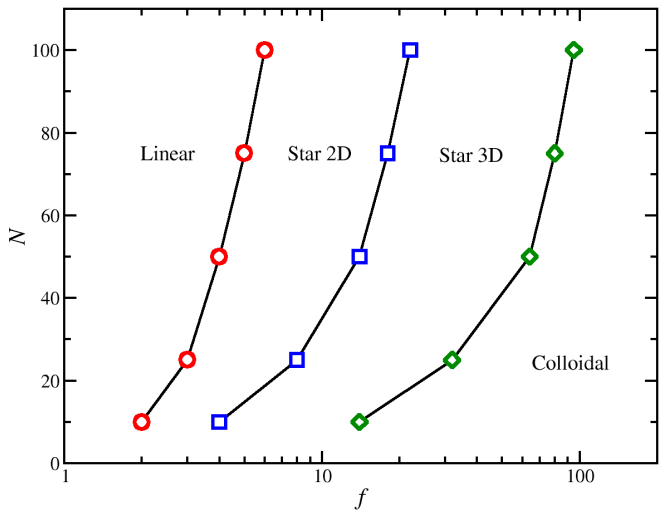

Figure 4.10: (Colour) The figure display the different regimes of a N/f star polymer on a surface with $\varepsilon_s^* = 1.0$.

acts like a network of loosely-coupled linear chains. The *colloidal regime* applies when the star resembles an ulta-soft colloid. The *star regime* is intermediate between the linear and colloidal regimes. Within the star regime, a star polymer on a surface may only extend in the lateral directions and thus it behaves like a two dimentional object. We identify the boundaries between the linear and star regimes using the minimum occuring of $\langle R_G^2 \rangle_\parallel / \langle R_{G_0}^2 \rangle_\parallel$ in Fig. 4.6. The transition between a two-dimensional star and three-dimensional star occurs at the point just before $\langle h_{\text{core}} \rangle / \langle h \rangle$ significantly decreses, after which at least one arm is desorbed from the surface. Finally, the boundary between the star and colloidal regimes is identified using the minimum occuring in $\langle h_{\text{core}} \rangle / \langle h \rangle$. These regimes mentioned above are plotted in a 'phase diagram' as shown in Fig. 4.10.

4.3.2 Isolated star - Solvent Effects

In this section we focus on the effects of the solvent on the structure of an isolated adsorbed star polymer. Once the star polymer had adsorbed in athermal solvent ($\lambda = 0$) followed the following procedure described in the previous section, the solvent quality was adjusted by changing λ to the desired value. The molecule was equilibrated for around $2 \times 10^6 \delta t$, and then properties were measured over a production run of $4 \times 10^6 \delta t$. Note that if a change in solvent quality was more than $0.4 = \lambda_{\text{new}} - \lambda_{\text{old}}$ then intermediate equilibration cycles of $10^6 \delta t$ were performed after increments of $\Delta\lambda = 0.1$ until the desired value was reached. The solvent parameter values we have explored, apart from $\lambda = 0$ corresponding to athermal solvent, are

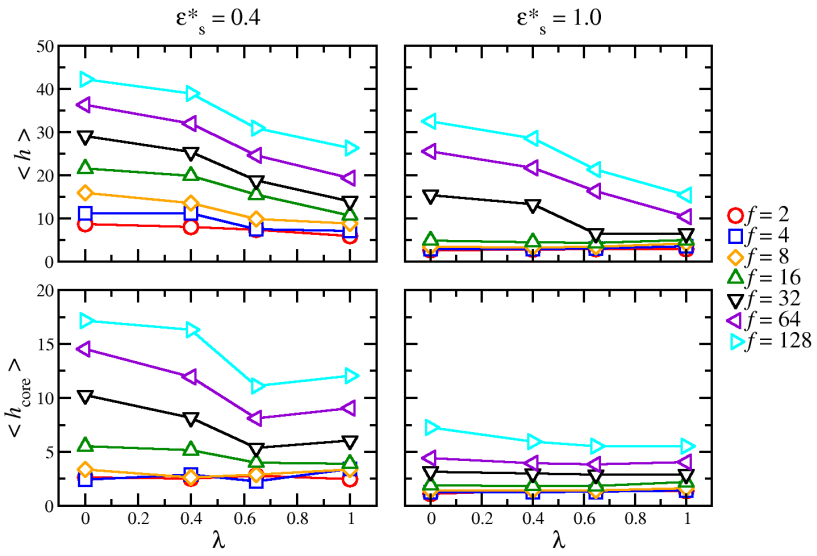

Figure 4.11: (Colour) The diagrams display the behavior height an adsorbed star polymer $f/50$ (top row) and its core particle (bottom row). For comparison the quantities are presented for different monomer-surface interactions, $\varepsilon_s^* = 0.4$ (left column) and $\varepsilon_s^* = 1.0$ (right column).

$\lambda = 0.4$, 0.646 (θ-solvent) [58] and 1.0.

Changing the solvent quality means that the monomer-monomer interactions become less repulsive and the crowding effects are reduced. This has an immediate result; the star polymer shrinks in size. In Fig. 4.11 this effect is observed by measuring $\langle h \rangle$ and $\langle h_{\text{core}} \rangle$. Both quantities are reduced by descreasing the solvent quality. Nevertheless, a deviation from this behavior has been observed when entering in to the bad-solvent regime for small values of ε_s^*, i.e. $\varepsilon_s^* = 0.4$. The height of the star polymer is getting smaller, while the height of the core particle, $\langle h_{\text{core}} \rangle$ is slightly increased. This is more pronouced for higher values of f. The interpretation of this behavior is that the monomer-monomer interactions become significant compared to the monomer-surface interactions; the monomers adopt a more spherical configuration in an attempt to minimize the surface contact with the bad solvent. Adopting a more spherical configuration pushes the position of the core particle towards the center of the star and away from the exterior surface of the star.

In Fig.4.12 we present results for $\langle R_G^2 \rangle_{\parallel}$ and Φ_{a}. As described above when the solvent quality is lowered the star polymer shrinks in size. The behavior of $\langle R_G^2 \rangle_{\parallel}$ agrees with this description for both monomer-surface interactions being considered ($\varepsilon_s^* = 0.4$ and 1.0). On the other hand the bound fraction differs by exhibiting the following interesting behavior. Φ_{a} remains at the same level as the solvent quality changes from good-to-ideal solvent conditions. A small decrease of Φ_{a} is observed when the star polymer enters into bad-solvent conditions. For $\varepsilon_s^* = 1.0$ the entrance

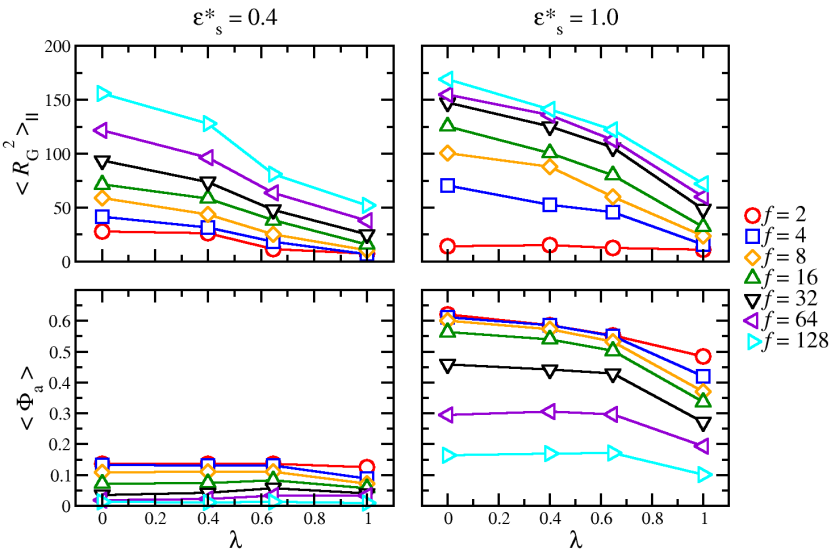

Figure 4.12: (Colour) The diagrams display the behavior of the $\langle R_G^2 \rangle_\parallel$ of an isolated adsorbed star polymer $f/50$ (top row) and its bound fraction $\langle \Phi \rangle$ (bottom row). For comparison the quantities are presented for $\varepsilon_s^* = 0.4$ (left column) and $\varepsilon_s^* = 1.0$ (right column).

into bad-solvent conditions Φ_a has a more significant decrease than for $\varepsilon_s^* = 0.4$.

In Fig. 4.13 we summarize the effects of the solvent on the star's conformation. As the solvent quality shifts from good to ideal the star structure "shrinks" in the sense that the crowding effects are not as pronouced as in the case of athermal solvent conditions, compare Fig. 4.13(a) and (b). The maximum height of the star and the height of the core are both reduced. Additionally, the bound fraction remains roughly at the same level. Nevertheless, as we shift from ideal-solvent to bad-solvent conditions two different behaviors are observed. In the first one the star polymer attemts to minimise its surface contact with the bad solvent with a hemishperical or almost spherical shape (droplet). The height of the star is further reduced but the height of the core is increased because it moves closer to the center of the star's spherical shape, see Fig. 4.13(c). The dominant factor behind this behavior is that the monomer-monomer interactions become energetically more significant than the monomer-surface interactions. If the monomer-surface interactions still dominate the energetic contributions to the free energy then the overall shape of the star will be similar to that shown in Fig. 4.13(d), where both the heights of the star and its core are reduced.

Additionally, a strong monomer-surface interactio can have drastic effects on the structure in the lateral directions. Fig. 4.14 shows a comparison between star configurations on surfaces with $\varepsilon_s^* = 0.4$ and $\varepsilon_s^* = 1.0$, these differences can be observed. In the case of $\varepsilon_s^* = 0.4$ the collapsed polymer has a nearly globular shape, but

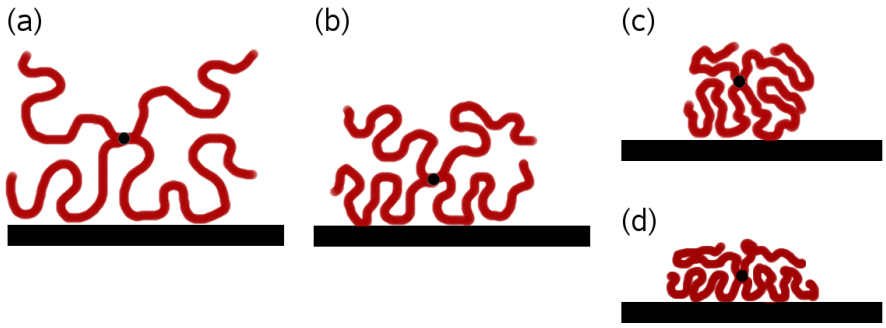

Figure 4.13: (Colour) Schemate illustration of the conformation changes of star polymer on an attractive surface; (a) good solvent conditions; (b) near θ-solvent conditions; (c) bad solvent conditions and the monomer-monomer interaction is stronger than the monomer-surface interaction; (d) bad solvent conditions and the monomer-monomer interaction is weaker than the monomer-surface interaction.

in the case of $\varepsilon_s^* = 1.0$ the star has an irregular/asymmetrical shape. Nevertheless, the latter converges to a more regular/symmetrical shape for high values of f, i.e. $f \geq 32$. This is an important observation because with strongly interacting surface one can manipulate the shape of the star polymer in the bad solvent conditions.

4.3.3 Many adsorbed stars - Athermal solvent

In good-solvent conditions, polymers experience purely repulsive effective mutual interactions. Appropriate simulations with $\lambda = 0$ were initiated by preparing configurations with many polymers on a surface, and equilibrating for around $5 \times 10^6 \delta t$. Due to computational constraints we were restricted by the number of molecules, $N_p = 20\,000/fN$, where 20 000 is the total number of beads used in all simulations (without counting the core particles). Increasing the number of arms, the number of molecules decreases thus making simulations of even modest values of f computationally expensive. For this reason in this study we investigated only the following star polymers 2/25, 4/25, 8/25 and 16/25. Following equilibration, we performed a production run of $4 \times 10^6 \delta t$.

The adsorption is measured by the equilibrium surface bead density, defined in terms of the number of beads N_{ads} belonging to those stars with at least one bead-surface contact, defined using the distance-based criterion $z \leq 1.2\sigma$. Note that N_{ads} is, in general, greater than the number of beads actually bound to the surface. The reduced surface bead density is $\rho^* = N_{\text{ads}}\sigma^2/L^2$. Furthermore, in the adsorbed state we define an effective intramolecular two-dimensional density of an isolated star ρ^* as

$$\rho_{\text{iso}} = \frac{N}{A_{\text{iso}}} \tag{4.5}$$

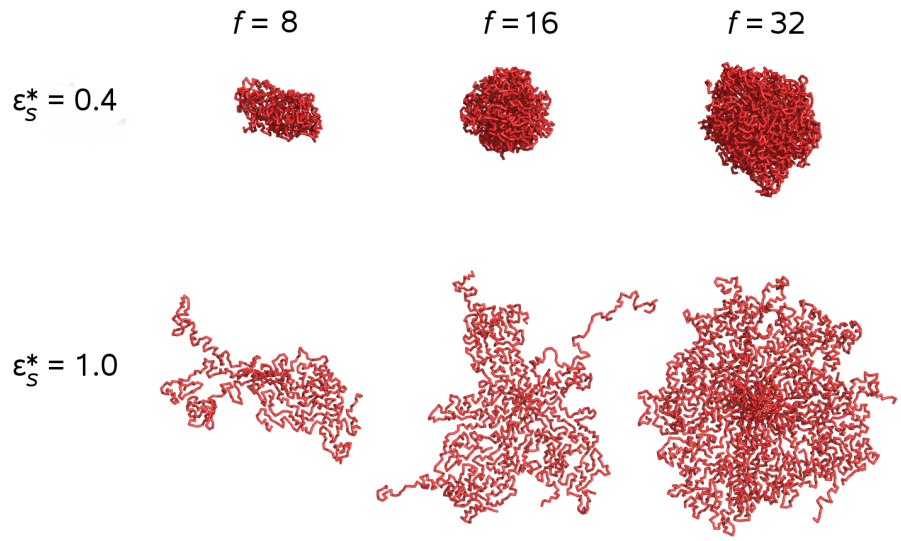

Figure 4.14: (Colour) Snapshots of configurations of $f/100$ star polymers in bad solvent conditions on surfaces from a top-view perspective. The top row is for $\varepsilon_s^* = 0.4$ and the bottom row is for $\varepsilon_s^* = 1.0$. From left to the right the columns display the configurations of stars with 8/100, 16/100 and 32/100, respectively.

where A_{iso} is the area covered on the surface by the adsorbed polymer, given by $A_{\text{iso}} = \pi\langle R_G^2\rangle_{\parallel}$, where $\langle R_G^2\rangle_{\parallel}$ is the parallel component of the radius of gyration of an isolated adsorbed polymer. ρ_{iso} can also be used to define the critical overlap concentration between star polymers. The dilute regime corresponds to $\rho^* \ll \rho_{\text{iso}}$; in this regime the individual stars are almost independent and nearly unperturbed. For $\rho^* > \rho_{\text{iso}}$, the excluded volume constrains lead to interaction effects between adsorbed star polymers. Now, we introduce the scaling variable

$$\gamma = \frac{\rho^*}{\rho_{\text{iso}}} \tag{4.6}$$

in terms of which $\gamma = 1$ corresponds to the critical overlap concetration. By placing a number of stars on surfaces of various dimensions, we simulated surface densities, up to that corresponding to the critical overlap concetration. In other words, the simulations were perfomed at surface concetrations (within the film) approaching the semidilute regime. During equilibration runs near the critical overlap concentration, some of the polymers were seen to desorb as the polymer film approached the steady state.

In Fig. 4.15 we present the behavior of $\langle h\rangle$ and $\langle h_{\text{core}}\rangle$ with varying surface density. For very small surface densities the star polymers are dispersed on the surface, and so we expect identical results with those of an isolated star polymer. Nevertheless, the

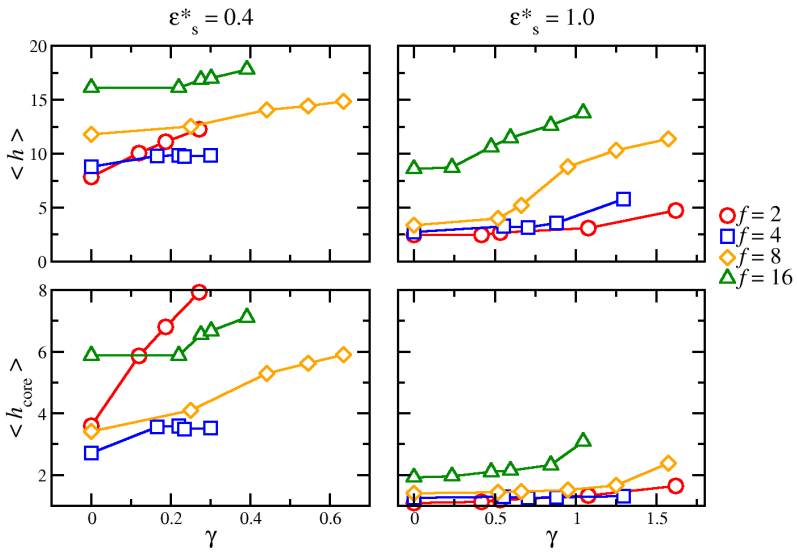

Figure 4.15: (Colour) The diagrams display the behavior of the average maximum height of adsorbed stars $f/25$ (top row) and their core particles (bottom row). For comparison the quantities are presented for for different monomer-surface interactions, $\varepsilon_s^* = 0.4$ (left column) and $\varepsilon_s^* = 1.0$ (right column).

surface density critical value beyond, which the polymer conformation significantly changes, varies with functionality and the monomer-surface interaction. Under weak-adsorption conditions ($\varepsilon_s^* = 0.4$) only small values of γ could be addresses due to desorption, which reduced the number of star polymers on the surface. For the case of linear chains ($f = 2$) one expects the critical density threshold to be much higher than for $f > 2$. This is confirmed for strong adsorption conditions. Under weak adsorption conditions the chain conformation is more sensitive to changes in density. A possible interpretation is that the adsorbed chains can overlap with other chains without entropic restrictions by adopting configurations that contain long tails or loops.

This effect can be seen in Fig. 4.15, which shows that the height of the core particle is more sensitive to changes in density for lower functionality star polymers. The rate of change of $\langle h_{\text{core}} \rangle$ with density for $f = 2$ is much higher than that for $f = 4$ or 8, while in the case of $f = 16$ the rate remain negligible. For $f > 2$ the values of $\langle h \rangle$ remain at the same level within the range of $0 \leq \gamma < 0.2$; beyond this range there is an increase. That is because at $\gamma \approx 0.2$ the star polymers start to feel the presence of their neighbouring star polymers. Similar behavior is observed under strong-adsorption conditions ($\varepsilon_s^* = 1.0$). The difference is that the density threshold, for the star polymer statistics to change is at $\gamma \approx 0.5$. In the strong monomer-surface interaction case, $\langle h \rangle$ starts to increase earlier than $\langle h_{\text{core}} \rangle$, due to crowding monomer effects on the surface. This situation arises by the star polymer shrinking in the lateral directions

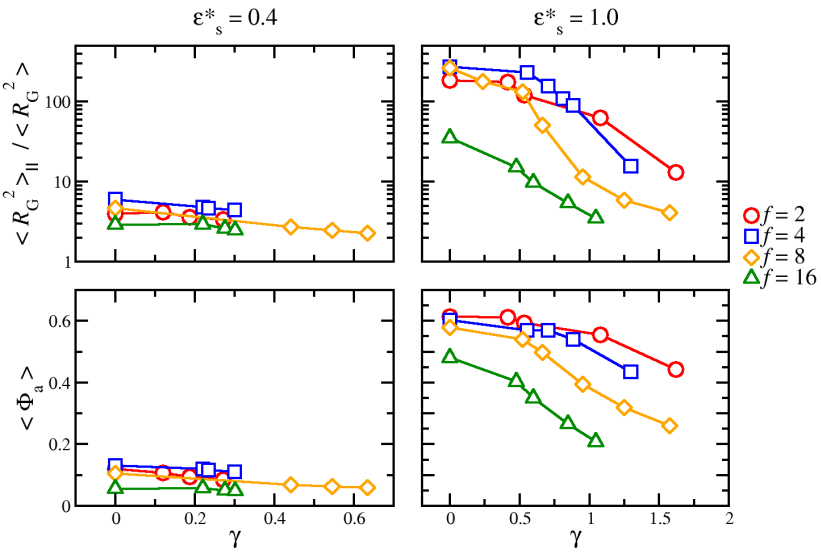

Figure 4.16: (Colour) The diagrams display the behavior of the ratio of the parallel over the vertical component of the radius of gyration, $\langle R_G^2\rangle_\parallel / \langle R_G^2\rangle_\perp$, of adsorbed stars $f/25$ (top row) and their bound fraction (bottom row). For comparison the quantities are presented for for different monomer-surface interactions, $\varepsilon_s^* = 0.4$ (left column) and $\varepsilon_s^* = 1.0$ (right column).

and then, if the crowding effects persist, some arms desorb from the surface. The reasoning is similar to the case of isolated star of varying functionality.

In Fig. 4.16 we display the behavior of the ratio of the parallel and the perpendicular components of the radius of gyration, $\langle R_G^2\rangle_\parallel / \langle R_G^2\rangle_\perp$, and the bound fraction, Φ_a. The results show that under weak-adsorption conditions small structural changes occur with a small decrease of $\langle R_G^2\rangle_\parallel / \langle R_G^2\rangle_\perp$ by about less that 20%. Even though $\gamma < 0.6$ meaning there is still enough space on the surface for more star polymers to be adsorbed, the star polymers do experience small configurational changes due to their interactions with neighbours. One interpretation for this is that the star polymers diffuse on the surface and eventualy they will "collide" with each other. Once such a collision occurs there would be a degree of interpenetration, which will affect the overall conformation of both colliding stars. Additionally, the functionality plays an important role both on the degree of interpenetration and resulting conformational changes. For example, a star polymer of $f = 2$ will diffuse more easily on the surface than a star of $f > 2$ (keeping the arm length fixed). Additionally, desorption of one of the arms will be more significant in a star of lower functionality. This explains why the conformation of a star $f = 2$ is most sensitive to density changes.

For strong adsorption more significant changes occur, because the star polymer extend further in the lateral directions. The star polymers possess higher values of $\langle R_G^2\rangle_\parallel$ - as shown in Fig. 4.5 - and thus they are more likely to overlap with other

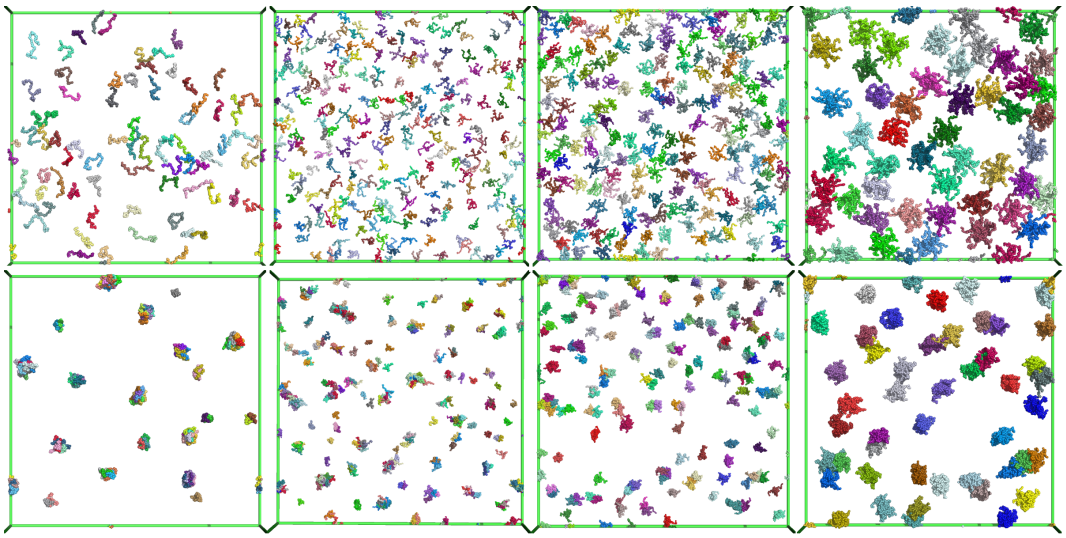

Figure 4.17: (Colour) Top view from simulations of star polymers on an attractive surface $\varepsilon_s^* = 0.4$ in good-solvent conditions ($\lambda = 0$, top) and bad-solvent conditions ($\lambda = 1.0$, bottom). All stars in the figure have $N = 25$ and from left to right $(f, \gamma) = (2, 0.107)$, $(4, 0.186)$, $(8, 0.466)$ and $(16, 0.750)$, respectively.

star polymers. Another key difference with the weak adsorption case is that the configuration of the star polymer will be in the linear- or 2D-star regime. The arms will be flatter on the surface, greatly reducing the opportunities for interpenetration. Another factor that controls the degree of interpenetration is functionality. As functionality increases both the ratio $\langle R_G^2 \rangle_\parallel / \langle R_G^2 \rangle_\perp$ and Φ_a drop, as shown in Fig. 4.16. This is no surprise since functionality controls the "stiffness" of the stars.

4.3.4 Many adsorbed stars - Bad Solvent

The final step in the experimental polymer-adsorption procedure being considered here, is the quench from good-solvent to bad-solvent conditions, corresponding to rinsing with solvent and then drying in nitrogen/air. As described in chapter 3 for the case of linear chains we mimic this step in our simulations by starting simulations from well-equilibrated configurations with $\lambda = 0$ (good solvent) and then instantaneously switching to $\lambda = 1$ (bad solvent). We then re-equilibrate the system for $5 \times 10^6 \delta t$, during which the system was seen to reach an apparent steady state. As discussed in the case of linear polymers in chapter 3 the surface structures are apparently stable for a long period of time. Star polymers diffuse less as functionality is increased, and so in our simulations the structures observed are apparently static on the timescales accessed in the simulations.

In Fig. 4.17 we show examples of equilibrated simulation configurations before ($\lambda = 0$) and after ($\lambda = 1$) the quench, for systems of polymers each made up from

$N = 25$ beads per arm, and with surface-interaction parameter $\varepsilon_s^* = 0.4$, with different functionalities, and at various surface densities. In good-solvent conditions the polymers are in extended conformations, but in bad-solvent conditions they collapse to optimise the attractive bead-bead interactions. Functionality plays a significant role in determining the degree of clustering between the polymers. As seen in Fig. 4.17 even at a low densities, a low functionalities of $f = 2$ or 4 leads to clusters composed of 4 or even 6 polymers, while for $f = 16$ one has to reach higher values of surface coverage ($\gamma \approx 0.750$) to observe a cluster composed of 3 polymers. The interpenetration of this is based on 'stiffness' of the star polymer before the quench. For low functionalities the star polymers diffuse in the lateral directions and once they 'collide' they easily interpenetrate with one another. Once the quench occurs some of the polymers will overlap each other or they are very close together meaning that is highly probable they will form clusters. However, for higher values of f the degree of interpenetration between polymers is greatly reduced. Therefore high functionality stars, prior the quench, position themselves in such a way to minimise the degree of overlapping with each other. Hence, after the quench the star polymers tend to form isolated collapsed globules or small clusters. To observe clustering of high functionality star polymers, one has to significantly increase the surface density resulting an increase to the degree of polymer overlap. Another important factor that contributes is that the functionality greatly reduces the mobility (diffusion) of the star polymers on the surface. This means that the positions of the center of mass of the star polymers on the surface before and after the quench will be roughly the same. Exceptions to this would occur if a star polymer has many bead contacts or entanglements with a neighbouring star polymer prior the quench.

4.4 Conclusions

In this work we have used Langevin dynamics simulations of coarse-grained, bead-spring models to gain insight on the adsorption of star polymers on to a smooth surface. Our motivation was driven by experimental AFM images of polymers physisorbed from solution on to a mica surfaces during a process of rapid solvent evaporation. The process was mimicked by switching the coarse-grained model interactions between those appropiate for good-solvent or bad-solvent conditions. Of particular interest was the experimental observation of the crossover from polymer-like to colloidal behavior. Initially, we examined how the crossover manifests itself in an isolated adsorbed polymer. Three parameters were identified being important for controling the structure of the star on the surface: f, N and ε_s^*. By exploring the

parameter space we mapped the different behaviors onto a 'phase diagram'. Additionally, our methodology allowed us to change the solvent quality by tuning one parameter, λ, thus gaining valuable insights on the conformational behavior of the adsorbed star in different solvent conditions. Finally, we explored systems of many adsorbed star polymers under good-solvent conditions and the corresponding patterns they create once quenched into bad-solvent conditions. The observed patterns were rationalised in terms of the probable interpenetration between polymers before quenching from good-solvent to bad-solvent conditions.

Chapter 5

Neighbor network in a polydisperse hard disk fluid: degree distibution and assortativity

5.1 Introduction

For over four decades the science of complex networks was based on results for random graphs, obtained by Erdös and Rényi in 1959 [85]. Recent analyses reveal that the topologies of most large, real networks deviate from those of random networks [86]. Examples of real networks include the World Wide Web [87, 88], the Internet [89], metabolic systems and protein-protein interactions [90, 91, 92], sexual contacts [93], collaborations between scientists [7] and between movie actors [94], and scoring totals of Brazilian football players [95]. The most significant deviations from random-network behavior appear in the tail of the *degree distribution* p_k, that is the probability of a given vertex possessing connections to k other vertices. In random networks p_k is Poissonian, while p_k for many real networks varies asymptotically like $k^{-\gamma}$, where γ is a positive exponent [94]. In qualitative terms, a *scale-free* network is characterized by a small number of highly-connected vertices called 'hubs'; for a general introduction, see Ref. [96]. Many authors identify scale-free networks as those possessing power-law degree distributions, but as discussed fully in Ref. [97], this is a necessary but not sufficient condition. In what follows, we will be largely concerned with power-law degree distributions, and the term 'scale free' will be employed; but it should be borne in mind that, strictly speaking, other properties are required for the network to be termed scale free [97].

It has been suggested – but not yet confirmed – that growth and preferential attachment are possible mechanisms by which real-world, scale-free networks can

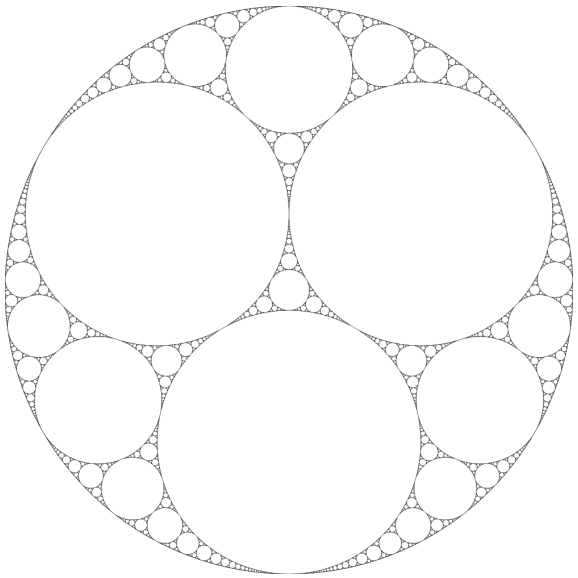

Figure 5.1: An example of an Apollonian gasket. The image was taken from Wikipedia (http://en.wikipedia.org/wiki/Apollonian_gasket).

emerge [86]; the addition of nodes to networks may capture the intrinsic evolutionary behavior of some real-world examples. Dynamical models of the growth of cellular networks – including the effects of cell division and disappearance – can also give rise to scale-free neighbor networks [98, 99]. Stochastic models have been proposed and studied which can successfully reproduce certain features of real networks [94, 100], however there are some features which cannot yet be reproduced. An example is the assortativity of a network [101], which measures the extent to which vertices with equal degree link with one another: in assortative networks, vertices with equal degree are linked to one another more frequently than in a random network; in disassortative networks, vertices with equal degree are linked to one another less frequently than in a random network. To quote Newman, "An interesting observation is that essentially all social networks measured appear to be assortative, but other types of networks (information networks, technological networks, biological networks) appear to be disassortative. It is not clear what the explanation for this result is, or even if there is any one single explanation. (Probably there is not.)" [102]. Nonetheless, it has been shown that assortativity and clustering (which means more linked vertices share a common neighbor than would be expected by chance) can arise if social networks are divided in to distinct groups or communities [103].

Scale-free networks are rare in real and model condensed-matter systems. One important example is the scale-free contact network in the Apollonian packing of circles [104], in which the circle diameter distribution decays according to a power-law with an exponent of about 1.3 [105]. The mechanical, percolation, and conductive

properties of materials possessing Apollonian-packing networks have been shown to exhibit unusual dependences on the number of vertices [104]. In Fig. 5.1 displays an example of Apollonian disks. Such models may describe the distribution of force in granular materials such as concrete, and networks of voids in porous media. The percolation properties of such networks [104, 106] will clearly be of relevance to the characteristics of certain porous media. The Apollonian packing has also been identified as a model for networks of connected minima on potential-energy surfaces of atomic clusters [107]; the transition states (edges) between minima (vertices) exhibit a scale-free distribution [108, 109, 110].

This chapter is concerned with the possibility of generating a simple scale-free network in molecular simulations of a simple fluid. The model consists of polydisperse hard disks in two dimensions, in which the distribution of disk diameters (σ) varies asymptotically like $\sigma^{-\alpha}$, where α is a positive exponent. The equilibrium structure of the fluid phase is determined using Monte Carlo (MC) simulations, conducted at constant pressure (strictly tension). Naïvely one might expect the number of neighbors of a given disk to be proportional to the circumference and hence σ. Due to the broad distribution of particle diameters, neighbors are identified using the radical tessellation [111] proposed as a suitable alternative to the Voronoï construction which is usually applied to one-component systems. If the tail of the diameter distribution follows a power law, then perhaps the neighbor distribution will vary in a similar way. Identifying particles with vertices, and the separation vectors between neighboring disks as edges, this situation could give rise to a scale-free neighbor network, with the large particles playing the role of the hubs. In this section it is shown that: (i) there are indications that the neighbor network in the polydisperse hard-disk fluid possesses a power-law degree distribution, which is one of the properties of a scale-free network; and (ii) the neighbor network is highly assortative, i.e., vertices with equal degree are directly connected more often than in a random network. This is an interesting situation, because the equilibrium properties of the fluid are static, and hence dynamic mechanisms of scale-free network formation, e.g., preferential attachment, are not applicable.

Polydisperse hard-disk fluids are of considerable intrinsic interest, for example as models of colloidal monolayers, froths and foams, and packing and segregation in granular materials. The packing of binary mixtures of hard disks has been studied extensively and is shown to be highly non-trivial [112, 113, 114]; for instance, the distributions of neighbors and of cell area (as obtained from radical tessellations) show distinct contributions arising separately from the small and large disks, indicating the clustering of disks with equal size. Fluids with more than two components have received far less attention, although it has been noted than in some respects the statis-

tics of the radical tesselations may conform to those of a random tesselation [112]. Specifically, it has been found that fluids of disks with a linear, decreasing diameter distribution obey the Aboav-Weaire law, which states that the average total number of sides of the cells (determined by tesselation) neighboring a cell with k sides increases linearly with k [115, 116, 117]. It has been shown that the Aboav-Weaire law is a consequence of a maximum-entropy (ME) principle [118, 119], the argument being that it can be written as a linear superposition of two basic constraints, these being that $\sum_k p_k = 1$, and for a two-dimensional tesselation $\sum_k k p_k = 6$ (Euler); therefore, the Aboav-Weaire law provides no new constraints and so it leads to the ME distribution. It might therefore be anticipated that in the polydisperse hard-disk fluid considered in this work, a maximum-entropy distribution may provide an adequate description of the nearest-neighbor network measured in simulations.

From the viewpoint of liquid-state physics, it is interesting to construct expressions for the equations of state of highly polydisperse fluids. In statistical mechanical terms, this may stimulate progress in understanding dense, complex fluids, such as the mixtures of macromolecules found inside living cells [120]. Therefore, a simple equation of state is derived using scaled-particle theory (SPT) [121], and compared with (essentially exact) results from MC simulations.

This chapter is organized as follows. Section 5.2 details the hard-disk model, summarizes the MC and SPT approaches to be employed, and presents the derivation of an ME estimate of p_k. The results are reported and discussed in Section 5.3, and Section 5.4 concludes the paper.

5.2 Model and methods

The model consists of N hard disks confined to a square cell of area A. The disk-diameter distribution is given by

$$p(\sigma) = \frac{C}{1 + (\sigma/\sigma_0)^\alpha} \tag{5.1}$$

where $\sigma \geq 0$, σ_0 is a reference diameter, α is a positive exponent, and C is the normalization constant. This particular choice of distribution was chosen so that there is a finite number of small particles (important for the simulations), and because it rapidly approaches the asymptotic form $p(\sigma) \sim \sigma^{-\alpha}$. The value of α should be small enough to give a long tail to the distribution, but large enough such that the first few moments are well defined. The second moment is required to exist so that one can define a packing fraction, given by $\eta = \pi\rho\langle\sigma^2\rangle/4$, where the angled brackets denote an average over $p(\sigma)$, and $\rho = N/A$ is the number density. The second moment is

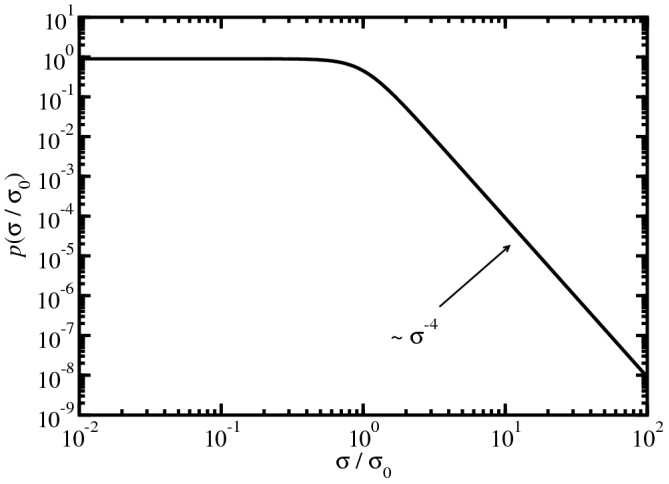

Figure 5.2: Normalized disk-diameter distribution $p(\sigma) = C/[1 + (\sigma/\sigma_0)^4]$ plotted on a log-log scale to highlight the asymptotic σ^{-4} behavior.

finite only for $\alpha > 3$, so present work is focused on the distribution with $\alpha = 4$, the normalization constant and first two moments of which are

$$C = \frac{2\sqrt{2}}{\pi\sigma_0}, \tag{5.2}$$

$$\langle\sigma\rangle = \frac{\sigma_0}{\sqrt{2}}, \tag{5.3}$$

$$\langle\sigma^2\rangle = \sigma_0^2. \tag{5.4}$$

$p(\sigma)$ is plotted in Fig. 5.2 on a log-log scale to show the crossover to a power-law decay for $\sigma \gtrsim \sigma_0$.

5.2.1 Monte Carlo simulations

Constant-temperature, constant-pressure MC simulations of $N = 10^4$ polydisperse hard disks were performed in a square cell with periodic conditions applied [9]. The hard-disk system is athermal and so the reduced pressure employed in the simulations is defined as $P^* = P\sigma_0^2/k_B T$, where k_B is Boltzmann's constant and T is the temperature. Ten different simulation configurations were used, each consisting of particles with diameters drawn randomly from $p(\sigma)$. Results obtained with the ten configurations at a given reduced pressure were averaged.

On average, one MC cycle consisted of N attempted displacements of randomly selected disks, N_A trial displacements of $\ln A$ [9], and one cluster move, the latter

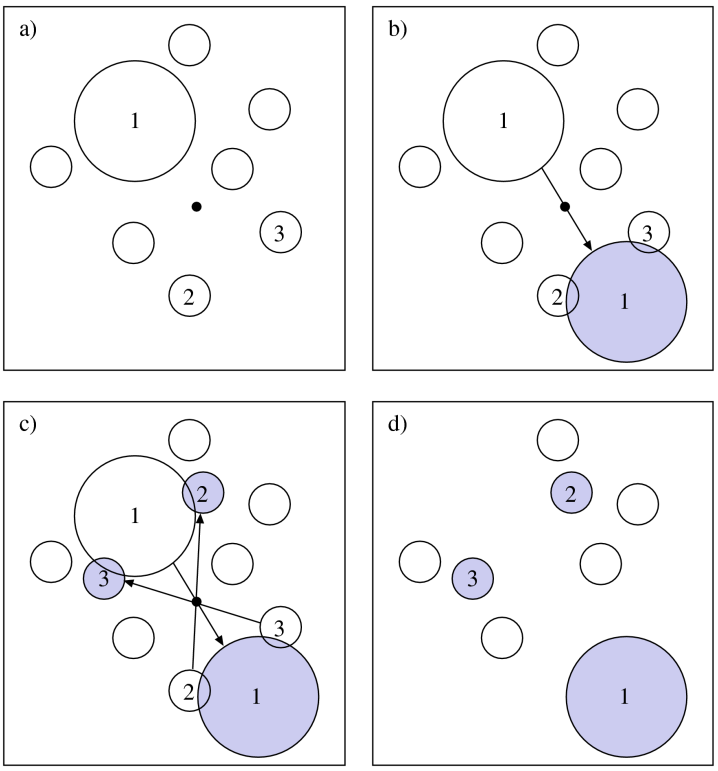

Figure 5.3: A scematic illustration of the cluster move algorithm. (a) Initial configuration. The black dot it the random pivot point; (b) the randomly chosen particle is reflected with respect to the pivot point; (c) particles overlaping with the new position of particle 1 are reflected; (d) the final configuration.

implemented using Dress and Krauth's cluster algorithm [122] with reflection rather than rotation [123]. The cluster moves are vital for equilibration, because the displacements of large disks are severely hampered by the large number of neighboring small disks. In a few words, each cluster move begins with the selection of a random pivot point within the simulation box. A disk is chosen at random, and is subjected to a point reflection about the pivot. Any disks that overlap with the reflected disk are themselves reflected, and this process is repeated until there are no more overlaps, see Fig. 5.3. This algorithm works particularly well at low to intermediate densities, but it fails at high densities due to all of the particles being part of the same 'cluster' [123]. For each state point the equilibration phase consisted of about 10^5 MC cycles with N_A = 1-20, depending on the pressure. Production runs consisted of a further 10^5 MC cycles. At intervals of 10 MC cycles, radical tessellations [111] were computed and the network statistics were incremented. In the standard two-dimensional Voronoï construction, the edges of the tessellation are perpendicular bisectors of the lines joining the centers of neighboring disks. When neighboring disks are of very different size, the bisectors may intersect with the larger disks. In the radical

tessellation, this problem is avoided by forming edges with the loci of points from which the lengths of the tangents to neighboring disks are equal.

5.2.2 Scaled particle theory

The derivation of a simple equation of state from SPT [121] is now summarized. To begin, the excess chemical potential (in units of $k_B T = \beta^{-1}$) of a scaled disk with diameter $\lambda\sigma$ is given in the limit of small λ by the Widom insertion formula [124]

$$\beta\mu^{\text{ex}}(\lambda\sigma) \approx -\ln\left[1 - \rho\int p(\sigma')\,v(\lambda\sigma,\sigma')\mathrm{d}\sigma'\right] \tag{5.5}$$

where $v(\lambda\sigma,\sigma')$ is the excluded 'volume' of two hard disks with diameters $\lambda\sigma$ and σ':

$$v(\lambda\sigma,\sigma') = \frac{\pi}{4}(\lambda\sigma+\sigma')^2. \tag{5.6}$$

The combination of Eqs. (5.5) and (5.6) can be expanded about $\lambda = 0$ up to a linear term. An additional λ^2 term is chosen to yield the correct limit when $\lambda \to \infty$; in the case of a scaled disk with area $\pi\lambda^2\sigma^2/4$ the reversible work of expanding the particle against the macroscopic pressure is $\pi P\lambda^2\sigma^2/4$. The result of these manipulations is an approximation to the excess chemical potential at fixed density and temperature:

$$\beta\mu^{\text{ex}}(\lambda\sigma) \simeq -\ln(1-\eta) + \frac{\pi\rho\sigma\langle\sigma'\rangle}{2(1-\eta)}\lambda + \frac{\pi}{4}\beta P\sigma^2\lambda^2. \tag{5.7}$$

To obtain an equation of state, appeal is made to a relation for hard particles derived by Smith and Labík [125, 126]. Consider the quantity Y defined by the derivative of $\beta\mu^{\text{ex}}$ with respect to λ at $\lambda = 1$, averaged over the diameter distribution of the inserted particle:

$$Y = \int p(\sigma)\left.\frac{\mathrm{d}\beta\mu^{\text{ex}}(\sigma)}{\mathrm{d}\lambda}\right|_{\lambda=1}\mathrm{d}\sigma. \tag{5.8}$$

In microscopic terms, this derivative is related to the infinitesimal work of expanding a full-sized particle against the surrounding fluid. This is given by [127]

$$\begin{aligned} Y &= \rho\int p(\sigma)p(\sigma')g(\sigma,\sigma')\left.\frac{\partial v(\lambda\sigma,\sigma')}{\partial\lambda}\right|_{\lambda=1}\mathrm{d}\sigma\mathrm{d}\sigma' \\ &= \frac{1}{2}\pi\rho\int p(\sigma)p(\sigma')g(\sigma,\sigma')\sigma(\sigma+\sigma')\mathrm{d}\sigma\mathrm{d}\sigma' \end{aligned} \tag{5.9}$$

where $g(\sigma,\sigma')$ is the partial pair correlation function for particles with diameters σ and σ', at contact. The right-hand side of this equation is simply related to the compressibility factor, $Z = \beta P/\rho$, which is easily obtained from the virial equation

[128]:

$$Z = 1 + \frac{1}{8}\pi\rho \int\int p(\sigma)p(\sigma')g(\sigma,\sigma')(\sigma+\sigma')^2 \mathrm{d}\sigma\mathrm{d}\sigma'. \tag{5.10}$$

Comparing Eqs. (5.9) and (5.10) leads to the simple relationship

$$Y = 2\,(Z-1)\,. \tag{5.11}$$

This is the two-dimensional version of a result derived by Smith and Labík in Ref. [126]. Inserting the SPT result for $\beta\mu^{\mathrm{ex}}(\lambda\sigma)$ [Eq. (5.7)] in to Eq. (5.8) yields

$$Y = \frac{2\eta s}{(1-\eta)} + 2Z\eta \tag{5.12}$$

where the packing fraction $\eta = \pi\rho\langle\sigma^2\rangle/4$ and $s = \langle\sigma\rangle^2/\langle\sigma^2\rangle$. Equating Eqs. (5.11) and (5.12) furnishes the final expression for the compressibility factor:

$$Z = \frac{1+(s-1)\eta}{(1-\eta)^2}. \tag{5.13}$$

The expansion of Eq (5.13) to first order in ρ is

$$Z = 1 + \frac{\pi}{4}(1+s)\langle\sigma^2\rangle\rho + \ldots \tag{5.14}$$

which yields the correct second-virial coefficient (equal to half of the average excluded volume)

$$B_2 = \frac{1}{2}\int\int p(\sigma)p(\sigma')\frac{\pi}{4}(\sigma+\sigma')^2\mathrm{d}\sigma\mathrm{d}\sigma' = \frac{\pi}{4}(1+s)\langle\sigma^2\rangle. \tag{5.15}$$

For the disk-diameter distribution in Eq. (5.1) with $\alpha = 4$, $s = \frac{1}{2}$ and $Z = (1-\eta/2)/(1-\eta)^2 = 1+3\eta/2+\ldots$. Note that for the monodisperse hard-disk fluid, $s = 1$ and the familiar SPT result $Z = 1/(1-\eta)^2$ is recovered.

5.2.3 Degree distribution from maximum-entropy theory

We derive a simple, ME estimate of $p_k(\sigma)$, this being the joint probability distribution of neighbors for a disk with given diameter σ. The overall degree distribution p_k is then obtained by integration of $p_k(\sigma)$. The derivation relies on there being constraints on the mean and mean-square number of neighbors for a disk with given diameter. A very small disk is essentially an ideal point particle, and because such small disks are so numerous, the neighbor network will be essentially random with moments that will not depend sensitively on σ. (The degree distribution for Voronoï tesselations of random sets of points in a plane – the 2D Poisson-Voronoï tesselation

– is known [129, 130].) On the other hand, a very large disk is expected to have an average number of neighbors which scales linearly with σ. We make the following *ansatz*; the average number of neighbors for a disk with diameter σ is

$$K_1(\sigma) \equiv \frac{\sum_k k p_k(\sigma)}{p(\sigma)} = a_1 + b_1 f(\sigma) \tag{5.16}$$

where we have used the fact that $\sum_k p_k(\sigma) = p(\sigma)$, and the sums are restricted to $k \geq 3$ because triangles are the smallest polygons in the tesselation. a_1 and b_1 are parameters, and $f(\sigma)$ is a function with the properties $f(0) = 0$, and $\lim_{\sigma\to\infty}[f(\sigma)\sigma_0/\sigma] = 1$. Given the form of $p(\sigma)$, an obvious choice for $f(\sigma)$ is

$$f(\sigma) = \frac{(\sigma/\sigma_0)^{\alpha+1}}{1+(\sigma/\sigma_0)^{\alpha}}. \tag{5.17}$$

The mean-square number of neighbors, $K_2(\sigma) = \sum_k k^2 p_k(\sigma)/p(\sigma)$ is assumed to be such that the width of the distribution for a given σ is constant:

$$\frac{K_2(\sigma) - K_1^2(\sigma)}{K_1^2(\sigma)} = a_2. \tag{5.18}$$

The parameters a_1, b_1, and a_2 are then chosen so that

$$\int p(\sigma) K_1(\sigma) \mathrm{d}\sigma = \langle k \rangle \tag{5.19}$$

$$\int p(\sigma) K_2(\sigma) \mathrm{d}\sigma = \langle k^2 \rangle \tag{5.20}$$

where $\langle k \rangle = 6$ (Euler) and $\langle k^2 \rangle$ are the averages for the whole network, and $\langle k^2 \rangle$ is to be taken from simulation. This leads to the relationships

$$b_1 = \frac{\langle k \rangle - a_1}{\langle f(\sigma) \rangle} \tag{5.21}$$

$$a_2 = \frac{\langle k^2 \rangle}{a_1^2 + 2a_1 b_1 \langle f(\sigma) \rangle + b_1^2 \langle f^2(\sigma) \rangle} - 1 \tag{5.22}$$

where a_1 will be retained as an adjustable parameter. The quantity $K_1(0) = a_1$ should be less than 6 because the average of $K_1(\sigma)$ over the whole diameter distribution – including the large disks – should be precisely 6. For the present diameter distribution (5.1) with $\alpha = 4$, $\langle f(\sigma) \rangle = 1/(2\sqrt{2})$ and $\langle f^2(\sigma) \rangle = 21/32$. We now seek an ME solution

for $p_k(\sigma)$ subject to the following constraints:

$$\sum_k p_k(\sigma) = p(\sigma); \tag{5.23}$$

$$\sum_k k p_k(\sigma) = p(\sigma) K_1(\sigma); \tag{5.24}$$

$$\sum_k k^2 p_k(\sigma) = p(\sigma) K_2(\sigma). \tag{5.25}$$

Maximizing the entropy $S = -\sum_{k\geq 3} p_k(\sigma) \ln p_k(\sigma)$ with respect to $p_k(\sigma)$ (with the method of Lagrange multipliers) leads to the result

$$p_k(\sigma) = \exp\left[\Lambda_0(\sigma) + \Lambda_1(\sigma) k + \Lambda_2(\sigma) k^2\right]. \tag{5.26}$$

where the $\Lambda_i(\sigma)$s are adjusted to satisfy the constraints (5.23-5.25). Finally, p_k is obtained from the relation

$$p_k = \int p_k(\sigma) \mathrm{d}\sigma. \tag{5.27}$$

5.3 Results

5.3.1 Equation of state

Reliable simulation results were obtained for pressures up to $P^* = 2$, corresponding to a packing fraction $\eta \simeq 0.45$. For higher pressures the cluster moves were seen to result in point reflections of increasingly large clusters, which ultimately precludes effective equilibration of the system. Presumably there is no crystallization at very high pressure. The equation of state – plotted as P^* versus η – for the polydisperse hard-disk fluid is shown in Fig. 5.4. The raw data is given in Table 5.1. The SPT (5.13) and virial-expansion (5.14) results are shown for comparison. The SPT is surprisingly good, being accurate for packing fractions up to about 0.3.

5.3.2 Radical tessellation and degree distribution

Simulation snapshots at $P^* = 1$ are shown in Fig. 5.5; the packing fraction at this pressure is $\eta \simeq 0.36$. For clarity, only a subdomain (containing 1600 particles) of a particular configuration is shown. Three different views are displayed: (a) the actual hard-disk configuration; (b) the radical tessellation; and (c) the Delaunay triangles formed by the links between neighboring vertices (defined by disks that share cell edges).

On the basis of the radical tessellations, the degree distribution p_k was constructed, being the probability that a disk has k neighboring disks. Given that ten

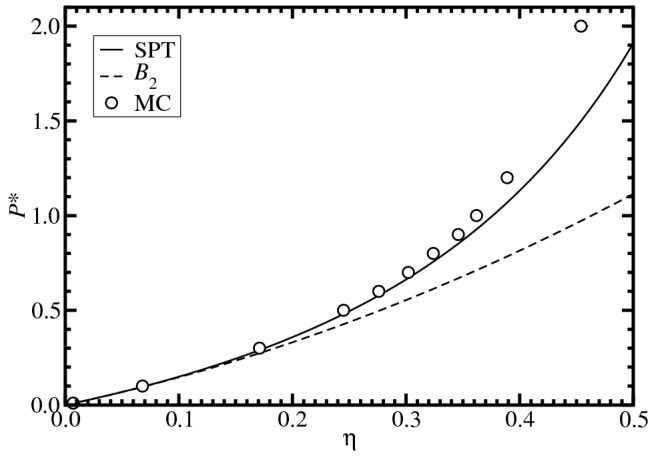

Figure 5.4: Equation of state – reduced pressure $P^* = \beta P \sigma_0^2$ versus packing fraction η: MC simulations (points); SPT (solid line); virial expansion with B_2 (dashed line).

configurations were simulated, each containing 10^4 particles, the lower limit on p_k accessible from our simulations is $\sim 10^{-5}$. In all cases it was confirmed that the average number of links, $\langle k \rangle$, is precisely equal to six. Figure 5.6 shows p_k as measured and averaged from simulations at $P^* = 0.01$, 0.1, 0.5, 1, 1.2, and 2. Error bars on p_k represent the statistical uncertainty in the mean obtained from averaging over the ten distinct configurations. The small-k portions of p_k ($k \gtrsim 10$) show only small variations over the entire range of pressures simulated. At low pressures ($P^* < 0.5$) p_k shows no sign of a long tail. At such low packing fractions, the particle positions are uncorrelated and the degree distribution resembles that of the 2D Poisson-Voronoï tesselation [129, 130]. At pressures in the range $0.5 \leq P^* \leq 1$ it was observed that the tail of p_k for $k \gtrsim 21$ appears as a straight line on a log-log plot, indicating consistency with the power-law decay $k^{-\gamma}$. At higher pressures, no power-law tail is apparent over the range of k accessible in simulations. For all pressures $P^* \geq 0.1$, a kink is apparent in p_k at the point where $p_k \simeq 10^{-4}$. Since the proportions of particles contributing to p_k before and after the kink appear constant, this suggests that p_k is partitioned in to 'small-particle' and 'large-particle' contributions, the latter possibly corresponding to an asymptotic scale-free regime.

Figure 5.7 shows the tails of p_k as measured in simulations with pressures in the range $0.5 \leq P^* \leq 1$. The kinks at $p_k \simeq 10^{-4}$ are more clearly visible. The asymptotic decay of p_k is consistent with a power-law, but it is far from being unambiguous. It is difficult to access larger values of k because of limitations on the number of particles that can be simulated; this restricts the form of the diameter distribution, and in

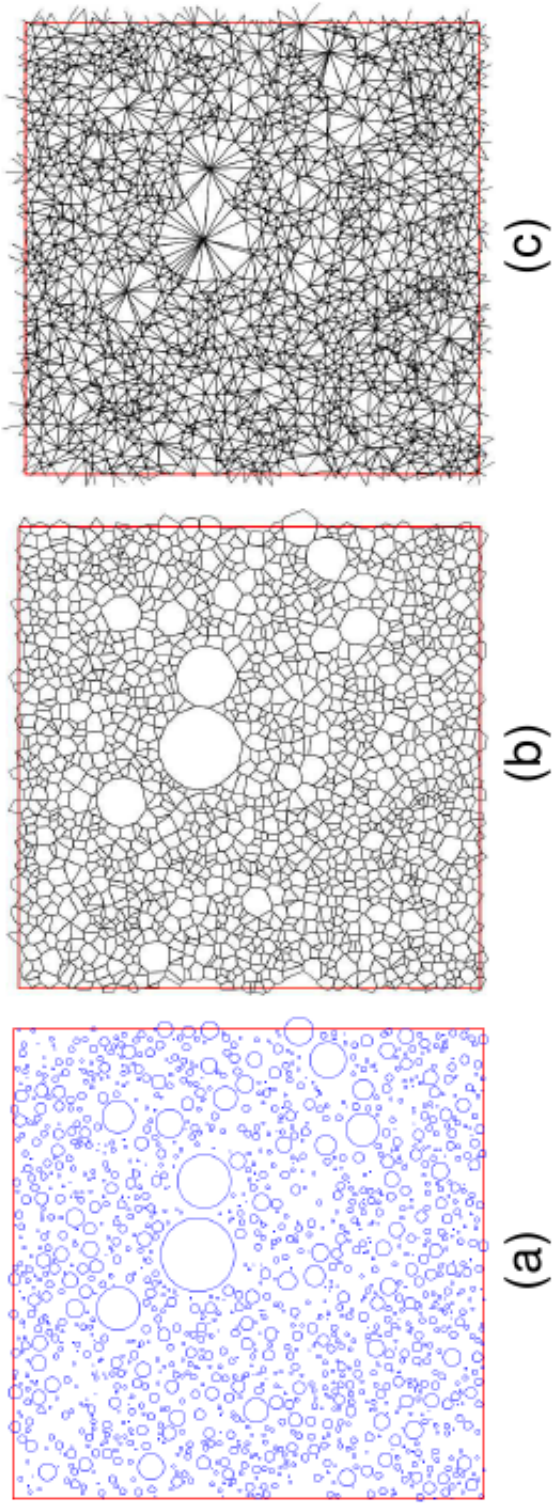

Figure 5.5: (Color online) Sub-domain ($N = 1600$ particles) of a simulation configuration at $P^* = 1$ and $\eta \simeq 0.36$: (a) the actual hard-disk configuration; (b) the radical tessellation; and (c) the Delaunay triangles formed by the links between neighboring vertices.

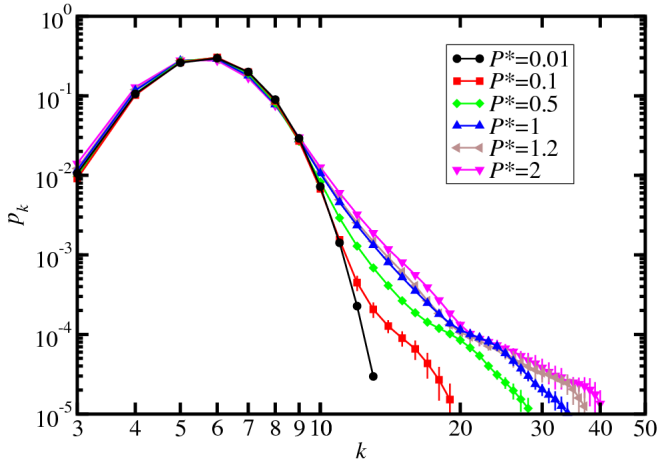

Figure 5.6: (Color online) Near-neighbor distribution functions, p_k, at reduced pressures in the range $0.01 \leq P^* \leq 2$.

particular necessitates the regularization of the distribution at $\sigma < \sigma_0$. Nevertheless, least-squares fitting of power laws to the tails of p_k yields the lines shown in Fig. 5.7. The corresponding fitting ranges and exponents (γ) are reported in Table 5.1.

It has been pointed out that the least-squares fitting procedure may give rise to biased, and hence erroneous, results for the power-law exponent (γ) due to large fluctuations in the tail of the distribution [131, 132]. There is an alternative fitting scheme based on a maximum likelihood estimator (MLE), which for power-laws yields a simple, closed-form expression for the exponent [131, 132]. We implemented this scheme on the cumulative probability, $c_k = \sum_k^\infty p_k \sim k^{-\gamma+1}$, which serves to reduce statistical errors. We report the resulting MLE exponents in Table 5.1; the values are slightly smaller than, but generally consistent with, those obtained from least-squares fitting.

Interestingly, γ is relatively insensitive to the packing fraction, being in the region 5-6; the uncertainties quoted in Table 5.1 are associated with the fitting procedure, and so they are underestimates. Naïvely, if the number of neighbors is proportional to the disk diameter, then one might expect $p_k \sim k^{-4}$; in reality, γ is significantly greater than 4. The apparent exponent $\gamma > \alpha$ can be understood by comparing the MC simulation results with the predictions from the ME theory derived in Section 5.2.3. Figure 5.8 shows p_k from simulations with $P^* = 0.5$ and $P^* = 1$, along with plots of Eq. (5.27) computed using the best-fit parameters $a_1 = 5.50$ and $a_1 = 5.39$, respectively, and values of $\langle k^2 \rangle$ reported in Table 5.1. The ME results are in quite good agreement with those from simulations, although the kink at $p_k \sim 10^{-4}$ is not

P^*	η	$\langle k\rangle$	$\langle k^2\rangle$	w	γ (LS)	γ (MLE)	Range	r
0.01	0.0078(2)	6.00	37.758(4)	0.2210				0.475(8)
0.1	0.068(1)	6.00	37.78(7)	0.2220				0.472(14)
0.3	0.171(2)	6.00	37.88(3)	0.2285				0.467(10)
0.5	0.245(3)	6.00	38.18(3)	0.2445	6.0(1)	5.7	$21 \le k \le 28$	0.456(9)
0.6	0.276(3)	6.00	38.33(4)	0.2525	5.8(1)	5.7	$22 \le k \le 29$	0.448(7)
0.7	0.302(3)	6.00	38.44(4)	0.2581	5.9(1)	5.6	$23 \le k \le 31$	0.441(7)
0.8	0.324(3)	6.00	38.55(5)	0.2641	5.7(1)	5.5	$23 \le k \le 32$	0.433(7)
0.9	0.346(3)	6.00	38.67(4)	0.2698	5.6(1)	5.4	$24 \le k \le 33$	0.424(7)
1	0.362(2)	6.00	38.76(4)	0.2744	5.6(1)	5.4	$24 \le k \le 34$	0.420(6)
1.2	0.389(2)	6.00	38.67(7)	0.2724				0.408(3)
2	0.454(6)	6.00	39.0(1)	0.2901				0.377(6)

Table 5.1: Results from MC simulations of the polydisperse hard-disk fluid with $\alpha = 4$: packing fraction η; mean and mean-square degree, $\langle k\rangle$ and $\langle k^2\rangle$; relative width of the degree distribution, $w = \sqrt{\langle k^2\rangle/\langle k\rangle^2 - 1}$; power-law exponent, γ, for the tail of p_k (and the range over which power-law behavior is observed) from least-squares fitting (LS) and a maximum likelihood estimator (MLE) [131, 132]; assortativity r. Figures in brackets are statistical uncertainties in the last digits based on one standard deviation.

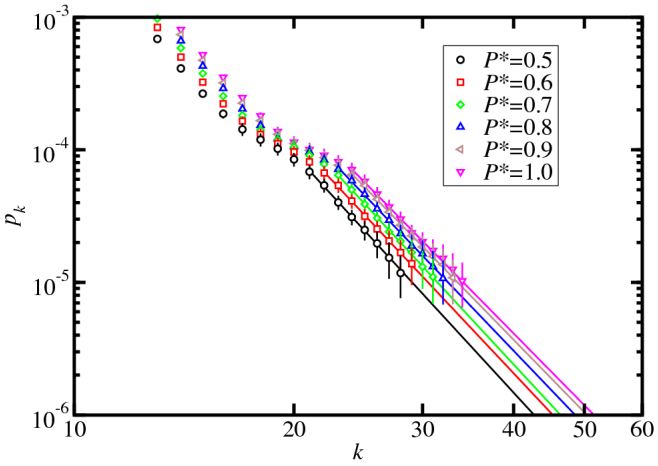

Figure 5.7: (Color online) Tails of the near-neighbor distribution functions, p_k, at reduced pressures in the range $0.5 \leq P^* \leq 1$. The lines are fitted power-law extrapolations $p_k \sim k^{-\gamma}$; the least-squares exponents are reported in Table 5.1.

captured so well. But the main points are that in the region of $k = 20$-30, where the simulation results are consistent with a power-law decay, the ME predictions have apparent exponents greater than 4 (at $k = 20$, $\gamma = -\mathrm{d}\ln p_k/\mathrm{d}\ln k \simeq 5.8$), and that as $k \to \infty$, p_k approaches the anticipated k^{-4} behavior (at $k = 100$, $\gamma \simeq 4.3$). Of course, this is largely a consequence of the prescription for $K_1(\sigma)$. But the agreement between simulation and theory at moderate k suggests that, at large enough k, the simulated network degree-distribution would follow the power law $p_k \sim k^{-4}$.

5.3.3 Assortativity

The assortativity of a network, as defined by Newman [101], reflects the tendency of vertices with equal degrees to cluster. A convenient measure of assortativity is clearly defined in Ref. [101], but for clarity the derivation is reproduced here. The degree distribution of vertices attached to randomly selected edges is not equal to p_k, because high-degree vertices have more links. Instead, the distribution is proportional to kp_k, and the distribution of remaining vertices (not including that attached to the randomly selected edge) is $q_k \propto (k+1)p_{k+1}$. The assortativity can then be related to the joint probability distribution function of there being j and k remaining vertices at each end of the selected edge [100]. Denoting this function by e_{jk}, the following properties are to be noted: for an undirected graph $e_{jk} = e_{kj}$; $\sum_{jk} e_{jk} = 1$; and $\sum_j e_{jk} = q_k$. For networks which are neither assortative nor

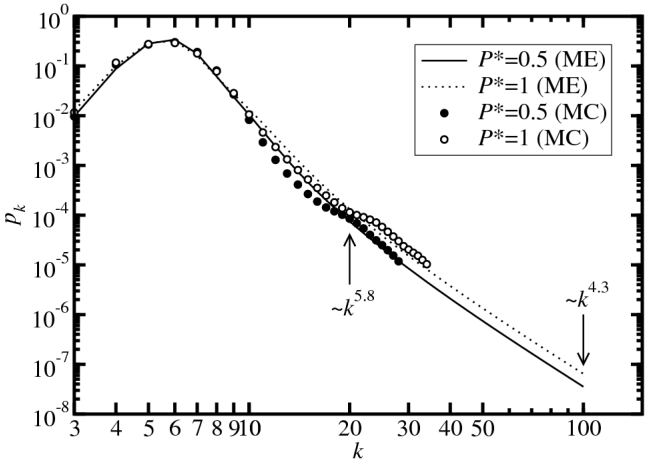

Figure 5.8: Near-neighbor distribution functions, p_k, at reduced pressures of $P^* = 0.5$ (solid points and solid line) and $P^* = 1$ (open points and dotted line) from MC simulation (points) and the ME theory (lines).

disassortative, the degrees of the vertices at the ends of the edge are uncorrelated and so $e_{jk} = q_j q_k$. A correlation function between degrees can therefore be defined as $\langle jk\rangle - \langle j\rangle\langle k\rangle = \sum_{jk} jk(e_{jk} - q_j q_k)$ where the angled brackets denote an average over all edges in the graph. For the comparison of diverse graphs, it is convenient to normalize this correlation function by its maximal value, which corresponds to the case of a perfectly assortative network, i.e., the degrees of connected vertices are identical. In this case $e_{jk} = q_k \delta_{jk}$ and $\sum_{jk} jk(e_{jk} - q_j q_k)$ is equal to the variance, σ_q^2, of k according to the distribution q_k. Finally, then, the measure of assortativity is defined as

$$r = \frac{\sum_{jk} jk(e_{jk} - q_j q_k)}{\sigma_q^2} \tag{5.28}$$

where r ranges from -1 for a perfectly disassortative network, through 0 for a network with no disassortative or assortative mixing (such as a random network [85, 101]) to $+1$ for a perfectly assortative network. The average values of r obtained for the hard-disk neighbor networks are reported in Table 5.1. The results indicate that the hard-disk fluid is strongly assortative at all pressures considered. If the degree of a disk is dictated by its diameter, then in physical terms, the results indicate that 'small' disks are preferentially solvated by other small 'disks'; the 'large' disks – with high degree – are more likely to be solvated by 'small' disks, due to the form of the diameter distribution. Nonetheless, some weak clustering of large disks is apparent in Fig. 5.5, particularly in 5.5(b) and 5.5(c); note the associations between different

'sparse' regions of the network. The physical driving force for the clustering of large disks might be identified with a depletion interaction [133, 134, 135] mediated by the osmotic pressure of the small disks, but of course what constitutes the boundary between 'large' and 'small' is not well defined. r decreases slowly and monotonically with increasing packing fraction. One possibility is that as the packing fraction is increased, particle packing and correlations become more pronounced, and the 'large' disks develop links with an increasing number of neighboring 'small' disks, and the assortativity decreases. This process is, of course, accompanied by a broadening of the degree distribution, as illustrated in Fig. 5.6, and as quantified by the relative width, $w = \sqrt{\langle k^2\rangle / \langle k\rangle^2 - 1}$, reported in Table 5.1. The broadening of p_k, and the resulting effects on q_k, are already taken in to account in the definition of r [Eq. (5.28)].

The assortativities of real networks vary widely. Most 'social' networks, such as scientific co-authorships and movie-actor collaborations, are clearly assortative, with r values up to about 0.4 [101]; successful individuals are often attracted to others. On the other hand, the networks represented by the World Wide Web, the Internet, and most significantly, many biological situations are disassortative (with r values down to about -0.3) [101]; this property may make the network more resilient to random attack, since the hubs (which may play crucial roles in the function of the network) are not connected [92]. The present simulation results indicate that if scale-free neighbor networks do exist in the polydisperse hard-disk fluid at pressures in the range $0.5 \leq P^* \leq 1$, then they are strongly assortative, with values of r comparable to those found in social networks. It is tempting to speculate that the analogues of groups and communities in social networks [103] are 'clusters' of small and large disks in the polydisperse fluid.

5.4 Conclusions

An attempt has been made to realize a scale-free near-neighbor network in computer simulations of a polydisperse fluid of hard disks. Each disk represents a vertex on a graph, and the edges of the graph correspond to links between neighboring disks as identified by a radical tessellation. Working on the naïve assumption that the number of links is proportional to the disk diameter, an asymptotic power-law diameter distribution was expected to give an asymptotic power-law degree distribution. The simulation results are consistent with power-law decay – within the limits imposed by the simulated diameter distribution – but only for a specific range of disk densities in which particle correlations are sufficiently pronounced.

The apparent exponent of the degree distribution γ was found to depend weakly on the disk density, and to differ from the exponent of the diameter distribution α. A comparison with predictions from a maximum-entropy theory suggest that this decay is not the asymptotic one, and that for sufficiently large particles (not accessible in simulations) γ would approach α. The results therefore suggest that, in principle, the near-neighbor network in the polydisperse hard disk fluid may be scale-free. It is anticipated that a similar situation would obtain with different choices of α, but of course α should be as small as possible if a sufficient number of hubs are to be found in a network of finite size. Earlier results [112] and the form of the maximum-entropy theory suggest that non-power-law diameter distributions will not give rise to a scale-free neighbor network. The assortativity of the network was found to be positive over the whole range of disk densities, reflecting a preference for links between vertices of equal degree. In other words, 'small' particles are preferentially solvated by other 'small' particles, and 'large' particles show some tendency to cluster together. Finally, some effort was directed towards analyzing the thermodynamic properties of the fluid. No evidence for crystallization at high packing fractions was found. A simple equation of state – derived from a scaled-particle theory – was demonstrated to be accurate up to moderate packing fractions.

In stochastic models of networks, the position of a vertex on a graph does not influence its degree (i.e., the number of other vertices with which it shares edges). But in the case of hard disks at equilibrium, the degree of a disk is dictated by its size and the sizes of its immediate neighbors, through packing constraints. The spatial correlations in fluids, and therefore the properties of the neighbor network, are dictated by the requirement to minimize the free energy of the system. Hence, the apparent scale-free properties of the network are static, and do not arise from any dynamic mechanism, such as preferential attachment. It would be interesting to find out whether the formation of assortative, scale-free networks in other contexts can be rationalized using equilibrium statistical mechanics.

An experimental realization of a polydisperse 'fluid' could actually be a granular material, with a scale-free size distribution achieved by milling and grinding. Alternatively, by analogy with cellular networks, froths and foams produced with an element of bubble division and disappearance may exhibit a scale-free degree distribution [98, 99]. It should be pointed out, however, that in conventional colloidal fluids, polydispersity is usually better described by log-normal or Γ distributions. The physical properties of two-dimensional materials possessing scale-free networks may be of interest, and demand further study.

Chapter 6

Crystal structures of two-dimensional binary mixtures of dipolar colloids in tilted fields

6.1 Introduction

The crystallisation of colloids confined at liquid-air and liquid-liquid interfaces has recently attracted a great deal of attention [136, 137, 138, 139, 140, 141, 142, 143, 144] due to the large number of potential applications ranging from food and agrochemicals to petrochemicals and pharmaceuticals. Unlike particles in the bulk, the effective interactions between colloidal particles at fluid interfaces are influenced not only by the properties of the particles and the solvent, but also by the surface and line tensions of the interface [143].

From various experimental realisations of binary mixtures of dipolar colloids, two such realisations are related with this work and we briefly describe them here. The first realisation deals with colloidal dipoles, which are roughly spherical particles with diameters in the range 10 nm - 1 μm. For preventing irreversible aggregation the particles are usually coated with a thin layer of non-magnetic material. Thus the net colloid-colloid interaction is mainly dipolar, with the coatings providing a relatively weak short-range dispersion interactions. The colloidal dipoles are suspended in a pendant drop in gravity (system I), see Fig. 6.1(a). In the second, colloids of polystyrene colloids float on an oil-water interface (system II), see Fig. 6.1(b) . The colloids are trapped at the oil-water interface because this way they minimise the surface between the two phases. Nevertheless, the polystyrene colloids do not have a molecularly smooth surface and water molecules are trapped at the colloid-oil interface. This has as a consequence the formation of water droplets or a thin

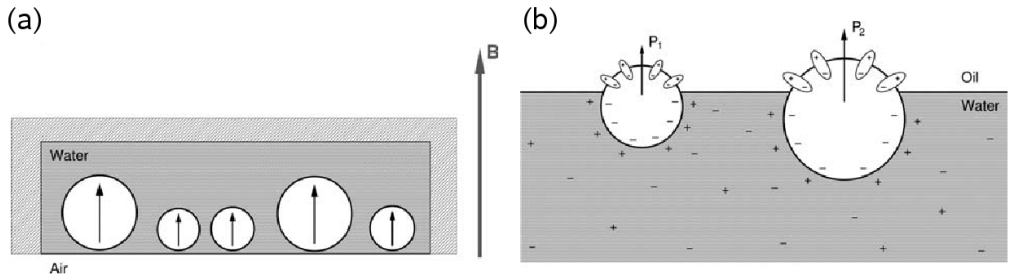

Figure 6.1: Scematic illustration of system I and II; (a) two colloids of different size trapped at the oil-water interface. The dipole moments P_1 and P_2 are given by the vector sum of the dipole moments on the particle-oil interface; (b) colloidal particles trapped at the water-air interfacein a pendant water droplet. The external magnetic field **B** is applied on the colloids.

film surrounding the polystyrene colloid with dipoles. The net dipole moment of the dipoles surrounding the colloid is non-zero, because the dipole interaction is screened in the aqueous phase.

In both cases, one can apply an external magnetic field to induce a repulsive colloid-colloid interaction, whose direction and strength can easily be controlled via the external field; the dipole moments almost perfectly align along the field direction and the magnitude of the dipole moment is proportional to the field strength. In the conventional setup, the field is perpendicular to the interface, inducing a repulsive interaction between the colloids, additional to the short-ranged steric repulsion arising from the physical cores of the colloids. For large fields, the typical strength of the repulsive dipole-dipole interaction is much larger than the thermal energy, leading to crystallisation of the colloids. Both realisations have been extensively studied with experiments [136, 138, 140, 139], and simulations [141, 137, 144]. As shown in [142] at suffiecient low density the dipole-dipole interactions of system I and II become equivalent. The pair interactions of colloids of a binary mixture (with diameter σ_A or σ_B), has the form of a power law

$$\Psi_{ij}(r) \cong (z_i z_j)^{5/2}/r^3 \tag{6.1}$$

where r is the distance between the centers of the two colloids, and $z_{i,j}$ is either 1 or $z = \sigma_\mathrm{B}/\sigma_\mathrm{A} < 1$ if $i, j =$ A or B. At this regime where system I and II become equivalent the $z^{5/2}$ corresponds to the suspensibility of the supermagnetic colloids of system I. In this work we will work in this density regime where eq. 6.1 holds.

Knowing the effective interactions between the particles one can use computer simulations to obtain the minimum energy configuration (MEC), and thus the fa-

vored crystal structure at $T = 0$. However, it is well known that binary mixtures tend to exhibit a broad spectrum of rather complex alloy phases [145] corresponding to a very rough energy landscape; few optimization algorithms are able to solve such high-dimensional and complex problems. To overcome this difficulty, genetic algorithms (GAs) have been applied to the case of binary mixtures with their interactions been described by to eq. 6.1. The results revealed a rich spectrum of exotic ordered ground-state structures [142].

The main focus of the current work was to explore, with the use of GA, the crystal structures emerging from a binary mixture of colloids when the external field is *tilted* with respect to the normal of the interface. The tilt angle introduces an anisotropic interaction creating new exotic crystal structures. As the field is tilted beyond a critical angle the patterns switch over being dominated by chains aligned parallel to the field.

The paper is organized as follows. In Sec. 6.2 we define our model and present the simulation methods used. The results are presented and discussed in Sec. 6.3. Finally, in Sec. 6.4 we summarise the conclusions.

6.2 Simulation Methods

6.2.1 Model

We consider a binary mixture of particles, namely type A and B, with their diameter ratio, $z = \sigma_B/\sigma_A = 0.5$, unless stated otherwise. To determine the global energy minimum of such a system, we assume that the particles arrange themselves in a set of Bravais lattices. Specifically, we consider a two-dimensional Bravais lattice with an N-particle unit cell, where N is the sum of particles of type A and B, that is $N = N_A + N_B$.

The candidate structures are generated by the periodic repetition of the unit cell, which is a parallelogram formed by the vectors $\mathbf{a}$ and $\mathbf{b}$ that substain an angle ψ between them, as shown in Fig. 6.2(c). For convenience, but without loss of generality, we set the particles occupying vertices of the parallelogram to be of type A, and their positions are described by the linear combination $\mathbf{r} = l\mathbf{a} + m\mathbf{b}$, where l and m are integers. We introduce a coordinate system (x, y) and, choosing the x axis parallel to the unit-cell vector $\mathbf{a}$, the primitive vectors of the Bravais lattice take the form:

$$\begin{aligned} \mathbf{a} &= \alpha\,(x, 0) \\ \mathbf{b} &= \alpha\left(\cos\psi, \sin\psi\right) \end{aligned} \tag{6.2}$$

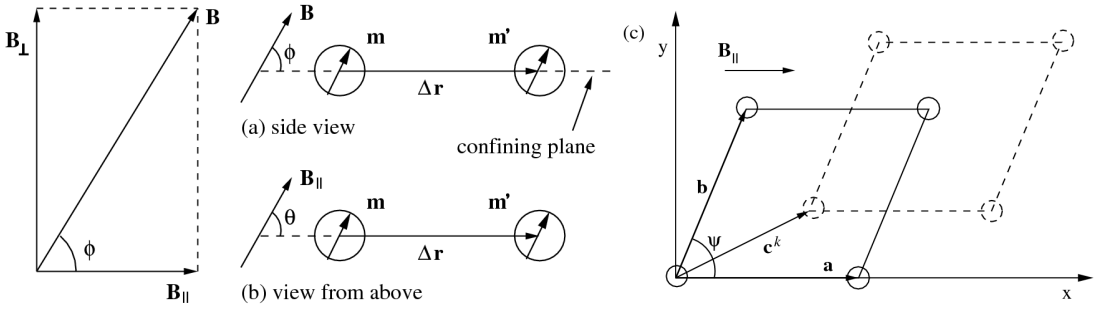

Figure 6.2: (a) and (b) show schematic views of two particles, with magnetic moments $\mathbf{m}$ and $\mathbf{m}'$, perfectly aligned along the external magnetic field, $\mathbf{B}$. (c) The geometry of a two-dimensional Bravais lattice with one particle per unit cell, as well the basis vector $\mathbf{c}^k$ that characterizes the position of an additional particle.

where x is a variable determining the length of $\mathbf{a}$ vector, $|\mathbf{a}| = x|\mathbf{b}|$, and α is a scaling variable defined by the number density as $\rho = N/|\mathbf{a}\times\mathbf{b}| = N/x\alpha^2\sin\psi$. Now, since ρ will be fixed, it allows the elimination of one parameter of our model, $\alpha = \sqrt{N/x\rho\sin\psi}$. We will call the lattice just described as the *primary lattice*. The additional particles of the unit-cell, which can be of type A or B, are placed inside the parallelogram, and their positions are specified by the set of vectors $\mathbf{c}_k = c_k^{\mathrm{a}}\mathbf{a} + c_k^{\mathrm{b}}\mathbf{b}$, where $c_k^{\mathrm{a,b}}$ are coefficients and k is the index of the additional particles, $k = 2,...,N$. The value $k = 1$ is reserved for the coordinates of the particle belonging to the first-lattice, $\mathbf{c}_1 = (0,0)$.

When such a cell is repeated periodically over space, it produces N lattices, and each of them is shifted with respect to the first-lattice by the vectors $\mathbf{c}_k$. Hence, the positions of the particles on the (x,y) plane are given by the vector $\mathbf{r}+\mathbf{c}_k$.

To calculate the total energy per particle, U, in a structure defined by our model, one has to calculate the lattice sum of all unique interactions between the particles of the unit cell; the interactions are defined in Sec. 6.2.2, but for now they will represented by $u_{i,j}(\mathbf{r})$. For example, if we had one particle in the unit cell, in other words we have only the primitive lattice, then the total energy per particle would be:

$$U_{i,i}^1 = \frac{1}{2}\sum_{\mathbf{r}\neq 0} u_{ii}(\mathbf{r}) \tag{6.3}$$

where the set $\{\mathbf{r}\}$ spans a Bravais lattice, which takes the form of a lattice sum $\sum_{l=-\infty}^{\infty}\sum_{m=-\infty}^{\infty}(...)$ running over the integers l and m, with the exception of $(l,m) = (0,0)$. Having an additional particle in the unit cell, the total energy per particle will be the average of the sum of each particle of the unit cell interacting with all other particles within its own sublattice, plus the additional energy between the particles belonging to different sublattices. Therefore the total energy per particle for two

particle unit cell takes the form:

$$U^2 = \frac{1}{2}\left(U^1_{i,i} + U^1_{j,j}\right) + \frac{1}{2}\sum_{\mathbf{r}} u_{i,j}(\mathbf{r} + \mathbf{c}_2 - \mathbf{c}_1) \tag{6.4}$$

Now, with the same reasoning we write the total energy per particle for an N-particle unit cell:

$$\begin{aligned} U_N \;=\; & \frac{1}{N}\left[\frac{1}{2}\sum_{\mathbf{r}\neq 0}\sum_{i=\mathrm{A,B}} u_{i,i}(\mathbf{r}) \right. \\ & \left. + \sum_{\mathbf{r}}\sum_{k=1}^{N-1}\sum_{k'=k+1}^{N} u_{i,j}(\mathbf{r} + \mathbf{c}_k - \mathbf{c}_{k'})\right] \end{aligned} \tag{6.5}$$

Hence, the parameters that characterise the structure of the lattice are N, ρ, x, ψ, c^{a}_k, and c^{b}_k. These parameters are subject to the following constrains:

$$0 < x \leq 1, \quad 0 < \psi \leq \pi/2, \quad 0 \leq c^{\mathrm{a,b}}_k \leq 1. \tag{6.6}$$

Note that the representation in eq. 6.2, even with the above constraints, is *not* unique, since different sets of parameters can create equivalent structures; these ambiguities are excluded by a suitable algorithm described in Sec. 6.2.3.

In the following we characterize composition of the binary mixture by the mole fraction of small particles, $C = N_B/N$. The parameter ranges we explore in this work are, $\rho = 0.4$, 0.6 and 0.8, $C = 1/2$, $2/3$, $3/4$, $4/5$, $1/3$, $1/4$, and $1/5$.

6.2.2 Interactions

As mentioned in the introduction, we will study colloids with dipole-dipole interactions, and with an external magnetic field, $\mathbf{B}$, strong enough to create crystallization. Before we define the interactions between the particles, we define the two components of the $\mathbf{B}$, one parallel to the plane of the interface, $\mathbf{B}_\parallel$, and the other normal to the interface, $\mathbf{B}_\perp$, see Fig. 6.2(a). For convenience, we set the $\mathbf{B}_\parallel$ to be parallel with the x-axis and the vector $\mathbf{a}$. Therefore the field is expressed as $\mathbf{B} = |\mathbf{B}|(\cos\phi, 0, \sin\phi)$. Now, based on the approach presented in Ref. [146], the dipole-dipole pair potential at the interface in the presence of a strong magnetic field, $\mathbf{B}$, is

$$V_{\mathrm{dd}}(r, \chi_i\mathbf{B}, \chi_j\mathbf{B}) = \frac{\chi_i\chi_j\mathbf{B}^2}{2}\frac{1}{r^3}(1 - 3\cos^2\phi\cos^2\theta) \tag{6.7}$$

where $\cos\theta = \Delta\mathbf{r}\cdot\mathbf{B}_\parallel/(rB_\parallel)$, $\Delta\mathbf{r} = \mathbf{r} + \mathbf{c}_k - \mathbf{c}_{k'}$ is the separation vector of two particles on the lattice, ϕ is the tilt angle of the magnetic field with respect to the confining

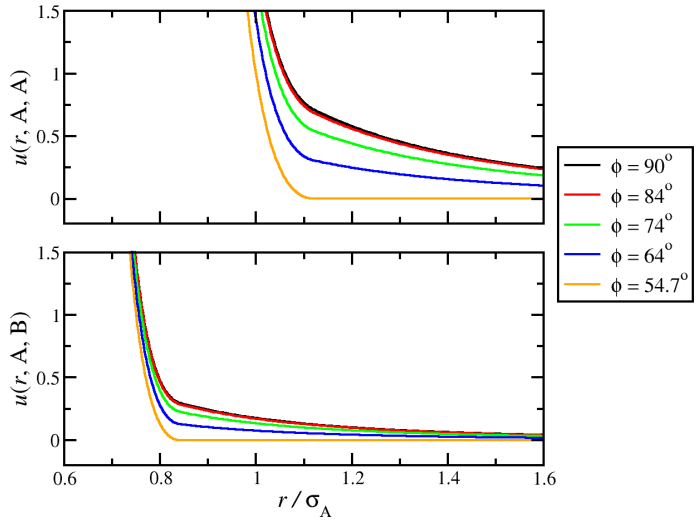

Figure 6.3: (Color online) Two diagrams showing the total potential of interaction at $\theta = 0$ between two particles of type A (top) and one A and one B type (bottom) as a function of interparticle separation for different values of the tilt angle, ϕ.

plane, and χ_i is the susceptibility of particle i, see Fig. 6.2(a).

However, since we will work in low enough density, where the asymptotic behavior for a system of dipolar colloids when the external magnetic field is perpendicular to the interface holds and is described by eq. 6.1, then we recall the correspondence $z_i^{5/2} \leftrightarrow \chi_i$. Using this, we eliminate the factor $\frac{\chi_i \chi_j \mathbf{B}^2}{2}$ in eq. 6.7, and thus we can re-write the pair dipole-dipole interaction as:

$$V_{\mathrm{dd}}(r, z_i, z_j) = (z_i z_j)^{5/2} \frac{1}{r^3}(1 - 3\cos^2\phi\cos^2\theta) \tag{6.8}$$

The degree of anisotropy is controlled via the tilt angle ϕ, as seen in Fig. 6.4, which allows the particles to adopt less repulsive head-to-tail configuration ($\theta = 0$). In this work we will restrict the tilt angle above the threshold value $\arccos(1/\sqrt{3}) \approx 54.7°$; below that value, the dipole interactions in the nose-to-tail configuration becomes attractive. The values we explore are $\phi = 54.7°$, 59°, 64°, 74°, and 84°. Additionally, we generate structures at 90° for comparison.

At high degree of anisotropy the particles will collapse to each other due to the absence of repulsive interactions in the x direction. For this reason the purely repulsive Weeks-Chandler-Andersen (WCA) potential [59], which is a Lennard-Jones potential cut and shifted at the position of the minimum, $r_{\mathrm{min}} = 2^{1/6}\sigma_{ij}$, is used to

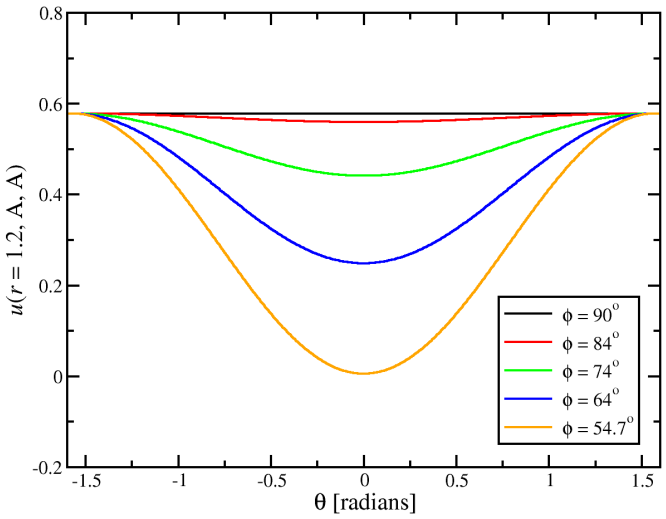

Figure 6.4: (Color online) The diagram shows the total potential of interaction between two A type particles at fixed interparticle separation, $r = 1.2\sigma_A$, as a function of θ.

model the short-ranged repulsion between the physical cores of the colloids,

$$V_{\mathrm{WCA}}(r) = \begin{cases} 4\varepsilon_{ij}\left[\left(\frac{\sigma_{ij}}{r}\right)^{12} - \left(\frac{\sigma_{ij}}{r}\right)^{6}\right] + \varepsilon_{ij} & r \le r_{\min} \\ 0 & r > r_{\min} \end{cases} \tag{6.9}$$

where σ_{ij} is the effective particle diameter, and ε_{ij} sets the energy scale of the short-ranged soft core repulsion; the values of these parameters were determined by the well-known Lorentz-Berthelot mixing rules [147], $\epsilon_{ij} = \sqrt{\epsilon_{ii}\epsilon_{jj}}$, $\sigma_{ij} = (\sigma_{ii} + \sigma_{jj})/2$.

Joining eq. 6.8 and eq. 6.9 together, the total pair potential takes the form:

$$u_{i,j}(\Delta\mathbf{r}) = V_{\mathrm{dd}}(\Delta\mathbf{r}, z_i, z_j) + V_{\mathrm{WCA}}(|\Delta\mathbf{r}|) \tag{6.10}$$

6.2.3 Genetic Algorithms

Introduction

Many interesting optimization problems, require a reasonable fast algorithm. Given a hard optimization problem, we need to search through a space of potential solutions by either finding, if possible, an efficient problem-specific algorithm which is approximately optimal, or by using probabilistic algorithms, which despite being powerful, do not guarantee to give the optimum solution. For small spaces, classical exhaustive methods usually suffice; for larger spaces special artificial intelligence techniques

must be employed. GAs are stochastic search algorithms invented in the 1970s by Holland to solve high dimensional and complex problems in engineering science [148]. These methods are inspired by the Darwinian struggle for survival and employ evolutionary processes as key elements to obtain the optimal solution to a particular problem. However, strictly speaking, GAs do *not* optimize, and neither does biological evolution [148, 149]. Evolution uses whatever material that is at its disposal to produce above average individuals; it has no ultimate goal of "perfection". Nevertheless, GAs form the basis of extremely robust optimization methods, which are able to take the whole search space into account, and at the same time concentrate their computing efforts on promising regions (for an overview see Ref. [150]).

Genetic Algorithms in general

We briefly summarize the basic ideas of a GA and in the subsequent section will show how it will be applied to our specific problem.

GA represents a candidate solution as an *individual*, whose *genes*, fixed in number, represent the variables of the given problem. The genes in an individual can take values from a suitably chosen alphabet, such as binary, with digits 0 and 1 as its letters. All the genes together form the *chromosome* as a string of digits. Individuals are evaluated via a problem-specific fitness function in the sense that a better or fitter individual has a higher fitness value. A large, but fixed, number of individuals form a generation.

The initialization of the GA's first generation is realized at random. A new generation is formed by selecting individuals to be parents from the former generation according to their fitness values, and then generating new individuals to form the subsequent generation. Several procedures for this mating recombination processes have been proposed in the literature [151]. In addition, mutations are performed with a certain probability during the mating process, a procedure necessary to avoid persistent inbreeding and to allow at the same time for the reintroduction of new or lost genetic material. At each iteration selection-recombination-mutation-evaluation cycle, a fraction of the former generation is replaced to form the new generation. Usually, we retain individuals with the highest fitness value, but other replacement procedures exist. The final solution is represented by the fittest individual in the population after many generations.

Genetic Algorithms in our problem

These general ideas behind GAs are now applied to our problem of obtaining the optimal crystal structure of a binary mixture of colloidal particles, by using the model

described in sec. 6.2.1. The formalism has been used in similar problems elsewhere in the literature [152].

We translate our model represented by the set of parameters $\{x, \Psi, c_1^{\mathrm{a}}, c_1^{\mathrm{b}}, ..., c_N^{\mathrm{a}}, c_N^{\mathrm{b}}\}$, where $\Psi = \psi/(\pi/2)$, into an individual $\mathscr{I} = \mathscr{I}(y_1, y_2, ..., y_{2N})$, where $y_1, .., y_{2N}$ represent the parameters of our model as strings of genes of fixed length, $n_{\mathrm{gene}} = 6$. The genes are expressed by a decimal alphabet i.e. an alphabet composed by the one-digit integers $0, 1, 2...9$. The aim of the encoding is to produce a chromosome from which the GA will use later. For example, assuming an individual is a point in (x, y) space; the encoding process would produce

$$(x, y) = (0.122334, 0.988776) \rightarrow 122334988776 \tag{6.11}$$

For the present investigation, we used the number of individuals, $N_p = 500$, and the number of generations $N_{\mathscr{G}} = 300$. Even though for most cases explored a smaller genetic population would be suffient to give a solution; a large population maintains diversity between individuals, and thus covering the whole search space.

As mentioned in Sec. 6.2.1, we need to implement an algorithm to ensure a unique representation of the Bravais lattice. This is achieved by requiring the perimeter of the unit cell, Π, to be minimal, and it is given by the equation,

$$\Pi = 2\,(|\mathbf{a}| + |\mathbf{b}|) \tag{6.12}$$

To minimize eq. 6.12, the following iterative algorithm was applied: the vectors $\mathbf{a}$ and $\mathbf{b}$ are replaced by new vectors, from the four options the combination with the lowest value out of Π,

$$\{\mathbf{a} \pm \mathbf{b}, \mathbf{b}\} \quad \text{and} \quad \{\mathbf{a}, \mathbf{a} \pm \mathbf{b}\} \tag{6.13}$$

If none of the possible combinations minimize Π, then the algorithm stops and the initial $\mathbf{a}$ and $\mathbf{b}$ are used. The vectors $\mathbf{c}_k$ are not required to be checked by the algorithm, since they are linear combination of $\mathbf{a}$ and $\mathbf{b}$.

A positive fitness value is assigned to each individual $\mathscr{I}$ via the fitness function $f(\mathscr{I})$: a higher fitness value characterizes a better solution. The optimum solution is a crystal structure with the lowest free energy, $F = U - TS$, where S is entropy, but for our purposes we look for crystals formed by the system at zero temperature ($T = 0$). Therefore, the optimum crystal structure will have lowest potential energy, U, which can be calculated by eq. 6.5 and eq. 6.10. Additionally, for practical reasons we look at the ratio $U(\mathscr{I})/U(\mathscr{I}^{\mathrm{hex}})$, where $U(\mathscr{I}^{\mathrm{hex}})$ is the potential energy of a hexagonal structure (hex) generated by one particle unit cell at the same density. The reason behind this is to ensure that the values used will be of order 1. Hence, $f(\mathscr{I})$, in our

problem, reads

$$f(\mathscr{I}) = \exp\left\{1 - \frac{U(\mathscr{I})}{U(\mathscr{I}^{\text{hex}})}\right\} \tag{6.14}$$

Once the first generation, $\mathscr{G}_0$ is realized and its individuals are evaluated by the fitting function, we sort them out by a ranking scheme. For example, the fittest individual will have rank value $R\left[f(\mathscr{I}_j)\right] = 1$, while the least fit will have $R\left[f(\mathscr{I}_j)\right] = N_p$. This ranking scheme is important for avoiding breeding shortcomings and to ensure the existence of selection pressure throughout the simulation [151].

Afterwards, the interactive process of creating a new generation, starts. In the first step, two individuals are selected as parents according to the rank of their fitness values with the *roulette wheel algorithm* [151]. First, we generate a random number $w \in [0, S]$, where S is the sum of the differential fitness, S_j, over all the individuals in the population:

$$S = \sum_{j=1}^{N_p} S_j = \sum_{j=1}^{N_p} \frac{N_p - R\left[f(\mathscr{I}_j)\right] + 1}{N_p} \tag{6.15}$$

Now we use w to locate the element T_j in the following inequality,

$$T_{j-1} \leq w < T_j \tag{6.16}$$

where T_j is the running sum,

$$T_j = \sum_{i=1}^{j} S_j, \quad j = 1, ..., N_p \tag{6.17}$$

This procedure is equivalent to constructing a roulette wheel, where each individual is occupying a sector of angular size $\frac{1}{2\pi} S_j / S$ and the random number represents the spinning wheel. In other words, the probability of the wheel stopping at a sector is proportional to the sector. Once the parents are chosen, two new individuals populate the new generation via a one-point crossover, as visualized in Fig. 6.5. The crossover point, which is randomly chosen, is where each of the parent's gene sequence is cut and combined to create the new individuals. This action is unbiased in respect to the geometry of the problem and cannot be associated with any physical movement of the particles. Further, we perform mutations with a probability p_m, which has a typical value of 0.1, on the new individuals. It means that we randomly choose one of the genes and replace it with a new one.

Even though the process of recombination and mutation will create two new individuals, it is not guaranteed that they will join the new generation. A number of criteria must be fulfilled. First, they must be at least as fit as the least-fit members of the existing population; the latter will be eliminated and replaced by the new

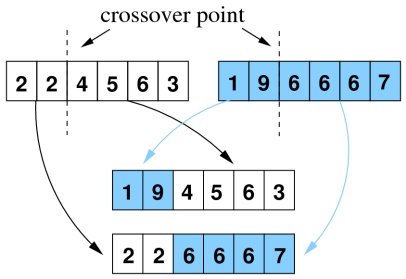

Figure 6.5: (Color online) Schematic representation of the one-point crossover that generates two new individuals from two parents.

members. Second, the new individuals must not be identical with any other member of the population; this *no-duplicate* criterion is an important safeguard against inbreeding.

To test the efficiency of the reproduction strategy described above, it was compared to an alternative reproduction strategy in which we select parents randomly with no regard to fitness, and then randomly replace members of the population with the new individuals. An exception to this replacement is granded to the fittest individual, as a form of elitism. Similar strategies to this has been found advantageous for problems tending to suffer from premature convergence [153].

After the GA has provided with a solution a final optimization with gradient descent was applied. The last step was needed to increase the accuracy of the results.

6.3 Results & Discussion

We present the ordered equilibrium configurations obtained by the GA, as the angle of the magnetic field is tilted. The results are organizing into four blocks. (a) In Fig. 6.6 structures with $C \geq 1/2$ are shown. (b) Structures with $C < 1/2$ are in Fig. 6.8. (c) A comparison with structures of different densities are in Fig. 6.9. (d) Structures with smaller diameter ratio $z = 0.3296$, at $\rho = 0.6$ are presented in Fig. 6.10.

6.3.1 $C \geq 1/2$

We start with the case $C \geq 1/2$, where the small particles form more complex structures, as seen in Fig. 6.6. For the angle range $74^\circ < \phi < 90^\circ$, the patterns of the structures only slightly perturbed from the structures at $\phi = 90^\circ$. For $\phi < 74^\circ$ the anisotropy becomes significant, and both the small and big particles attempt to take advantage of it by generating new patterns; see Fig. 6.6(i), (m), (n), (r) and (s). At $\phi = 54.7^\circ$ there is no repulsion along the x-axis and the particles form chains parallel

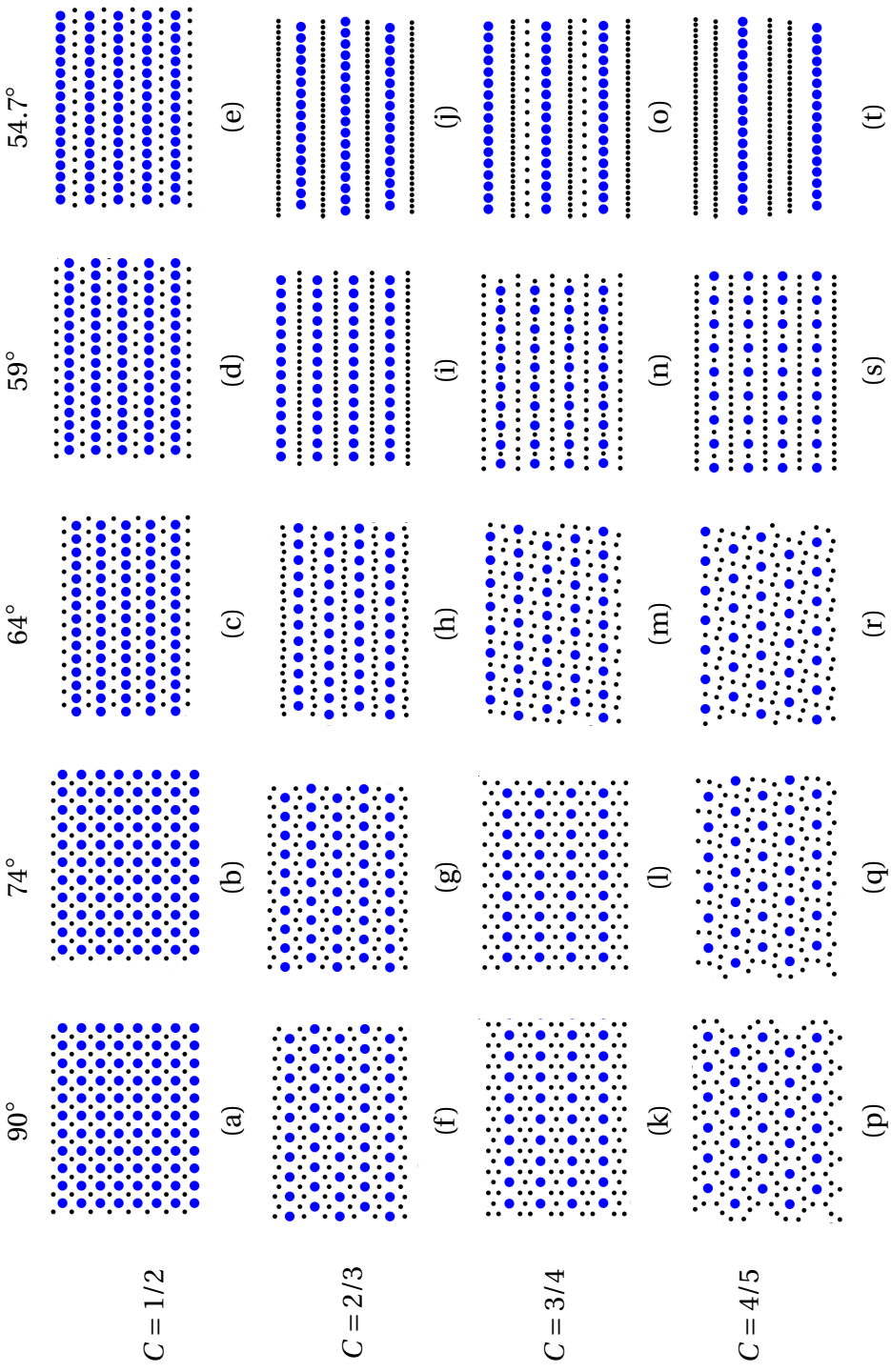

Figure 6.6: (Color online) Minimum energy configurations for $C \geq 1/2$, for $\rho = 0.6$.

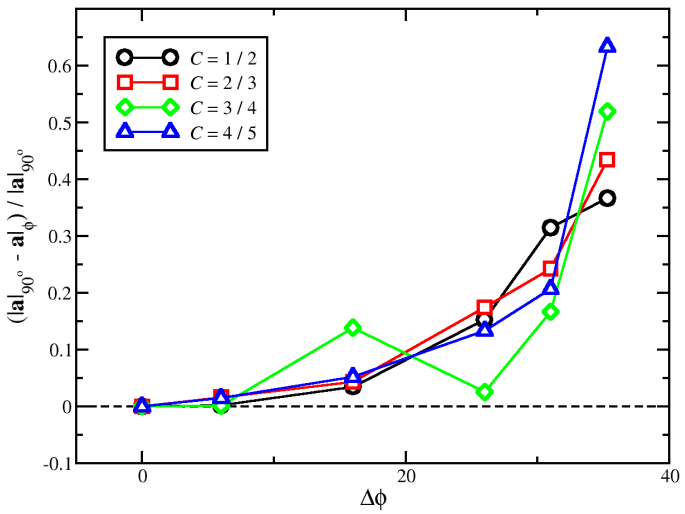

Figure 6.7: (Color online) The diagram shows relative change of length of the vector $\mathbf{a} = \alpha x$ for different tilt angles.

to the field.

To understand the results, we view the length of vector $|\mathbf{a}|$ as a function of $\Delta\phi = 90^\circ - \phi$, so at $\Delta\phi = 0^\circ$, $|\mathbf{a}| = |\mathbf{a}|_0$. Naively, one would expect the length of vector $\mathbf{a}$ to be monotonically decrease as $\Delta\phi$ increases, however that is not always the case. In Fig. 6.7, we plot the ratio of relative displacement of the A-type particles of the first lattice along the x-axis, $(|\mathbf{a}|_0 - |\mathbf{a}|_{\Delta\phi}/|\mathbf{a}|_0)$, versus $\Delta\phi$. For all cases, the ratio remains at the same level up to the threshold $\Delta\phi \approx 16^\circ$, above that threshold it rapidly increases. However, in the case $C = 3/4$, initially there is an increase, at $\Delta\phi$ there is descrease, meaning that the length of the $\mathbf{a}$ vector increases, but after a certain value of $\Delta\phi$, the ratio increases as expected. Note that in our initial assumptions of our model, the length of vector $\mathbf{a}$ is always smaller than the length of $\mathbf{b}$. Even though, this significantly simplifies the problem it has also the effect to limit the search space. Nevertheless, when the restriction was removed, there was no change in our results. An explanation for this behavior is that the small particles in the unit cell feel first the anisotropy and attempt to come in between the primary lattice's particles into a head-tail configuration, compare Figs. 6.6(l) and (m). Additionally, the particles of the primary lattice also attempt to position themselves into a more favorable oblique formation.

Now, as the angle of the magnetic field is tilted further the particles of the primary lattice prefer to come closer together, while increasing their separation distance in the y-axis, as seen clearly in the cases $C = 1/2$ and $C = 2/3$, Fig. 6.6(d) and (i). In the cases $C = 3/4$ and $C = 4/5$ at 59°, we observe that one of the small particles has

moved between the particles of the primary lattice, by creating an inhomogeneous chain, Fig. 6.6(n) and (s). The structures at $\phi = 54.7°$ converge into a series of chains parallel to the magnetic field. The small particles can form chains of uneven numbers, Fig. 6.6(o). The reason is that the primary lattice particles come as close as possible with each other along the x-axis, thus maximizing their distance in y-axis, and by doing that in essence they reduce the available space for the small particles to create chains. As the number of small particles increases there is no enough space to accompany the third particle, therefore it creates a new chain. For $C = 4/5$ two such chains composed by small particles are formed. Even though chains can be formed for $\phi > 54.7°$, such in the cases Figs. 6.6(n) and (s), some of them have mixed type of particles something that it is not observed at $\phi = 54.7°$, see Figs. 6.6(e), (j), (o) and (t).

6.3.2 $C < 1/2$

In the second block of results, $C < 1/2$, the big particles become the majority component and attempt to form hexagonal structures, which are disturbed by the small particle, as seen in Figs. 6.8(a), (f) and (k). In particular, at perpendicular field, $\phi = 90°$, the neighbors of the small particle form a square, which is also seen as the optimum structure for the system $C = 1/2$, see Fig. 6.6(a). Similar with the cases of $C \geq 1/2$, as the field is tilted the particles will rearrange by taking advantage of the anisotropy.

When anisotropy becomes significant enough, the particles attempt to form chains as seen in Figs.6.8(c), (d), (h), (i) and (m), (n). In the cases of $C = 1/3$ and $C = 1/5$ the chains are straight, but in other case, $C = 1/4$, the particles' excluded volume comes into effect and restricts them to form straight lines. The result is to form small zig-zags [frustrated chains], but this effect disappears as the repulsion along the x-axis is reduced. Also, in the case of $C = 1/5$ see Figs.6.8(k-o), there was no significant changes in the system's structure due to the domination of the big particles. The hexagonal structures change to obligue and then to chain-like oblique structures, while the rectangular structures, created by the effects of the small particles, do show any significant changes.

At $\phi = 54.7°$ the particles form chains of the same type, aligned parallel to the field. It is interesting to note that parallel chains of particles of A-type form chain-like oblique structures as it has been found for one component systems in Ref. [146], but if between the chains there is a small particle, then the chains of A-type particles form rectangular structures with be the small particle in the middle (compare Figs.6.8(e), (j), and (o) with Fig.6.6(e)).

Figure 6.8: (Color online) Minimum energy configurations for $C < 1/2$, for $\rho = 0.6$. The particles with color blue belong to the primary lattice, while the particles with color red are A-type particles.

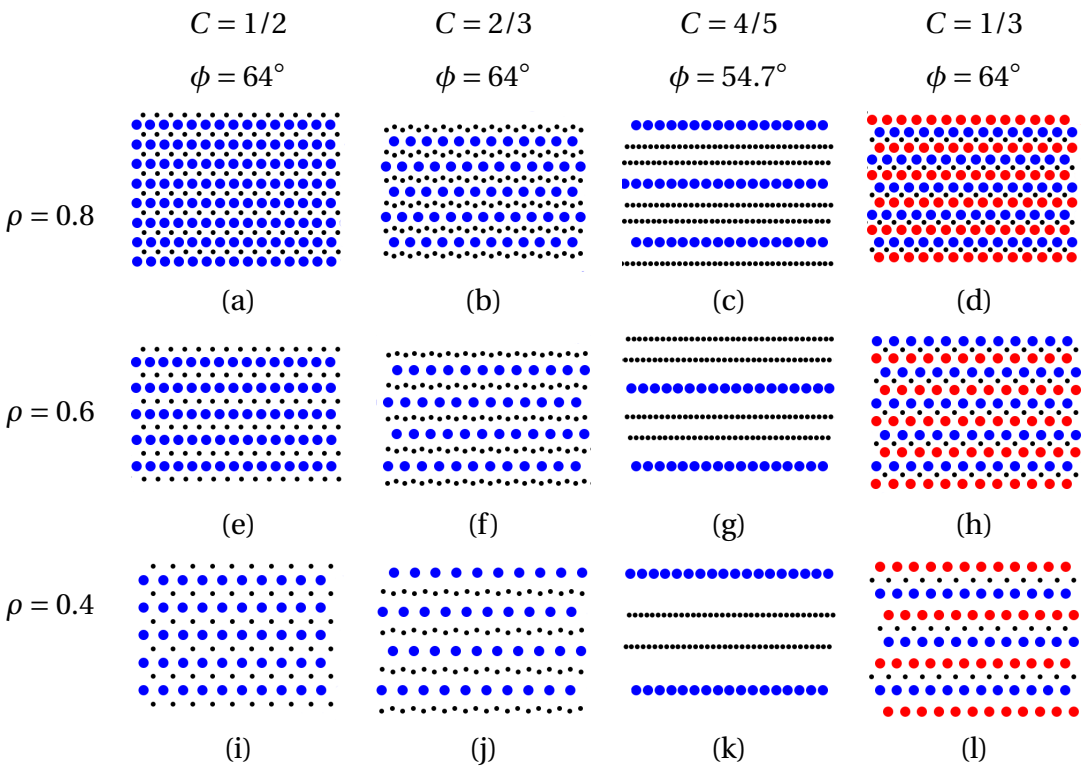

Figure 6.9: (Color online) Minimum energy configuration of different compositions as their patterns are affected by density.

6.3.3 Density effects

In sufficiently dilute concentrations of binary magnetic colloidal mixtures, the pair potential scales as a power law at long distances, $\sim r^{-3}$. This feature generates patterns that are *scale-free*, meaning that the overall density is an irrelevant parameter, as shown in previous investigations, where the field was perpendicular to the interface [142]. Only at higher densities, does the excluded volume becomes a significant factor, the system cease to be scale-free. In our simulations, we do observe the same patterns for different values of densities for tilted external fields with non-zero interaction along the x-axis. In Fig. 6.9 we present different compositions at different densities with a tilted field, and discuss how it is affected by anisotropy. In the first example, see Fig. 6.9(a), (f), and (k), the system, which is at tilt angle is $\phi = 64°$, remains invariant under change of density. In the second example, we have one more small particle, i.e. for $C = 2/3$, at the same tilt angle, the system changes slightly over different values of density, but maintain essentially the same pattern, Fig. 6.9(b), (f) and (j). The reason is that at high density, the excluded volume becomes significant and reduces the space between the particles. Therefore, the small particles are unable to maintain their pattern they had at lower densities in order to take advantage of the anisotropy.

In the first two examples, anisotropy does not affect the system's scale-free features. However, this is true so long there is a repulsive interaction among the particles along the x-axis. At $\phi = 54.7°$ there is no interaction anymore between the particles in the x-direction, which breaks the scale-free feature. As seen at Fig. 6.9(c), (g) and (k), the pattern may essentially remain the same, but along the x-axis the particles ceases to scale by not changing positions as density changes.

A final example is displayed at Fig. 6.9(d), (h) and (l), where the composition of the system $C = 1/3$, which has higher packing fraction than $C = 2/3$, compare with Fig. 6.9(b), (f) and (j). The anisotropy, similar to the case $C = 2/3$, does not affect the system being scale-fee, till the point there is no interaction in one direction, as it happens for $\phi = 54.7°$.

6.3.4 Diameter ratio effects

In the final block of results, we look at structure with composition $C > 1/2$, but with smaller diameter ratio, $z = 0.3296$. From a quick look at the structures, the same behavior is observed when $z = 0.5$; initially the structures are perturbed, then new structures emerge, and at $\phi = 54.7°$ chains are formed. Despite the similarities there are some small but significant differences. The first one occurs for $C = 2/3$ at $\phi = 54.7°$, Fig. 6.10(e) where the small particles form a chain, but they are not equally spaced; the small particles form pairs. The reason behind this is that the small particles attempt to maximize their distance from the big particles not only along the y-axis but also the x-axis due to the absence of interactions between the particles along the x-axis. This effect is not observed for $z = 0.5$, because two small particles to cover the distance between two particles of the primary lattice.

A smaller diameter ratio also has an effect of reducing the number of chains formed by the small particles at $\phi = 54.7°$. For example, comparing $C = 3/4$ at $z = 0.5$ (Fig. 6.6(o)) and at $z = 0.3296$ (Fig. 6.10(j)), we observe that at lower diameter ratio there is one less chain. As mentioned above this happens because more particles can fit into one chain without steric repulsive iteractions come into effect.

6.4 Conclusions

We have applied genetic algorithms to study equilibrium configurations of binary mixture of two dimensional dipolar particles in the presence of a tilted external magnetic field, which introduces anisotropic interactions between the particles. At small degree of anisotropy the structures are perturbed, while once the anisotropy reaches the maximum degree, that is when there is no repulsive (or attractive) interactions

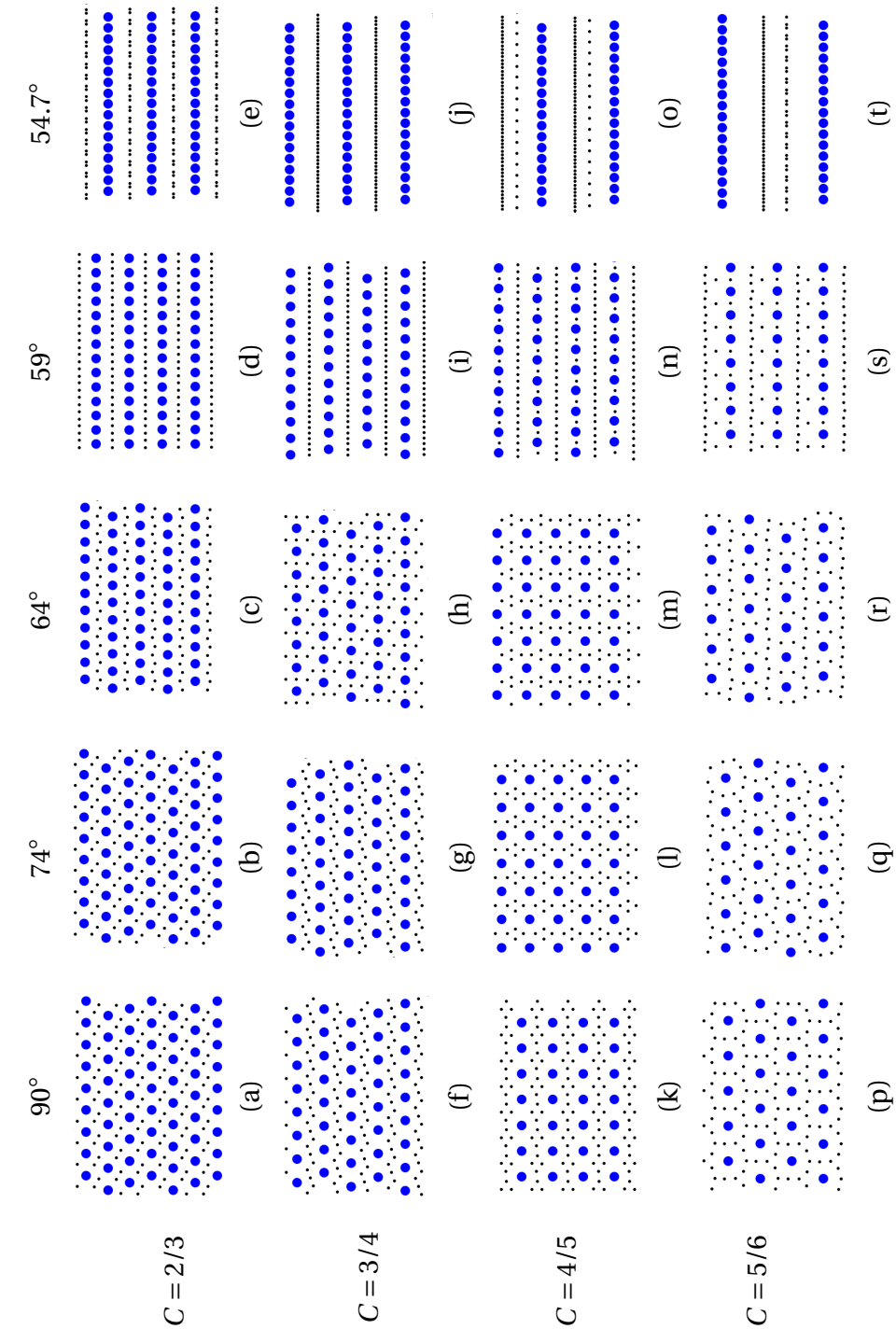

Figure 6.10: (Color online) Minimum energy configurations for $C \geq 1/2$, $\rho = 0.6$, and $z = 0.3296$.

along the direction of the magnetic field, the particles form chains aligned parallel to the field. By varying the degree of anisotropy and density we found a rich spectrum of new structures.

Chapter 7

Conclusions

This thesis is divided into three parts. The first part contains two studies of physisorbed polymers (linear and star) on surfaces. In the second part, an attempt has been made to realise a scale-free near-neighbour network in computer simulations of polydisperse fluids of hard disks. In the final part we explore the minimum energy configurations of two dimensional binary mixture of magnetic colloids in tilted external fields.

In the first part, we were motivated by atomic-force microscopy images of polymer films (either linear chains or stars), on mica surfaces, adsorbed from dilute solution following a good solvent-to-bad solvent quenching transition. In the case of linear chains a bimodal cluster distribution is observed under certain experimental conditions. We used a bead-spring molecular model and Langevin dynamics computer simulations and demonstrated that a bimodal distribution can be reproduced in the simulations and rationalised on the basis of the polymer structures prior to the quench. In addition to providing insight on experimental observations, the simulation results support a number of predicted scaling laws such as the decay of the monomer density as a function of distance from the surface. Additionally, the same methodology has been used to study many arms stars polymers, in which the soft-colloidal nature of star polymers was studied in the proximity of a surface. Measurements of the fraction of monomers bound to the surface, height, radius of gyration and asphericity provided valuable insights on the structures. We rationalised the results and allowed us to map the stars' behaviours (from polymer-like to soft-colloid) based on the number of arms and their length on a given surface.

In the second part of this thesis we examine the neighbour network in a two-dimensional polydisperse hard-disk fluid with diameter distribution $p(\sigma) \sim \sigma^{-4}$ is examined using constant-pressure Monte Carlo simulations.Graphs are constructed from vertices (disks) with edges (links) connecting each vertex to k neighbouring

vertices defined by radical tessellation. At packing fractions in the range $0.24 \leq \eta \leq 0.36$, the decay of the network degree distribution is observed to be consistent with the power-law $k^{-\gamma}$ where the exponent lies in the range $5.6 \leq \gamma \leq 6.0$. Comparisons with the predictions of a maximum-entropy theory suggest that this apparent power-law behaviour is not the asymptotic one, and that $p_k \sim k^{-4}$ in the limit $k \to \infty$. This asymptotic dependence is consistent with the simple idea that for large disks, the number of neighbours is proportional to the disk diameter. A power-law decay of the network degree distribution is one of the characteristics of a scale-free network. The assortativity of the network is measured, and is found to be positive, meaning that vertices of equal degree are connected more often than in a random network. Finally, the equation of state is determined and compared with the prediction from a scaled-particle theory. Very good agreement between simulation and theory is demonstrated.

In the final part, we use genetic algorithms, which allow to efficiently search energy landscapes and obtain their global minimum, to investigate the ordered equilibrium structures formed by binary mixtures of anisotropic dipolar particles confined to a plane, under the presence of an external magnetic field. Anisotropy is introduced by tilting the external magnetic field with respect to the interface. Initially, as the field is tilted the isotropic structures are perturbed only slightly, but as anisotropy becomes enhanced by tilting the magnetic field further new structures emerge. Once anisotropy becomes dominant, the structures form chains parallel to the field.

Appendix A

Appendix - Papers published

1. *Magnetic properties of polydisperse ferrofluids: A critical comparison between experiment, theory and computer simulation*, A. O. Ivanov, S. S. Kantorovich, E. N. Reznikov, C. Holm, A. F. Pshenichnikov, A. V. Lebedev, A. Chremos, and P. J. Camp, Phys. Rev. E **75**, 061405 (2007).

2. *Polymer-like to soft colloid-like behavior of regular star polymers adsorbed on surfaces*, E. Glynos, A. Chremos, G. Petekidis, P. J. Camp, and V. Koutsos, Macromolecules **40**, 6947-6958 (2007).

3. *Neighbor network in a polydisperse hard-disk fluid: degree distribution and assortativity*, A. Chremos and P. J. Camp, Phys. Rev. E **76**, 056108 (2007).

4. *Magnetic measurements as a key for the particle size distribution in ferrofluids: experiment, theory, and computer simulations*, A. O. Ivanov, S. S. Kantorovich, E. N. Reznikov, C. Holm, A. F. Pshenichnikov, A. V. Lebedev, A. Chremos, and P. J. Camp, Magnetohydrodynamics **43**, 393-400 (2007).

5. *Adsorption and self-assembly of linear polymers on surfaces: A computer simulation study*, A. Chremos, E. Glynos, V. Koutsos, and P. J. Camp, Soft Matter, accepted (2008).

6. *Collapsing and clustering after solvent evaporation of physisorbed linear homopolymer on surfaces: an atomic force microscopy study*, E. Glynos, A. Chremos, P. J. Camp, E. Theofanidou, and V. Koutsos, submitted to Macromolecules.

7. *Adsorption and self-assembly of star polymers on surfaces: A computer simulation study*, A. Chremos, E. Glynos, V. Koutsos and P. J. Camp, in preparation.

8. *Crystal structures of two-dimensional binary mixtures of dipolar colloids in tilted external fields*, A. Chremos and C. N. Likos, in preparation.

9. *Complex fluid and solid structures of binary core-softened particles,* A. C. Fogarty, A. Chremos, and P. J. Camp, in preparation.

Bibliography

[1] E. Glynos, A. Chremos, G. Petekidis, P. J. Camp, V. Koutsos (in preparation).

[2] E. Glynos, *et al.*, *Macromolecules* **40**, 6947 (2007).

[3] S. Asakura, F. Oosawa, *J. Polym. Sci.* **33**, 181 (1958).

[4] S. M. Ilett, A. Orrock, W. C. K. Poon, P. N. Pusey, *Phys. Rev E* **51**, 1344 (1995).

[5] J. Dzubiella, C. N. Likos, H. Löwen, *J. Chem. Phys.* **116**, 9518 (2002).

[6] A. L. Barabási, E. Bonabeau, *Scientific American* **May**, 50 (2003).

[7] M. E. J. Newman, *Proc. Natl. Acad. Sci. U.S.A.* **98**, 404 (2001).

[8] R. Aveyard, B. P. Binks, J. H. Clint, *et al.*, *Phys. Rev. Lett.* **88**, 246102 (2002).

[9] M. P. Allen, D. J. Tildesley, *Computer simulation of liquids* (Clarendon Press, Oxford, 1987).

[10] J.-P. Hansen, I. R. McDonald, *Theory of simply liquids* (Academic Press, London, 2006).

[11] D. Frenkel, B. Smit, *Understanding molecular simulations* (Academic Press, London, 2001).

[12] J. T. Padding, A. A. Louis, *Phys. Rev. E* **74**, 031402 (2006).

[13] M. E. Cates, *et al.*, *J. Phys. Condens. Matter* **16**, S3903 (2004).

[14] P. G. de Gennes, *Scaling Concepts in Polymer Physics* (Cornell University Press, Cornell, 1979).

[15] M. Rubinstein, R. H. Colby, *Polymer Physics* (Oxford University Press, Oxford, 2003).

[16] D. H. Napper, *Polymeric Stabilization of Colloidal Dispersions* (Academic Press, London, 1983).

[17] A. P. Gast, L. Leibler, *Macromolecules* **19**, 686 (1986).

[18] J. K. Cox, A. Eisenberg, R. B. Lennox, *Curr. Opin. Colloid Interface Sci.* **4**, 52 (1999).

[19] K. B. Migler, H. Hervet, L. Leger, *Phys. Rev. Lett.* **70**, 1993 (1993).

[20] H. R. Brown, *Science* **263**, 1411 (1994).

[21] P. O. Brown, D. Botstein, *Nat. Genet. Suppl.* **21**, 33 (1999).

[22] E. Pludeman, N. Collins, *Adhesion Science and Technology* (Plenum Press, New York, 1975).

[23] R. Viswanathan, J. Tian, D. W. M. Marr, *Langmuir* **13**, 1840 (1997).

[24] G. Bar, Y. Thomann, M.-H. Whangbo, *Langmuir* **14**, 1219 (1998).

[25] D. Raghavan, X. Gu, T. Nguyen, M. V. Landingham, A. Karim, *Macromolecules* **33**, 2573 (2000).

[26] J. C. Meiners, A. Q.-R. J. Mlynek, *Macromolecules* **30**, 1997 (1997).

[27] J. Kumaki, T. Hashimoto, *J. Am. Chem. Soc.* **125**, 4907 (2003).

[28] J. C. Zhao, *et al.*, *Eur. Phys. J. E* **16**, 49 (2005).

[29] V. Koutsos, E. W. van der Vegte, E. Pelletier, A. Stamouli, G. Hadziioannou, *Macromolecules* **30**, 4719 (1997).

[30] V. Koutsos, E. W. van der Vegte, E. Pelletier, G. Hadziioannou, *Macromolecules* **32**, 1233 (1999).

[31] K. Furukawa, *Acc. Chem. Res.* **36**, 102 (2003).

[32] A. Milchev, K. Binder, *Macromolecules* **29**, 343 (1996).

[33] K. Binder, A. Milchev, J. Baschnagel, *Annual Reviews Mater. Sci.* **107**, 107 (1996).

[34] A. Milchev, K. Binder, *J. Chem. Phys.* **114**, 8610 (2001).

[35] D. Mukherji, G. Bartels, M. H. Müser, *Phys. Rev. Lett.* **100**, 068301 (2008).

[36] Y. Wang, R. Rajagopalan, *J. Chem. Phys.* **105**, 696 (1996).

[37] H. X. Guo, X. Z. Yang, T. Li, *Phys. Rev. E* **61**, 4185 (2000).

[38] N. Källrot, P. Linse, *Macromolecules* **40**, 4669 (2007).

[39] W. P. J. Luettmer-Strathmann, F. Rampf, K. Binder, *J. Chem. Phys.* **128**, 064903 (2008).

[40] R. Descas, J.-U. Sommer, A. Blumen, *J. Chem. Phys.* **125**, 214702 (2006).

[41] S. Metzger, M. Müller, K. Binder, J. Baschnagel, *J. Chem. Phys.* **118**, 8489 (2003).

[42] E. Bouchaud, M. Daoud, *J. Phys.* **48**, 1991 (1987).

[43] A. N. Semenov, J. Bonet-Avalos, A. Johner, J. F. Joanny, *Macromolecules* **29**, 2179 (1996).

[44] P. G. de Gennes, *Macromolecules* **14**, 1637 (1981).

[45] L. Auvray, J. P. Cotton, *Macromolecules* **20**, 202 (1987).

[46] L. T. Lee, O. Guiselin, B. Farnoux, A. Lapp, *Macromolecules* **24**, 2518 (1991).

[47] O. Guiselin, L. T. Lee, B. Farnoux, A. Lapp, *J. Chem. Phys.* **95**, 4632 (1991).

[48] O. Guiselin, *Europhys. Lett.* **17**, 225 (1992).

[49] J. de Joannis, R. K. Ballamudi, C.-W. Park, J. Thomatos, I. A. Bitsanis, *Europhys. Lett.* **56**, 200 (2001).

[50] J. de Joannis, C.-W. Park, J. Thomatos, I. A. Bitsanis, *Langmuir* **17**, 69 (2001).

[51] P. Cifra, *Macromol. Theory Simul.* **12**, 270 (2003).

[52] T. A. Witten, P. A. Pincus, *Structured fluids: polymers, colloids, surfactants* (Oxford University Press, Oxford, 2004).

[53] S. O. Nielsen, C. F. Lopez, G. Srinivas, M. L. Klein, *J. Phys.: Condens. Matter* **16**, R481 (2004).

[54] G. S. Grest, K. Kremer, *Phys. Rev. A* **33**, 3628 (1986).

[55] G. S. Grest, K. Kremer, T. A. Witten, *Macromolecules* **20**, 1376 (1987).

[56] G. S. Grest, *Macromolecules* **27**, 3493 (1994).

[57] S. W. Sides, G. S. Grest, M. J. Stevens, *Macromolecules* **35**, 566 (2002).

[58] M. O. Steinhauser, *J. Chem. Phys.* **122**, 094901 (2005).

[59] J. D. Weeks, D. Chandler, H. C. Andersen, *J. Chem. Phys.* **54**, 5237 (1971).

[60] E. Eisenriegler, *Polymers Near Surfaces* (World Scientific, River Edge, 1993).

[61] E. Eisenriegler, K. Kremer, K. Binder, *J. Chem. Phys.* **77**, 6296 (1982).

[62] P. Frantz, S. Granick, *Macromolecules* **28**, 6915 (1995).

[63] R. R. Netz, D. Andelman, *Rhys. Rep.* **380**, 1 (2003).

[64] D. Mukherji, M. H. Müser, *Macromolecules* **40**, 1754 (2007).

[65] M. Daoud, J. P. Cotton, *J. Physique* **43**, 531 (1982).

[66] T. M. Birshtein, E. B. Zhulina, *Polymer* **25**, 1453 (1984).

[67] T. M. Birshtein, E. B. Zhulina, V. O. Borisov, *Polymer* **27**, 1078 (1986).

[68] K. Solc, W. H. Stockmayer, *J. Chem. Phys.* **54**, 2756 (1971).

[69] K. Solc, *J. Chem. Phys.* **55**, 2335 (1971).

[70] K. Solc, *Macromolecules* **6**, 378 (1973).

[71] J. Batoulis, *Macromolecules* **22**, 4277 (1989).

[72] G. Zifferer, *J. Chem. Phys.* **110**, 4668 (1999).

[73] K. Ohno, K. Binder, *J. Chem. Phys.* **95**, 5444 (1991).

[74] K. Ohno, K. Binder, *J. Chem. Phys.* **95**, 5459 (1991).

[75] J. F. Joanny, A. Johner, *J. Phys. II* **6**, 511 (1996).

[76] K. Shida, K. Ohno, M. Kimura, K. Y., *J. Phys. Chem* **105**, 8929 (1996).

[77] G. Kritikos, A. F. Terzis, *Polymer* **49**, 3601 (2008).

[78] I. Hiotelis, A. G. Koutsioubas, N. Spiliotopoulos, *et al.*, *Macromolecules* **41**, 7648 (2008).

[79] A. Chremos, E. Glynos, V. Koutsos, P. J. Camp (submitted to Soft Matter).

[80] C. N. Likos, *et al.*, *Phys. Rev. Lett.* **80**, 4450 (1998).

[81] K. Binder, *Applications of Monte Carlo Methods in Statistical Physics* (Springer, Berlin, 1984).

[82] A. Jusufi, J. Dzubiella, C. N. Likos, C. von Ferber, H. Löwen, *J. Phys. Condens. Matt.* **13**, 6177 (2001).

[83] G. Zifferer, *J. Chem. Phys.* **102**, 3720 (1994).

[84] J. Rudnick, G. Gaspari, *Science* **237**, 384 (1987).

[85] P. Erdös, A. Rényi, *Publ. Math.* **6**, 290 (1959).

[86] R. Albert, A.-L. Barabási, *Rev. Mod. Phys.* **74**, 47 (2002).

[87] R. Albert, H. Jeong, A.-L. Barabási, *Nature* **401**, 130 (1999).

[88] A.-L. Barabási, R. Albert, H. Jeong, *Physica A* **281**, 69 (2000).

[89] M. Faloutsos, P. Faloutsos, C. Faloutsos, *Comptut. Commun. Rev.* **29**, 251 (1999).

[90] H. Jeong, B. Tombor, R. Albert, Z. N. Oltvai, A.-L. Barabási, *Nature* **407**, 651 (2000).

[91] P. Uetz, *et al.*, *Nature* **403**, 623 (2000).

[92] H. Jeong, S. P. Mason, A.-L. Barabási, Z. N. Oltvai, *Nature* **411**, 41 (2001).

[93] F. Liljeros, C. R. Edling, L. A. N. Amaral, H. E. Stanley, Y. Aberg, *Nature* **411**, 907 (2001).

[94] A.-L. Barabási, R. Albert, *Science* **286**, 509 (1999).

[95] R. N. Onody, P. A. de Castro, *Phys. Rev. E* **70**, 037103 (2004).

[96] A.-L. Barabási, E. Bonabeau, *Sci. Am.* **288**, 50 (2003).

[97] L. Li, D. Anderson, J. C. Doyle, W. Willinger, *Internet Math.* **2**, 431 (2006).

[98] R. Delannay, G. L. Gaër, *Phys. Rev. Lett.* **73**, 1553 (1994).

[99] M. F. Miri, N. Rivier, *Phys. Rev. E* **73**, 031101 (2006).

[100] D. S. Callaway, J. E. Hopcroft, J. M. Kleinberg, M. E. J. Newman, S. H. Strogatz, *Phys. Rev. E* **64**, 041902 (2001).

[101] M. E. J. Newman, *Phys. Rev. Lett.* **89**, 208701 (2002).

[102] M. E. J. Newman, *SIAM Rev.* **45**, 167 (2003).

[103] M. E. J. Newman, J. Park, *Phys. Rev. E* **68**, 036122 (2003).

[104] J. S. Andrade, Jr., J. Herrmann, R. F. S. Andrade, L. R. da Silva, *Phys. Rev. Lett.* **94**, 018702 (2005).

[105] P. B. Thomas, D. Dhar, *J. Phys. A* **27**, 2257 (1994).

[106] H. D. Rozenfed, D. ben Avraham, *Phys. Rev. E* **75**, 061102 (2007).

[107] J. P. K. Doye, C. P. Massen, *Phys. Rev. E* **71**, 016128 (2005).

[108] C. P. Massen, J. P. K. Doye, *Phys. Rev. E* **71**, 046101 (2005).

[109] J. P. K. Doye, C. P. Massen, *J. Chem. Phys.* **122**, 084105 (2005).

[110] C. P. Massen, J. P. K. Doye, *Phys. Rev. E* **75**, 037101 (2007).

[111] B. J. Gellatly, J. L. Finney, *J. Non-Cryst. Solids* **50**, 313 (1982).

[112] C. Annic, *et al.*, *J. Phys. I* **4**, 115 (1994).

[113] J. P. Troadec, A. Gervois, C. Annic, J. Lemaitre, *J. Phys. I* **4**, 1121 (1994).

[114] A. Gervois, *et al.*, *Physica A* **218**, 403 (1995).

[115] D. A. Aboav, *Metallography* **3**, 383 (1970).

[116] D. Wearie, *Metallography* **7**, 157 (1974).

[117] D. A. Aboav, *Metallography* **13**, 43 (1980).

[118] M. A. Pshkin, K. J. Strandburg, N. Rivier, *Phys. Rev. Lett.* **67**, 1803 (1991).

[119] N. Rivier, *J. Phys. I* **4**, 127 (1994).

[120] R. P. Sear, J. Cuesta, *Phys. Rev. Lett.* **91**, 245701 (2003).

[121] H. Reiss, H. L. Frisch, *J. Chem. Phys.* **31**, 369 (1959).

[122] C. Dress, W. Krauth, *J. Phys. A* **28**, L597 (1995).

[123] J. W. Liu, E. Luijten, *Phys. Rev. Lett.* **92**, 035504 (2004).

[124] B. Widom, *J. Chem. Phys.* **39**, 2808 (1963).

[125] W. R. Smith, S. Labík, *Mol. Phys.* **80**, 1561 (1993).

[126] S. Labík, W. R. Smith, *Mol. Sim.* **12**, 23 (1994).

[127] M. P. Allen, G. T. Evans, D. Frenkel, B. M. Mulder, *Adv. Chem. Phys.* **86**, 1 (1993).

[128] J.-P. Hansen, R. M. I, *Theory of simple liquids* (Academic Press, London, 1986).

[129] P. Calka, *Adv. Appl. Prob.* **35**, 863 (2003).

[130] V. S. Kumar, *J. Chem. Phys.* **123**, 074502 (2005).

[131] H. Bauke, *Eur. Phys. J. B* **58**, 167 (2007).

[132] A. Clauset, C. R. Shalizi, M. E. J. Newman p. arXiv:0706.1062 (2007).

[133] S. Asakura, F. Oosawa, *J. Chem. Phys.* **22**, 1255 (1954).

[134] A. Vrij, *Pure Appl. Chem.* **48**, 471 (1976).

[135] H. N. W. Lekkerkerker, W. C.-K. Poon, P. N. Pusey, A. Stroobants, P. B. Warren, *Europhys. Lett.* **20**, 559 (1992).

[136] R. Aveyard, J. H. Clint, D. Nees, N. Quirke, *Langmuir* **16**, 8820 (2000).

[137] P. J. Camp, *Phys. Rev. E* **68**, 061506 (2003).

[138] K. Zahn, A. Wille, G. Maret, S. Sengupta, P. Nielaba, *Phys. Rev. Lett.* **90**, 155506 (2003).

[139] D. J. Robinson, J. C. Earnshaw, *Phys. Rev. Lett.* **71**, 715 (1993).

[140] A. J. Hurd, D. W. Schaefer, *Phys. Rev. Lett.* **54**, 1043 (1985).

[141] N. Hoffmann, F. Ebert, C. N. Likos, H. Löwen, G. Maret, *Phys. Rev. Lett.* **97**, 078301 (2006).

[142] J. Fornleitner, F. L. Verso, G. Kahl, C. N. Likos, *Soft Matter* **4**, 480 (2008).

[143] F. Bresme, M. Oettel, *Condes. Matter* **19**, 413101 (2007).

[144] J. Sun, T. Stirner, *Langmuir* **17**, 3103 (2001).

[145] C. N. Likos, C. L. Henley, *Philos. Mag. B* **68**, 85 (1993).

[146] V. A. Froltsov, R. Blaak, C. N. Likos, H. Löwen, *Phys. Rev. E* **68**, 061406 (2003).

[147] G. C. Maitland, M. Rigby, E. B. Smith, W. A. Wakeham, *Intermolecular Forces* (Oxford University Press, Clarendon, 1981).

[148] J. H. Holland, *Adaption in Natural and Artificial Systems* (MIT Press, 1992).

[149] K. A. DeJong, *Foundations of Genetic Algorithms* (Whitley, New York, 1993).

[150] Z. Michalewicz, *Genetic Algorithms + Data Structures = Evolution Programs* (Springer-Verlag, 1992).

[151] D. E. Goldberg, *Genetic Algorithms in Search, Optimization, and Machine Learning* (Addison-Wesley, Reading, 1989).

[152] D. Gottwald, G. Kahl, C. N. Likos, *J. Chem. Phys.* **122**, 204503 (2005).

[153] W. Cedeno, V. R. Vemuri, T. Slezak, *Evolutionary Comp.* **2**, 321 (1994).